Linköping University | Institution of Economic and Industrial Development
ISRN-number: LIU-IEI-TEK-A–21/04024-SE
LIU-IEI - June 18, 2021

Solid and Fluid Investigations of the Heat Distribution in and Around a Fighter Aircraft

- The Effect of Important Simulation Parameters

Ester Lundin
Linnea Sund

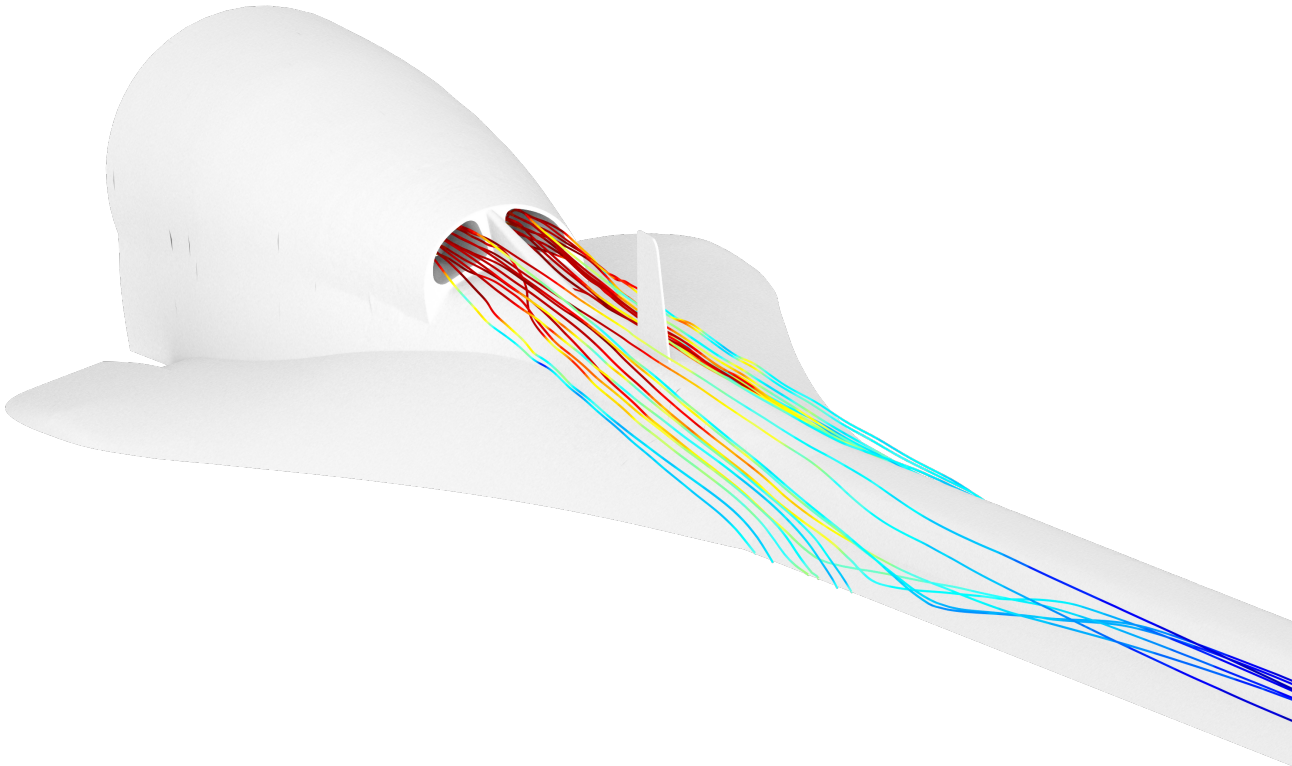

Academic Supervisor: Roland Gårdhagen
Industrial Supervisors: Henrik Rosendahl and Philip Evegren
Examiner: Matts Karlsson

LINKÖPINGS UNIVERSITET

Linköping University
SE-581 83 Linköping, Sweden
+46 013 28 10 00, www.liu.se

Abstract

Heat management is an important issue in fighter aircrafts and the number of heat generating components in aircrafts are increasing [1]. It is therefore of great importance to accurately predict temperature distribution in the aircraft structure to ensure flight safety. Solid and fluid simulations can be used to predict the temperatures in and around the aircraft at a lower cost than experiments.

In this thesis the effect of common heat transfer and modelling parameters on solid and fluid simulations were separately investigated. The heat transfer coefficient and the thermal contact resistance were investigated on a verified solid simulation and validated towards experimental data.

In the fluid simulation model, it was investigated whether deviations from general recommendations on parameters, y^+ and the CFL number, can still produce relatively accurate results. The effect of the numerical techniques RANS and URANS as well as the turbulence models SST $k-\omega$ and RKE Two-layer were also investigated. Since no validation was possible, focus was placed on the relative differences between investigated parameters and techniques. The results were also compared to similar results found in the literature.

A verified and validated solid simulation model was obtained, it showed a high accuracy for a low computational cost. The resulting thermal contact resistance was higher in the stationary simulation than in the transient, although they were similar and both were within ranges found in the literature. Deviations from general recommendations for y^+ and CFL were shown to accurately predict the flow behaviour for few of the investigated cases. The turbulence was shown to be damped by the RKE Two-layer model in transient simulations as well as showing similar behaviour to the SST $k-\omega$ used in steady simulations. Further simulations are needed to accurately investigate the introduced errors and inaccuracies in the fluid simulation methods.

Acknowledgements

This thesis was carried out at the section of Environmental Engineering and Thermal Analysis at SAAB AB. We would like to express our utmost gratitude to our supervisors Henrik Rosendahl and Philip Evegren for their technical and personal support throughout the thesis. They have given us a warm and honest welcome into the company as well as creating a secure atmosphere. We would also like to thank our examiner, Matts Karlsson, and supervisor, Roland Gårdhagen, at Linköping University. As well a great thanks to our opponents that gave good inputs and questions regarding the work.

Ester Lundin & Linnea Sund
June 18, 2021, Linköping

Nomenclature

Acronyms

BC	Boundary Condition
BL	Boundary Layer
CFD	Computational Fluid Dynamics
CFL	Courant-Friedrichs-Lewy Condition
CHT	Conjugated Heat Transfer
DES	Detached Eddy Simulation
DNS	Direct Numerical Simulation
EoS	Equation of State
HTC	Heat Transfer Coefficient
LES	Large Eddy Simulation
RANS	Reynolds Averaged Navier-Stokes
RKE	Realizable $k - \varepsilon$
SDR	Specific Dissipation Rate
SST k-ω	k-ω Shear Stress Transport Turbulence Model
TCR	Thermal Contact Resistance
TE	Trailing Edge
TKE	Turbulent Kinetic Energy
URANS	Unsteady Reynolds Averaged Navier-Stokes

Symbols

β	Inverse of the film temperature	$[1/K]$
ϵ	Emissivity constant	$[-]$
μ	Dynamic viscosity	$[kg/ms]$
μ_t	Eddy viscosity	[Pa·s]
ω	Specific dissipation rate	$[1/s]$
ρ	Density	$[kg/m^2]$
σ	Stefan Boltzmanns constant	$[W/m^2K^4]$
τ	Turbulent shear stress	$[Pa]$
$\mathbf{v}$	Velocity vector	$[m/s]$

ε	Turbulent kinetic energy's dissipation rate	$[m^2/s^3]$
A	Area	$[m^2]$
C_p	Specific heat constant	$[J/kgK]$
E	Total energy	$[J/m]$
Gr	Grashof's number	$[-]$
h	Heat transfer coefficient	$[W/m^2K]$
i	Internal energy	$[m^2/s^2]$
k	Turbulence kinetic energy	$[m^2/s^2]$
k_t	Thermal conductivity	$[W/mK]$
L	Reference length	$[m]$
M	Mach number	$[-]$
Nu	Nusselt number	$[-]$
p	Pressure	$[Pa]$
Pr	Prandtl number	$[-]$
q	Heat flux	$[W/m^2]$
R	The universal gas constant	$[J/K \cdot mol]$
Ra	Rayliegh number	$[-]$
Re	Reynolds number	$[-]$
S_i	Energy source term	$[W/m^3]$
T	Temperature	$[K]$
t	Time	$[s]$
u, v, w	Velocity component	$[m/s]$
$\mathbf{f}_b$	Body force resultant	$[-]$
$\mathbf{T}_V$	Viscous stress tensor	$[Pa]$
$\mathbf{T}_{RANS}$	Stress tensor	$[Pa]$

Contents

1 Introduction

1.1 Background

The generation and spread of heat is an important phenomenon to understand and investigate in order to ensure the integrity of many critical structures. With increased knowledge regarding the temperature and its distribution in an aircraft structure, more precise requirements can be set for the mechanical properties of the materials. This can enable a reduction in weight or change of material, resulting in a reduced cost.

Heat is generated in several areas of an aircraft and needs to be managed to not cause damage on the structure or impair the function of the aircraft. The number of heat generating high performance components inside aircrafts are increasing [1] and this leads to more heat being generated and less space being available for cooling of the components. One way of managing the generated heat is to use ambient air for cooling in a heat exchanger. The heated ambient air is then ejected overboard and due to the pressure field and impact of fluid flow about the body, it often travels alongside the skin of the aircraft. The heat is then conducted into the structure of the aircraft. Because of this, it is important to know the flow field to accurately predict the heat distribution on the surface and in the structure. The increased temperature may affect the structural integrity of the aircraft and can also have a negative impact on important underlying components.

Flight tests are expensive, especially if time-dependent and accurate data over large geometrical areas are desired. Because of this, simulations are often used to investigate these types of problems during the design process. Another advantage of simulations is that they are not limited to a few measuring positions but calculate values for the important parameters throughout the entire domain. The accuracy of the simulation results will however be affected by the method and solver setup used.

This master thesis was carried out at SAAB AB and concerns the aerothermal impact on the structure of an aircraft. Current methods for calculating temperatures and temperature distributions are conservative to ensure flight safety. In order to gain more knowledge and set better requirements for materials and dimensions for future developments by SAAB AB it is of interest to further investigate how the fluid flow distribution, including the hot jettisoned air, will affect the heat distribution in the main structure. One way to obtain this knowledge is to perform conjugated heat transfer (CHT) simulations where a solid and fluid model is combined. The access to increased computational resources at SAAB AB has enabled further investigations in this area using computational fluid dynamics (CFD) and computational heat transfer simulations.

A CFD method is generally validated towards experimental or analytical data before it is trusted. For some applications however, no such data is available. Important information might in some cases be extracted from the simulations despite this. Differences in flow behaviour for different solver settings and turbulence models can for example be investigated for a specific case. General requirements for parameters such as the y^+ value or the Courant Fredrichs Lewy (CFL) number often lead to costly computations. The requirements for the parameters are set to ensure a certain level of accuracy, however with the constant improvements in commercial solvers it is relevant to occasionally re-investigate the effect of these parameters.

It is common in today's industries to use steady Reynolds averaged Navier-Stokes (RANS) equations to model fluid flow since it is easy to use and computationally cheap [2]. For some applications however, an unsteady RANS (URANS) could be used to ensure convergence and to capture some of the unsteadiness in the flow, for example flows including vortex shedding. By attaining results from comparisons between these numerical techniques, increased knowledge of introduced errors and what flow phenomenon that are neglected when using steady RANS models can be obtained. It also gives a clearer picture of how the fluid behaves, which is beneficial information for engineers working with these types of flows [3].

It is also important to investigate solid simulation modelling. Small changes in parameters such as the heat transfer coefficient (HTC) and the thermal contact resistance (TCR) can greatly affect the results and should therefore be carefully chosen. Making sure that the parameters are realistic can be done by performing experimental tests and a validation study. At SAAB AB there is a close relation to the physical products on site and validation investigations are therefore possible. This in combination with access to increased computational resources enables the level of accuracy to be investigated.

1.2 Problem Statement

Managing temperature and its distribution in a fighter aircraft is crucial to ensure flight safety. Hot jettisoned air that travels along the fuselage of an aircraft conducts heat into the aircraft structure. Simulations are a cost effective way of predicting the temperature distribution in both the surrounding air and the solid structure. In this thesis, a solid and fluid simulation model were separately investigated to improve accuracy and reduce computational costs. The two models could then be used together in a CHT model in the future.

1.3 Aim and Research Questions

The aim of this thesis was partly to investigate if more accurate parameter values could be used when considering solid structures in future CHT simulations. The aim was also to investigate whether different solver setups in fluid simulations could increase accuracy and reduce the computational cost and thereby enable less conservative design criteria. The investigations were performed using both experimental and computational methods. To reach the aim of this thesis the following research questions were answered:

- To what degree can the solid simulation model be trusted?
- How important are the choices of the parameters of interest, such as HTC and TCR?
- What is the loss in accuracy when performing RANS simulations in comparison to URANS?
- How well is the fluid flow captured, in the domains considered in this thesis, when y^+ and CFL deviates from general recommendations?
- What are the major differences between the turbulence models Shear stress transport $k-\omega$ and Realizable $k-\varepsilon$ Two-layer?

1.4 Delimitations

To be able to follow the set time frame of 20 weeks, delimitations were necessary. Some delimitations were also a result of the available test equipment. Below the delimitations are presented.

- Thermal experiments were performed on a section of an aircraft in order to validate a solid simulation model. Since the area of interest was the temperature distribution no other forces acting on the structure were considered.
- Since the available resources could not be used to emulate forced convection over the test section, it was not considered for the experiments and validation for the fluid model was therefore not possible.
- A study was performed investigating general parameters of CFD simulations. The study was performed on a section of an aircraft and the inner structure was excluded in order to reduce the computational cost.
- One flight case was used throughout the thesis.

2 Theory

In this section introductory theory of heat transfer, *section 2.1* and *2.2*, and computational heat transfer, *section 2.3*, is presented.

2.1 Conduction, Convection and Radiation

When investigating the heat distribution within materials and structures it is important to be aware of the three modes of heat transfer: conduction, convection and radiation. The driving force for all three modes is a temperature difference, where the heat is transferred from a hotter to a colder region.

Conduction is the phenomenon where heat is transferred between two solid or stationary fluid bodies in contact. The heat transfers from the hot region to the colder region and a temperature gradient is therefore present. The rate at which heat is transferred, q, can be calculated according to Fourier's law, Equation (1), where k_t is the thermal conductivity of the material, A is the reference area and the partial derivative is the temperature gradient through the material [4]. It should be noted that Equation (1) is for one-dimensional cases and the conduction in y and z direction are neglected.

$$q_{conduction} = -k_t A \frac{\partial T}{\partial x} \tag{1}$$

Convection is the phenomenon where heat is transferred due to fluid motion. If fluid motion is caused by an external force, the heat transfer occurs through forced convection. Natural convection is when movement in the fluid is caused by density changes occurring due to the heating or cooling of local fluid regions, which moves the fluid by gravitational forces. The convectional heat transfer can be calculated through use of Newton's law of cooling, Equation (2), where h is the heat transfer coefficient, T_s is the surface temperature and T_∞ is the ambient temperature of the fluid. The heat transfer coefficient is calculated according to Equation (3), where Nu is the Nusselt number and L the reference length. [4]

$$q_{convection} = hA(T_s - T_\infty) \tag{2}$$

$$h = \frac{Nu \cdot k_t}{L} \tag{3}$$

The Nusselt number is calculated dependent of the state of the flow as well as the geometry and position of the considered object. In this thesis the Nusselt number for natural convection was used. The Nusselt number for natural convection on a horizontal flat plate with the heated side facing upwards is calculated according to Equation (4), where Pr is the Prandtl number, Equation (5) where c_p is the specific heat at constant pressure and μ the dynamic viscosity. The Prandtl number is the ratio of momentum to thermal diffusivity and is a dimensionless constant. Gr is the Grashof number, Equation (6) where g is the gravitational constant and ν the kinematic viscosity. The product of the Grashof and

Prandtl numbers is called Rayliegh (Ra) number and is calculated according to Equation (7). [4]

$$Nu_{\,heat\ upwards} = 0.16(Gr_L Pr)^{1/3} \quad , \quad 2 \cdot 10^8 < Gr_L Pr < 10^{11} \tag{4}$$

$$Pr = \frac{c_p \mu}{k_t} \tag{5}$$

$$Gr_L = \frac{g\beta(T_s - T_\infty)L^3}{\nu^2} \quad , \quad \beta = \frac{2}{T_w + T_\infty} \tag{6}$$

$$Ra_L = Gr_L Pr = \frac{g\beta c_p \mu (T_s - T_\infty)L^3}{k_t \nu^2} \tag{7}$$

The Nusselt number for natural convection with the heated side facing downwards on a horizontal plate as well as on a heated vertical plate can be calculated according to Equation (8) [4] and (9) [5] respectively.

$$Nu_{\,heat\ downwards} = 0.58(Gr_L Pr)^{(1/5)} \quad , \quad 10^6 < Gr_L Pr < 10^{11} \tag{8}$$

$$Nu_{\,vertical\ plate} = 0.021(Gr_L Pr)^{(2/5)} \quad , \quad 10^9 < Gr_L Pr \tag{9}$$

Thermal radiation occurs when a hot surface radiates heat to a colder surface through a partially or fully transparent medium. The resulting radiating effect can be calculated according to Equation (10), where ϵ is the combined emissivity constant, σ the Stefan Boltzmann constant that equals $5.67 \cdot 10^{-8}\ W/m^2K^4$ while T_1 and T_2 are the radiating surfaces' temperatures. The combined emissivity constant that considers the emissivity of both surfaces affected by the radiation, Equation (11), is an approximation that assumes two infinitely long surfaces [5]. The constant has a value between zero and unity where unity indicates that the body radiates all energy, often called a black body. Surfaces that are not fully black do not radiate the same amount of energy and ϵ is thereby dependent of the surface colour and finish. [4]

$$q_{radiation} = \epsilon_{12}\sigma A(T_1^4 - T_2^4) \tag{10}$$

$$\epsilon_{12} = \frac{1}{\frac{1}{\epsilon_1} + \frac{1}{\epsilon_2} - 1} \tag{11}$$

2.1.1 Solid Energy Equation

A governing equation for the transport of energy is used in solid heat transfer simulations. In STAR-CCM+ the governing equation is implemented as presented in Equation (12), where ρ is the density, C_p is the specific heat, T the temperature, $\dot{q}''$ the heat flux vector, $\mathbf{v}_s$ the convective velocity of the solid and S_u is the volumetric heat source within the solid that is defined by the user.

$$\frac{d}{dt}\int_V \rho C_p T dV + \oint_A \rho C_p T v_s \cdot da = -\oint_A \dot{q}'' \cdot da + \int_V S_u dV \tag{12}$$

2.2 Thermal Contact Resistance

When investigating the heat transfer between different bodies and materials in contact, the TCR plays a great role. Perfect contacts between materials are never found because of their surface roughness. It results in conduction at the solid contact points and conduction through the gas that is found in the voided areas. The conductive rate within gases is smaller than between solid materials and because of the loss in contact, a temperature drop is created. Different surface roughness will give different temperature drops, the TCR for two materials in contact is used to predict the temperature drop between them. [4]

2.3 Computational Fluid Dynamics

CFD deals with the simulation of fluid flow using computational resources. The flow is simulated by solving a set of equations that ensure the conservation of mass, momentum and energy, *section 2.3.1*. An analytical solution to these equations is not available for most flow cases and therefore they have to be solved numerically [6]. Because of this, the region of interest needs to be divided into discrete elements at which the equations can be solved. This is done through the use of a mesh.

A fluid flow can either be laminar, in transition or turbulent. Turbulence is often described as a chaotic, seemingly random flow with whirls or eddies of different sizes [6]. Most engineering flows experience some form of turbulence and it is therefore important to include turbulent behaviour in flow simulations [6]. Turbulent flows are more difficult to calculate than laminar and additional equations are often added through use of numerical techniques. The turbulence is modelled and resolved to different degrees for the different techniques. For example RANS, *section 2.3.3*, models all of the turbulence while URANS, *section 2.3.3*, resolves smaller parts of the unsteady behaviour of the flow. Detached Eddy Simulations (DES) and Large Eddy Simulations (LES) resolve some of the larger eddies and have an increase in computational cost in comparison to RANS and URANS. There is also Direct numerical simulation (DNS) that resolves all turbulence and therefore has a significantly larger computational cost compared to the previously mentioned numerical techniques. DNS is also the only method for resolving the turbulence that does not use additional equations, but resolves the turbulence directly from the governing equations [7]. Neither DES, LES or DNS were considered in this thesis.

When simulating fluid flow there are a lot of different methods and solver setups available, which will affect the simulation results. For example, different turbulence models that capture the characteristics of the flow in different ways can be used. The choice of turbulence model is therefore dependent on the type of flow that is considered. In this thesis the Shear stress transport (SST) $k-\omega$ and Realizable $k-\varepsilon$ (RKE) Two-layer were used. The models and the need of a discretized mesh are described in *section 2.3.3.2, 2.3.3.1* and *2.3.2*.

2.3.1 Governing equations

The governing equations govern the flow throughout the entire domain, in this thesis the compressible form of the equations were used since a Mach number above 0.3 was considered [8]. The continuity equation, Equation (13), ensures the conservation of mass where t is the time and $\mathbf{v}$ is the continuum velocity containing the velocities u, v, and w

in the x-, y- and z-direction. The momentum equation, Equation (14) that represents the momentum equations in each flow direction, ensures the conservation of momentum where p is the pressure, $\mathbf{I}$ the identity matrix, $\mathbf{T}_V$ the viscous stress tensor and $\mathbf{f}_b$ contains the contributions from body forces, for example gravity. The energy equation, Equation (15), ensures the conservation of energy where E is the total energy, $\mathbf{q}$ is the heat flux and S_E the energy source. [9]

This forms a set of equations that contain five equations and six unknowns which means that an additional equation is needed in order to close the system. Because of this, an equation of state (EoS) is added. There are several possible EoS but one of the most common is the ideal gas law, Equation (16), which relates the pressure to the density and temperature.

$$\frac{\partial \rho}{\partial t} + \nabla(\rho \mathbf{v}) = 0 \tag{13}$$

$$\underset{[i]}{\frac{\partial(\rho \mathbf{v})}{\partial t}} + \underset{[ii]}{\nabla(\rho \mathbf{v} \otimes \mathbf{v})} = \underset{[iii]}{-\nabla(p\mathbf{I})} + \underset{[iv]}{\nabla \mathbf{T}_V} + \underset{[v]}{\mathbf{f}_b} \tag{14}$$

$$\frac{\partial(\rho \mathbf{E})}{\partial t} + \nabla(\rho E \mathbf{v}) = \mathbf{f}_b \mathbf{v} + \nabla(\mathbf{v}(-p\mathbf{I} + \mathbf{T}_V)) - \nabla \mathbf{q} + S_E \tag{15}$$

$$p = \rho R T \tag{16}$$

The momentum, energy and other transport equations consist of similar terms that represent different modes of transport of a variable. Using Equation (14) as an example, the i-term is the rate of change of a calculated variable, ii is transport of the variable by convection, iii is the transport of the variable by pressure, iv is the rate of change of the variable due to diffusion and v is the rate of change of the variable due to sources. [10]

2.3.2 Mesh Discretization

No analytical solution has been found to the governing equations. Instead numerical simulations are used where the equations are solved at discrete points throughout the domain. The domain is discretized into these points using a mesh where different resolutions can be applied. Generally, finer resolution of the mesh gives more accurate results.

The velocity of a flow over a solid surface can be assumed to be zero at the wall due to the wall friction. Because of this, viscous effects decelerates the flow in the near-wall region. This creates what is called a boundary layer (BL), which is a thin region close to the wall where the velocity is lower than that of the free stream. Since the velocity through the BL changes from zero at the wall to the free stream velocity in a very short distance, large velocity gradients are present. Because of these gradients, it is necessary to have a very fine mesh resolution close to the wall in its normal direction in order to resolve the BL. A common way of evaluating if the height of the element closest to the wall is sufficiently low

is to calculate the y^+-value, Equation (17), where y is the first cell height. The y^+-value uses the friction velocity, u_τ, as shown in Equation (18) where τ_w is the wall shear stress.

$$y^+ = \frac{u_\tau y}{\nu} \tag{17}$$

$$u_\tau = \sqrt{\frac{\tau_w}{\rho}} \tag{18}$$

A BL can be divided into three regions, the viscous, buffer and log-law layer. The viscous sub-layer is the small region closest to the wall where viscous effects are dominant, generally it is located where $y^+ < 5$. Outside the viscous sub-layer the buffer layer is located, $5 < y^+ < 30$, where both viscous and turbulent stresses affect the flow. Furthest from the wall the log-law layer is found, $30 < y^+ < 500$, which is where turbulent stresses have the largest effect on the flow. [6]

2.3.3 Reynolds-averaged Navier Stokes Equations

As previously described in *section 2.3*, numerical techniques are generally needed to simulate the turbulent flow. One of the most common choices is a RANS model since it is computationally cheap and the level of turbulence resolution is sufficient for most engineering flows [6].

The RANS equations that are implemented in STAR-CCM+ are based on a Reynolds decomposition and subsequent time-averaging of the Navier-Stokes equations. Reynolds decomposition, Equation (19), is the splitting of a flow parameter ϕ into a time-averaged, $\bar{\phi}$, and a fluctuating, ϕ', part. Applying this decomposition and time averaging the governing equations, Equation (13) to (15), produces the compressible RANS equations, Equation (20) to (22) where $\mathbf{T}_{RANS}$ is a stress tensor defined as in Equation (23). [11] [12]

$$\phi = \bar{\phi} + \phi' \tag{19}$$

$$\nabla(\bar{\rho}\bar{\mathbf{v}}) = 0 \tag{20}$$

$$\frac{\partial}{\partial t}(\bar{\rho}\mathbf{v}) + \nabla(\rho\bar{\mathbf{v}} \otimes \bar{\mathbf{v}}) = -\nabla\bar{p}\bar{\mathbf{v}} + \nabla(\bar{\mathbf{T}}_V + \mathbf{T}_{RANS})\bar{\mathbf{v}} + \mathbf{f}_b \tag{21}$$

$$\frac{\partial}{\partial t}(\bar{\rho}\bar{E}) + \nabla(\bar{\rho}\bar{E}\bar{\mathbf{v}}) = -\nabla\bar{p}\bar{\mathbf{v}} + \nabla(\bar{\mathbf{T}}_V + \mathbf{T}_{RANS})\bar{\mathbf{v}} - \nabla\bar{\mathbf{q}} + \mathbf{f}_b\bar{\mathbf{v}} \tag{22}$$

$$\mathbf{T}_{RANS} = -\rho \begin{pmatrix} \bar{u'u'} & \bar{u'v'} & \bar{u'w'} \\ \bar{u'v'} & \bar{v'v'} & \bar{v'w'} \\ \bar{u'w'} & \bar{v'w'} & \bar{w'w'} \end{pmatrix} + \frac{2}{3}\rho k\mathbf{I} \tag{23}$$

Due to the appearance of additional terms in form of the Reynolds stresses, located in the fourth term in the momentum equation, there are more unknowns than equations which means that the system has a closure problem. The closure problem is solved by modelling the Reynolds stresses and there are different approaches to this. The most common one is to model them using Boussinesq's hypothesis [6], which approximates the size of the

Reynolds stresses using the mean rates of deformation. Since the turbulent viscosity, μ_t, and the turbulent kinetic energy, k, then appear in the equation, they have to be modelled. There are several different RANS models which calculate these two terms using different equations, in this thesis the RKE Two-layer and SST $k-\omega$ models were used, *section 2.3.3.1* and *2.3.3.2*. [12] [6]

There is also the unsteady formulation of the RANS equations, URANS, in which the first term in the original governing equations, the time-derivative, is retained [12]. This introduces a time derivative which allow the largest scales to be resolved. However, since URANS is based on time-averaged equations all small fluctuations will still be time-averaged, this is called scale separation. [13]

2.3.3.1 Realizable $k-\epsilon$ Two-layer

The $k-\varepsilon$ models are two-equation models that includes transport equations for the turbulent kinetic energy and its dissipation rate, ε. It gives reasonable results for boundary layer and free stream flows although it is limited in flows that contains large separations and a high mean shear rate. The limitations are caused by the eddy viscosity being over predicted by the eddy viscosity formulation of the model. The Realizable $k-\varepsilon$ is developed from the Standard $k-\varepsilon$ and it has improved formulations for the transport equations of the dissipation rate and eddy viscosity. The developed formulation ensures that the non-physical behaviour of the mean strain rate that can appear in the Standard $k-\varepsilon$ is prohibited by making the normal stresses positive. [14]

The two-layer version of the RKE model is a STAR-CCM+ specific variant of the RKE model that has a larger flexibility when considering the mesh that is used. The RKE model recommends a $y^+ > 30$ while the Two-layer model gives reasonable results with a y^+ below or around unity because of the additional wall functions of ε and μ_t that are applied in the layer closest to the wall. The Two-layer model is also said to give the smallest errors in comparison to other versions of the $k-\varepsilon$ models when having $1 < y^+ < 30$. [15]

2.3.3.2 Shear Stress Transport $k-\omega$

The Shear stress transport $k-\omega$ model is developed from the Standard $k-\omega$ model. The standard $k-\omega$ model results in a good prediction when applied in the boundary layer, the viscous-dominated region included. A disadvantage with the standard $k-\omega$ model is that it is sensitive to the turbulent kinetic energy and the turbulence frequency, ω, in the free stream. Other turbulence models, such as $k-\varepsilon$, better models k and ω in those regions. In order to improve the applicability in the free stream, SST $k-\omega$, was created. A blending function that includes wall functions was introduced which enables the transport equation for the turbulent kinetic energy's dissipation rate, ε, to be used in the free stream while the transport equation for ω is used close to the wall. The blending function operates such that it is unity in the near wall region, activating the $k-\omega$ model, and then transitions to zero in the free stream, activating the $k-\varepsilon$ model [16]. The SST $k-\omega$ is therefore widely used due to its accurate prediction of the boundary layer characteristics and in the free stream. The $k-\omega$ models are also a good choice of turbulence models where adverse pressure gradients exists which is the case in many aerodynamic flows. The mesh requirement for a $k-\omega$ model that resolves the BL is to have $y^+ < 1$ [17]. [12] [18]

2.3.4 Time Discretization

When performing transient simulations a time step is required and the choice of time step can impact the solution in both computational cost and accuracy. A common approach is to find a time step through use of the CFL number, Equation (24), where u is the velocity, Δt the time step and Δx the grid size [19].

$$CFL = \frac{u\Delta t}{\Delta x} < 1 \tag{24}$$

As the CFL number indicates, the time step can be decided through the use of the velocity and grid size. By keeping the $CFL < 1$ through the whole domain information in the flow will not be transported further than one cell length per time-step. When higher CFL numbers are used, some information might be lost since it travels beyond the immediate neighbours of a cell. A higher CFL number will however result in less computationally heavy simulations since the flow is less resolved in time, although the cost of this might be a loss in accuracy. The choice of time step is thereby often a trade-off. Since a non-uniform grid is often used, the CFL number can vary a lot between different regions in the domain. It can therefore be costly to use a small CFL number. By having a CFL number above one, errors are introduced but might be negligible if the areas are small and limited in number. [20] [21]

3 Method

In this section the method used during the thesis is described. In Figure 1 a flowchart of the method can be seen. The box *future work* in the flowchart represent continued work where the solid and fluid models can be combined and CHT simulations can be performed. Simulations were performed in the software STAR-CCM+ which uses a finite volume method. The solid simulation model was verified by performing a mesh analysis and then validated towards both stationary and transient experiments. The experimental setup is described in *section 3.1* and the method for the verification and validation of the solid model is described in *section 3.2*.

There was no possibility to validate the fluid model but verification was performed through a mesh analysis of a model representative of full size aircraft, further called the global model. Because of the limited time frame for the thesis a smaller model, further called the local model, was used in most of the CFD investigations where boundary conditions (BC) from the global model were used. A domain size investigation of the local model was performed to examine to which extent the boundaries of the fluid domain limited the fluid flow and its turbulent behaviour. The method used for the fluid domain is presented in *section 3.3*.

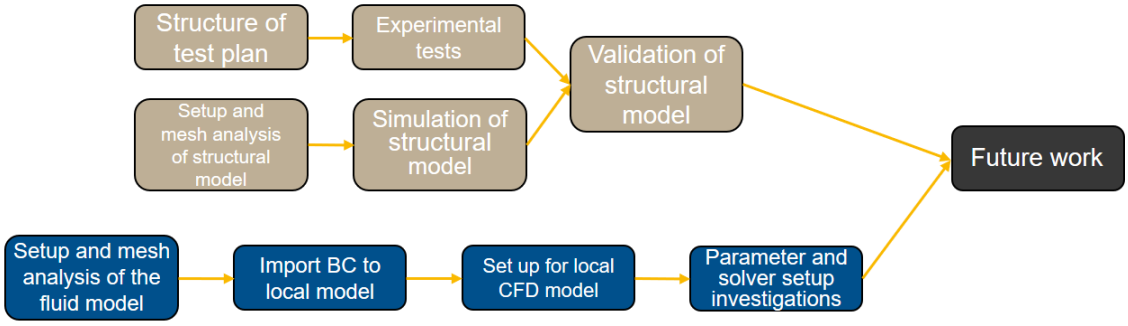

Figure 1: Flowchart of the method.

3.1 Solid Experiments

The physical test section, Figure 2, was used in thermal experiments to validate the solid simulation model. As can be seen, a primer had been applied to almost all surfaces of the test section. Resistors of model RND WD 200/10R F1752, Appendix A, were used to apply a heat source to the physical model and thermocouples of Type K were used to measure the temperatures. During an earlier thesis work at SAAB AB [22] thermocouples of type K had been constructed, 32 of these were rewelded and used for measuring in this thesis work. To investigate the accuracy of the thermocouples they were tested together in room temperature. The largest measured difference between the thermocouples was 0.2 $^{\circ}C$, which was assumed sufficiently low for the experimental tests. At higher temperatures, which were used in the experiments, the thermocouple error was assumed to be sufficiently small as well. The assumption was made since the Type K thermocouples are designed to be able to measure temperatures up to 1250 $^{\circ}C$ [23], which was significantly higher than the temperatures used in the experiments. This was also coherent with experiences from staff at SAAB AB. The external screws that fastened the larger plates as seen in Figure 2 were tightened with approximately 6 Nm.

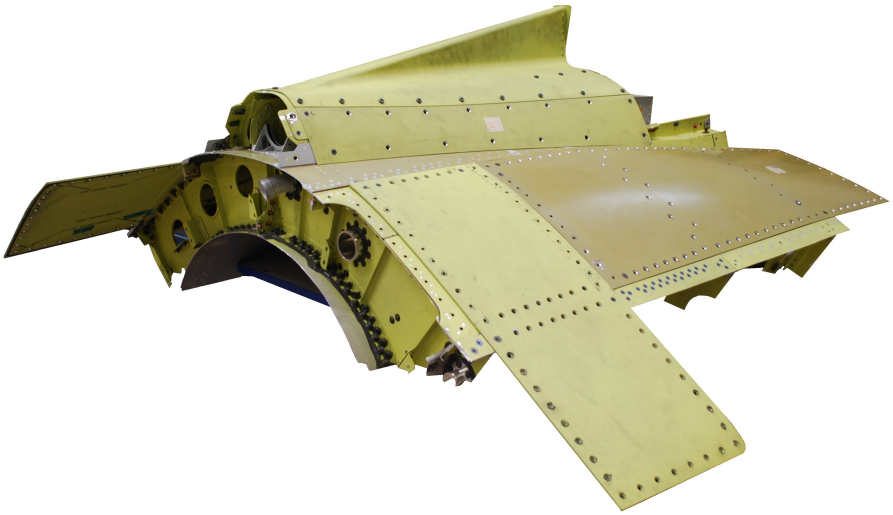

Figure 2: The physical test section used in the heat transfer experiments.

3.1.1 Temperature Boundary Conditions

When performing the experimental tests, temperature measurements had to be performed close to the resistors in order to set realistic boundary conditions in the solid simulations. Initial tests revealed that the contact surface between the resistor and aircraft skin varied depending on the position of the resistors due to the different curvatures of the aircraft. As a consequence the heat flux applied on the aircraft surface would be difficult to approximate to use as a boundary condition in the simulations. Instead the temperature distribution on the aircraft surface was used.

Pretests were performed where the temperatures at the four corners of a resistor, blue points in Figure 3, were measured both at the top and bottom side of a thin plate of the aircraft structure, the overhang to the left in Figure 2. The thin plate was chosen because of its minimal contact with other parts in order to reduce the conduction. These measurements were used to calculate an average temperature gradient through the skin of the aircraft.

Due to variation in contact surface for different resistor placements, the temperature distribution on the aircraft surface was measured for each resistor in each experimental test performed. Temperatures were measured according to Figure 3. Since the temperatures could not be measured directly at the surface between the skin of the aircraft and the resistor, measurements were done at the corners of the resistors on the top side of the plate, blue points in Figure 3. Measurements were also performed directly below the resistor on the bottom side, red point in Figure 3. The previously calculated gradient was then used together with the measurement on the bottom side of the plate to interpolate the temperature on the top surface. This temperature was then used as a BC at a circular surface in the middle of the resistors contact surface, *Inner BC* in Figure 4. The average of this temperature and the temperatures measured at the four corners for each experimental test were used as a temperature BC for the remaining resistor contact surface, *Outer BC* in Figure 4. The contact surface was in all cases assumed to be the same size as the resistor.

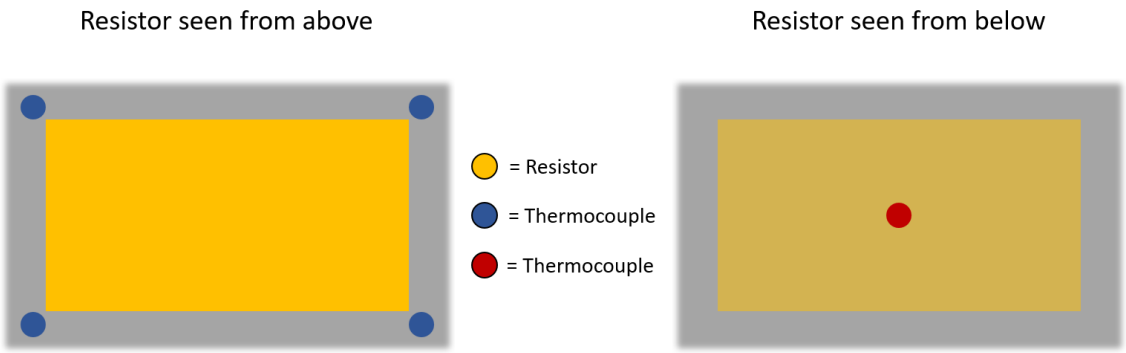

Figure 3: Placement of the thermocouples on both sides of the thin plate in relation to the resistors.

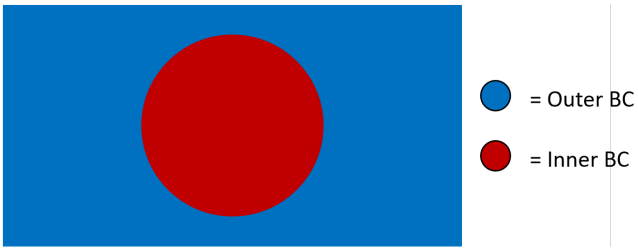

Figure 4: Shape and placement of temperature boundary conditions used in simulations.

3.1.2 Validation Experiments

Experiments were performed to obtain both stationary and transient results for the validation of the solid model. The purpose of the stationary experimental results was to validate the simulation setup and resulting heat distribution. The transient results were used as an additional validation of the results.

3.1.2.1 Steady Validation Method

Steady results were obtained by running the experiment until constant temperatures had been reached. This was done by monitoring the temperatures in the measuring software used, HYDRA. It was not possible to set a convergence criteria in the software, however the plots were ensured relatively stable for at least 30 minutes before measuring the final temperatures. During those 30 minutes small oscillations were found in the temperatures for all thermocouples. The average difference between the maximum and minimum values were below 3 % and the maximum difference at 8 %, however, 50 % of the thermocouples had differences of less than 2 %.

For the stationary results, 4 resistors and 20 thermocouples were used. The placement of the resistors as well as the thermocouples that measured on the top side of the structure can be seen in Figure 5. As can be seen in the figure, the thermocouples were fastened using blue tape. The reason for the successively increasing distance between the resistors, as seen from left to right, was to create different temperature distributions since resistors placed closer together increase the temperature in the structure. The resistors were also placed to cover areas both with and without underlying structure directly beneath them.

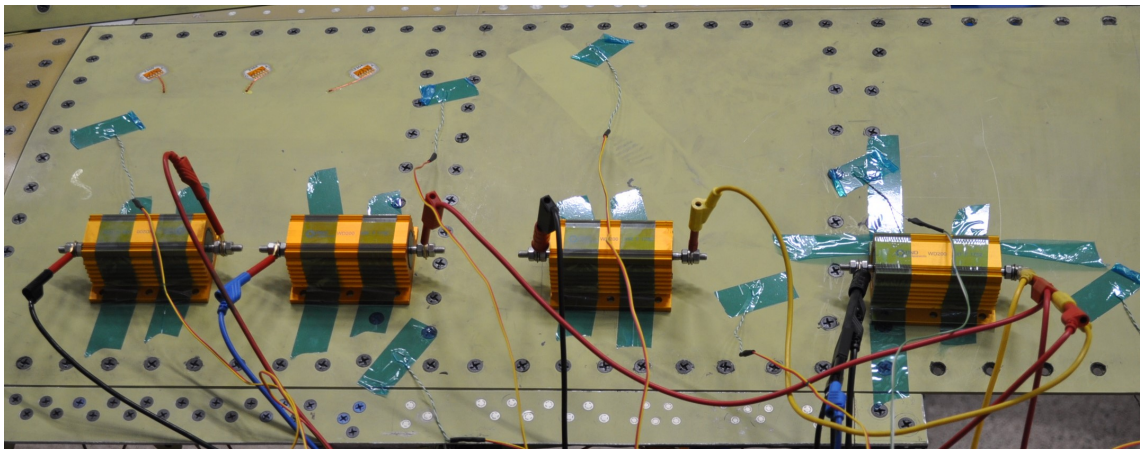

Figure 5: Placement of resistors and the thermocouples on the top skin of the physical test piece during the stationary validation tests.

Four of the thermocouples were placed directly below the four resistors and their temperatures were used to determine the boundary conditions in the validation simulations, as explained in *section 3.1.1*. The remaining thermocouples were evenly scattered on top and below the skin structure of the test section but also on the inner frame. When the temperatures had become stable, one thermocouple was shortly placed at each corner of all the resistors measuring the temperatures which were also used to determine BCs in the simulations. This meant that the corner temperatures were not measured at the exact same time.

3.1.2.2 Transient Validation Method

The transient results were obtained by first heating a resistor until it reached an equilibrium temperature away from the test section. It was then quickly transferred to and fixated on the test section and the data collection for the transient results began. The resistor that was placed as the second resistor from the left in Figure 5 was used for the experiment. The reason for this was that the time difference between the application of different resistors would have introduced a source of error into the transient results which was undesirable.

All thermocouples were kept at their original positions except for three that were originally located far from the resistor. One of them was moved to the top of the resistor to monitor its temperature when it was heated away from the test section. This was done to identify when the resistor had reached a sufficiently high equilibrium temperature. The other two were placed at the upper right and lower left corner of the resistor to use for BC in the simulations. This meant that two corner measurements were used for the BC determination compared to four measurements as was the case for the steady results.

3.2 Solid Simulations

In this section, the method for the solid simulations is presented. Before the simulations began, simplified calculations to investigate the effect of radiation were performed. The reason for this was that radiation is computationally heavy to simulate and it was therefore of interest to see if it could be neglected [24]. All three heat transfer modes were considered in the calculations to attain each percentual contribution to the heat transfer.

Through the use of temperatures found in the experimental setup as well as heat transfer parameters of air and an aluminium alloy in Equation (1)-(3), (5) and (4)-(10), calculations were made as in Equation (25)-(34). Since aluminium alloy was the most predominant material in the solid test rig the simplification of using it in these calculations was made. This introduced an error since the physical model also consisted of steel and titanium. The calculations were performed using equations based on an individual flat plate of aluminium where natural convection, conduction and radiation were considered, where the surroundings were assumed as white walls. However, in the experimental setup most parts were in contact with other parts, which the calculations did not take into consideration. Because of the geometrical variations in the solid structure, the calculated heat transfer coefficient was an average of Equation (4) and (8)-(9). The calculations resulted in that convection was the dominant heat transfer mode while thermal radiation had the least effect on the heat transfer, Table 1.

The combined emissivity constant, Equation (11), was unknown for the solid surface and environment, it was therefore approximated to 0.8. This equates to surface emissivity constants of 0.89 for both radiating surfaces which was a conservative value considering the relatively bright colours of the test piece and the surrounding walls.

$$q_{conduction} = -237 \cdot 0.5 \cdot 4 = -474.00 \ \ W/m^2 \tag{25}$$

$$q_{radiation} = 0.8 \cdot 5.67 \cdot 10^{-7} \cdot 0.5(T_s^4 - T_\infty^4) = 114.77 \ \ W/m^2 \tag{26}$$

$$Pr = \frac{1006 \cdot 1.83 \cdot 10^{-5}}{0.0260305} = 0.71 \tag{27}$$

$$Gr_L = \frac{9.82 \cdot 0.01 \cdot 128.4 \cdot 0.71^3}{(1.52 \cdot 10^{-5})^2} = 1.93 \cdot 10^{10} \tag{28}$$

$$Ra_L = Gr_L Pr = 0.71 \cdot 1.93 \cdot 10^{10} = 1.37 \cdot 10^{10} \tag{29}$$

$$Nu_{\ heat\ upwards} = 0.16 \cdot (1.37 \cdot 10^{10})^{1/3} = 382.85 \tag{30}$$

$$Nu_{\ heat\ downwards} = 0.58 \cdot (1.37 \cdot 10^{10})^{1/5} = 61.80 \tag{31}$$

$$Nu_{\ vertical\ plate} = 0.55 \cdot (1.37 \cdot 10^{10})^{1/4} = 195.19 \tag{32}$$

$$h = \frac{(382.85 + 61.8 + 195.19) \cdot 0.0260305}{3 \cdot 0.71} = 8.34 \ \ W/m^2K \tag{33}$$

$$q_{convection} = 8.34 \cdot 0.5 \cdot 128.4 = 535.43 \ \ W/m^2 \tag{34}$$

Table 1: Heat transfer contribution based on simplified calculations. Convection had the largest contribution while radiation had the smallest.

Convection [%]	**Conduction** [%]	**Radiation** [%]
48	42	10

Since radiation was shown to only contribute with 10 % of the heat transfer, even though the values and assumptions were very conservative, and that the operational temperatures were far below values where radiation starts playing a more significant role, according to [25], the thermal radiation was considered negligible. An additional investigation was performed to see to which degree the thermal radiation affected the results, *section 4.1.1*.

3.2.1 Pre-Processing

A solid geometry section of a fighter aircraft was given and then adapted to represent the physical test section by cutting off parts from it, see Figure 6 for final geometry. It was important to note that different series of the fighter aircraft were used in the physical and simulated setup which resulted in some dimensions and geometrical characteristics to differ. The inner frame was for example cut shorter in the physical model compared to the simulated model, this was however in a region far away from where the heat was applied which should reduce its effect on the results. This was also the case for the other geometrical differences. Based on this, the experimental and CAD models were assumed to be sufficiently similar to enable an accurate validation of the solid simulation model.

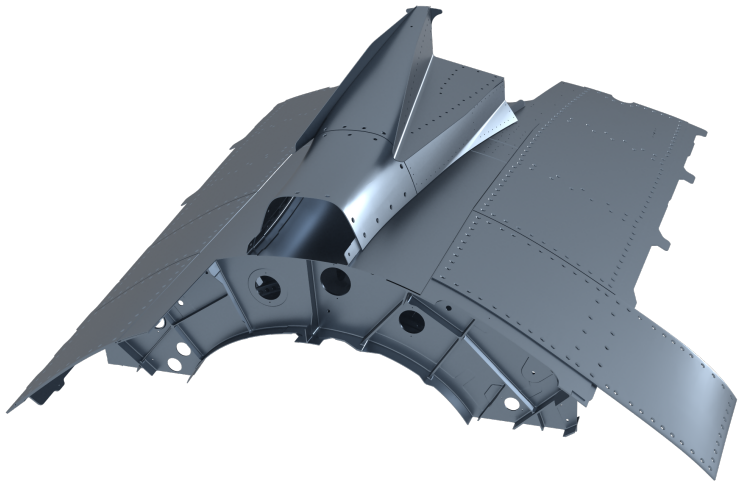

Figure 6: Solid geometry used in simulations.

The main types of materials that were found in the aircraft section were titanium, steel and aluminium alloys which had thermal conductivities spanning from around 5-10 W/mK, 15-20 W/mK and 90-130 W/mK respectively. The materials were given in a table with their associated part, which were read into the simulation model using a Java script. However, some parts were not assigned any material or consisted of materials that did not exist in SAAB's material database in STAR-CCM+. In those cases materials with similar characteristics were chosen. This resulted in the experimental setup and the simulation model also having different materials in some parts, which could create and affect thermal differences in the validation process. These effects should however be small since similar characteristics were present in the replacement materials.

The given geometry for the simulations consisted of parts with small gaps between them. To simulate the heat transfer between the parts that should have been in contact, *Weak contacts* were created and used in combination with *Mapped contact* and *Contact interfaces*. Through the use of *weak contact creator* the contact surfaces were identified and contacts were created based on tolerance values [26]. Interfaces were then created on these contact surfaces. For the parts with the smallest gaps between them, contact interfaces were created which creates a conformal mesh [27]. For the larger gaps where different mesh resolutions were present, *Mapped contact interfaces* were used since they create an interface with a non-conformal mesh [28]. The created interfaces could then transfer information during simulations and the parts would in that way behave as a continuous structure at the created contact interfaces [29]. Since the parts in contact had different geometries and mesh resolution it was impossible to create perfect contact interfaces and errors would therefore be introduced in the simulations. The affected areas were however assumed small enough to not significantly impact the accuracy.

3.2.2 Solver Setup

The general settings used in the mesh analysis and the stationary validation simulations are presented in Table 2. The radiation simulation used the presented setup as a base but also included radiation as described in *section 3.2.4.1*. The transient simulation also used the setup in Table 2 but with a transient formulation. The BC:s varied between the different simulations and are described in each section, respectively.

Stationary simulations were used in all simulations except the transient validation simulations. The reason for this was that steady simulations provide a large amount of information about the investigated problem for a low computational cost. Transient simulations were however performed to further validate the chosen parameter values.

Table 2: The settings used for the solid simulations performed in STAR-CCM+.

Setting Category	**Chosen Setting**
Time	Steady
Space	Three Dimensional
Material	Multi-Component Solid, Multi-Part Solid
Equation of State	Constant Density
Optional	Coupled Solid Energy, Gradients, Solution Interpolation

3.2.3 Mesh Sensitivity Analysis

A mesh sensitivity analysis was performed to verify the solid simulation model. A polyhedral mesh was used in combination with the function *Thin mesher*, which creates prism elements in the thickness direction of thin parts which better captures the temperature gradient. In STAR-CCM+ these prism elements are called *Thin layers*. The mesh analysis was performed having two parts with a constant temperature that heated up the surrounding parts. The resulting temperature distribution is shown in Figure 7, where the temperature increases in the direction of blue to red. All other external surfaces had settings of natural convection with a heat transfer coefficient of 8.34 W/m^2K.

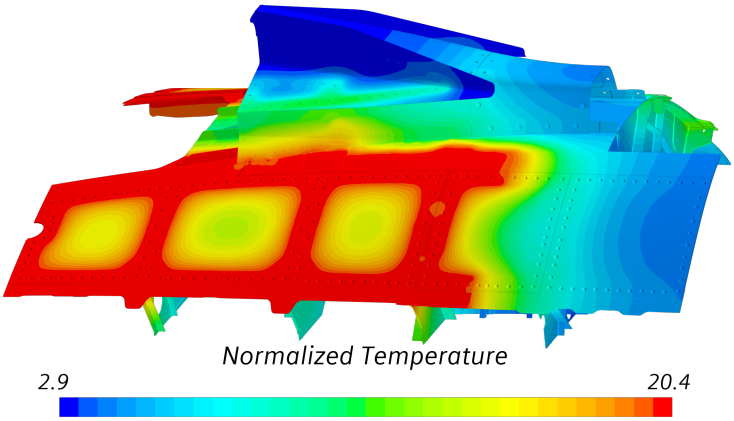

Figure 7: Resulting temperature distribution used in mesh analysis simulations.

Four different meshes were simulated and compared, Table 3. Throughout the mesh analysis the cell count was increased with about 40 % to make sure that if mesh independence had not yet been reached, a significant difference in the results would be present. To make sure that all simulations had stabilized, the maximum and average surface temperature in the two skin plates were monitored. A standard deviation of 0.001 degrees over 100 samples had to be reached for the four temperature values. To compare the different meshes the average temperatures of the two skin plates were obtained as well as the temperature at two lines, which were created by using line probes. The line probes were placed along the skin and the frame of the geometry. The lines had 80 evenly distributed points which were evaluated at the closest node. The normalized average temperatures in the two skin plates and the percentual change between the four meshes can be seen in Table 4. The results showed that the difference in percentage mostly decrease with an increase in cell count. The normalized temperatures along the lines showed little differences between the meshes, Figure 8. To obtain a quantitative difference of the meshes the maximum and average differences between each mesh and its succeeding mesh were obtained in the lines, Table 5, where both can be seen to be lowest for Mesh 2 in comparison to Mesh 3.

The results did not differ significantly between Mesh 1 and Mesh 2, it was however noted that the coarse elements in Mesh 1 were unable to correctly represent some parts of the geometry. Because of this, and that there were no large difference between any meshes, Mesh 2 was used in the remaining simulations.

Table 3: The four different mesh setups used in the mesh analysis, where N is the number of thin layers and the cell count increase is in relation to the preceding mesh.

Mesh	**N**	**Cell Count**	**Cell Count Increase**	**Surface Base Size [mm]**	**Surface Minimum [mm]**	**Volume Base Size [mm]**
Mesh 1	2	1 208 168		54	1.836	54
Mesh 2	2	1 719 179	42 %	40	1.360	40
Mesh 3	3	2 624 259	53 %	36	1.224	36
Mesh 4	4	3 989 915	52 %	26	0.780	26

Table 4: Normalized average temperatures and the percentual difference to the succeeding mesh in the two skin plates, named 1 and 2. The change in percentage was below 1 % for all cases.

Mesh	Surface Average 1	%	Surface Average 2	%
Mesh 1	18.577	0.06	18.653	0.26
Mesh 2	18.566	0.25	18.603	0.10
Mesh 3	18.613	0.23	18.621	0.02
Mesh 4	18.569		18.618	

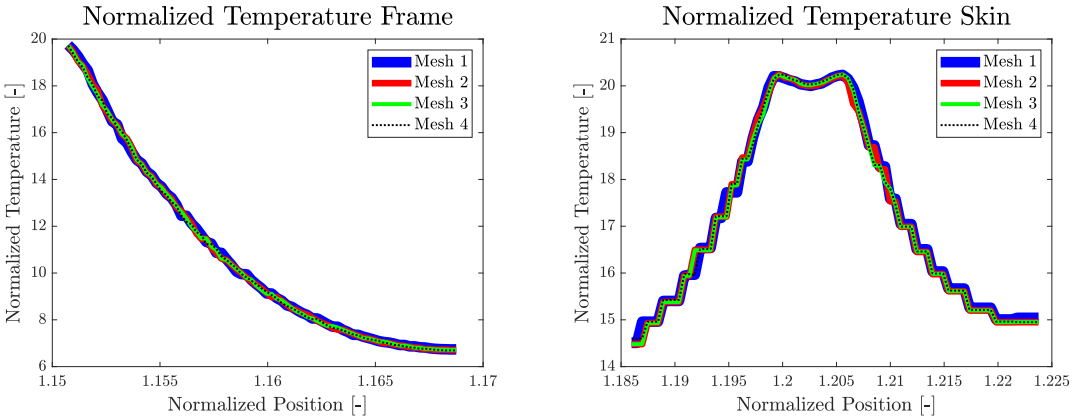

(a) Normalized temperature in the frame.

(b) Normalized temperature in the skin.

Figure 8: Normalized temperature along line probes in the frame and skin of the solid model. No major differences can be seen between the different meshes.

Table 5: Maximum and average percentual differences between the meshes' line probes in the mesh analysis. The differences are calculated by comparing each mesh to the succeeding mesh. The differences were smallest between mesh 2 and 3.

Mesh	Maximum Difference Frame [%]	Average Difference Frame [%]
Mesh 1	2.30	0.59
Mesh 2	1.58	0.30
Mesh 3	2.11	0.47
Mesh 4		
Mesh	**Maximum Difference Skin [%]**	**Average Difference Skin [%]**
Mesh 1	3.34	0.44
Mesh 2	2.09	0.16
Mesh 3	3.27	0.19
Mesh 4		

Since the number of thin layers could affect the heat distribution in thin geometries a small investigation was conducted. Mesh 2, which originally had 2 thin layers, was rebuilt using zero as well as 3 thin layers. These three thin layer setups, which had 0, 2 and 3 thin layers, were then compared to Mesh 3, Table 6. The monitoring of the normalized average temperatures in the same parts as used in the mesh analysis showed that the mesh with

three thin layers resulted in the smallest percentual change while the one with zero thin layers, a mesh consisting of only polyhedral elements, resulted in a significant difference in comparison, Table 7. Temperatures were also measured in the same line probes as used in the mesh analysis. The only clear difference between the use of different number of thin layers was that zero thin layers resulted in larger deviations in the coarser regions of the mesh, Figure 9.

Despite the relatively low difference for both Mesh 2.2 and 2.3 compared to Mesh 3, Mesh 2.3 was chosen to be used in further simulations. The reason for this was that a two-layered thin mesher would only have elements that were in direct contact with an external BC. With three layers, at least one cell in the middle of a thin plate would not be directly affected by the applied BC.

Table 6: Mesh setups used when investigating the impact of number of thin layers, where N is the number of thin layers.

Mesh	**N**	**Cell Count**	**Cell Count Increase**	**Surface Base Size [mm]**	**Surface Minimum [mm]**	**Volume Base Size [mm]**
Mesh 2.0	0	1 575 974	30 %	40	1.36	40
Mesh 2.2	2	1 719 179	42 %	40	1.36	40
Mesh 2.3	3	2 372 294	96 %	40	1.36	40
Mesh 3	3	2 624 259		36	1.224	36

Table 7: Normalized average temperatures for the meshes used in the investigation of the impact of number of thin layers on two solid parts, named 1 and 2. Mesh 2.0 to 2.3 were all compared to Mesh 3 and the impact was decreased with an increase in thin layers.

Mesh	**Surface Average 1**	**%**	**Surface Average 2**	**%**
Mesh 2.0	18.970	1.88	18.785	0.87
Mesh 2.2	18.566	0.25	18.603	0.10
Mesh 2.3	18.584	0.15	18.616	0.03
Mesh 3	18.613		18.621	

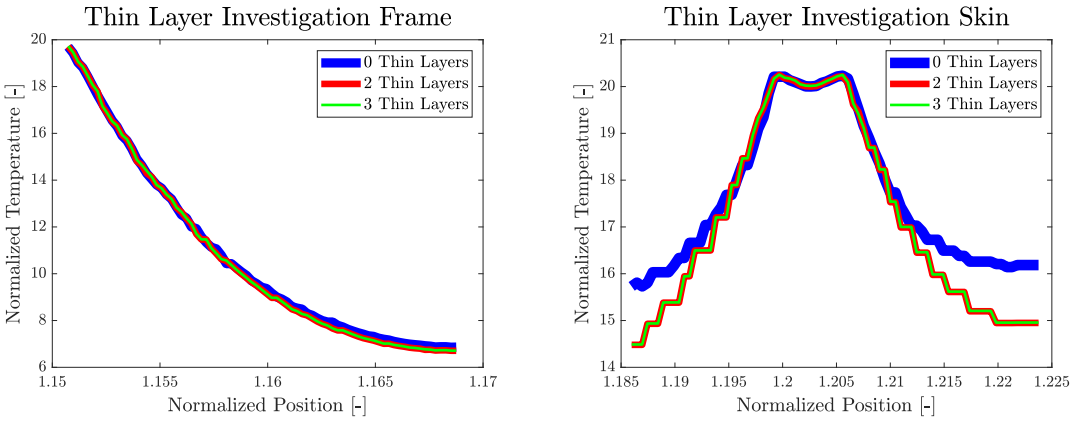

(a) Normalized temperature in the frame.

(b) Normalized temperature in the skin.

Figure 9: Normalized temperature in the frame and skin when investigating the impact of number of thin layers. The line with zero thin layers differed compared to the other lines in the coarser regions of the mesh.

3.2.4 Validation Simulations

After a mesh had been selected, validation simulations were performed to use in comparison to the experimental validation tests, *section 3.1.2*. When new BCs were set for these simulations however, it became apparent that the mesh contained some problematic elements. Because of this, refinement boxes were created around them. This increased the number of elements with approximately 74 000.

The simulation model was set up to mimic the experiments. Unlike the mesh analysis simulations, BCs were set on the surface of the skin plates as explained in *section 3.1.1*. A natural convection BC was set on the remaining external surfaces.

The temperatures measured by the thermocouples were used to compare the results between simulations and experiments. Point probes were placed at the same positions as the thermocouples in the experimental tests in order to validate the model, red points in Figure 10. Because of the complex geometry of the test rig in combination with the differences between the experimental and simulated geometries, it was difficult to perfectly match the positions of the points in the simulation to the thermocouples in the experiments. This introduced another error to the results from the simulated model but since no extreme temperature gradients were present it should not have affected the results significantly.

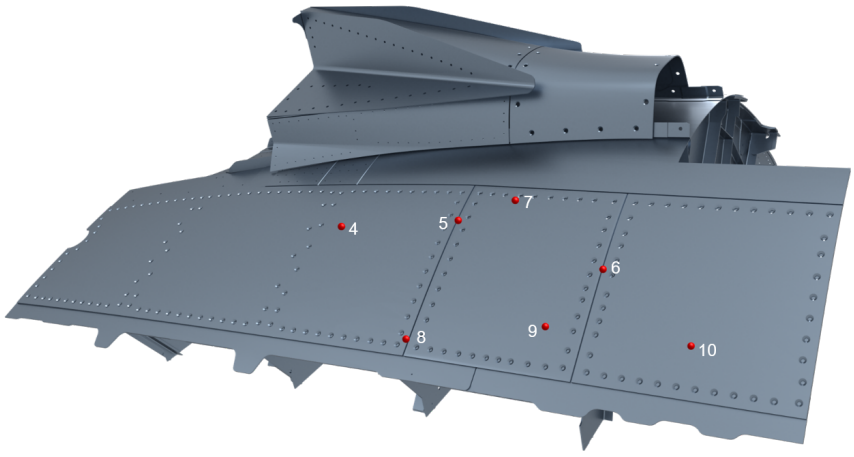

(a) Top view.

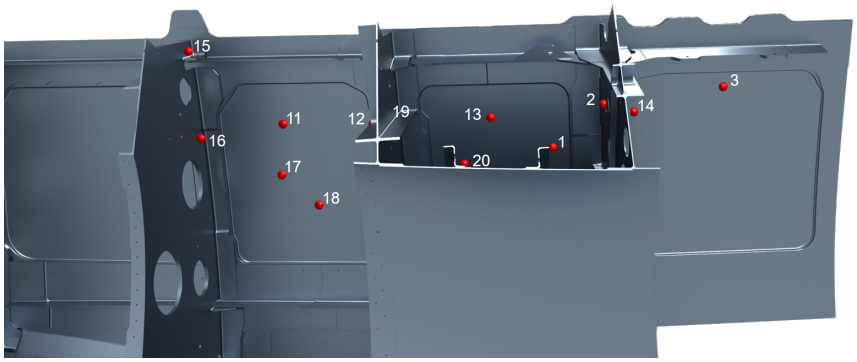

(b) Bottom view.

Figure 10: Top and bottom view of the geometry showing the measuring point positions, red dots, matching the placement of the thermocouples in the experiments. Point 12 is placed on the inner frame directly below one of the resistors and 19 is placed below the flange, they are therefore not visible in b).

The maximum temperature was monitored in four different parts which can be seen in colour in Figure 11, where the middle part consists of two parts with the division being in the middle of it. In the two skin plates which are shown furthest to the left and right, the average temperature was also monitored. When the standard deviation for each of the monitors was below $1 \cdot 10^{-4}$ degrees for 100 consecutive iterations, the solution was deemed converged. A plot of the temperature in the 20 measured points used for the validation study was also investigated to see that the temperatures had become steady. A convergence criterion of $1 \cdot 10^{-4}$ degrees for the standard deviation over 100 consecutive iterations was set for the sum total of the temperatures at these points. The energy residual was also monitored with a convergence criterion set to $1 \cdot 10^{-11}$.

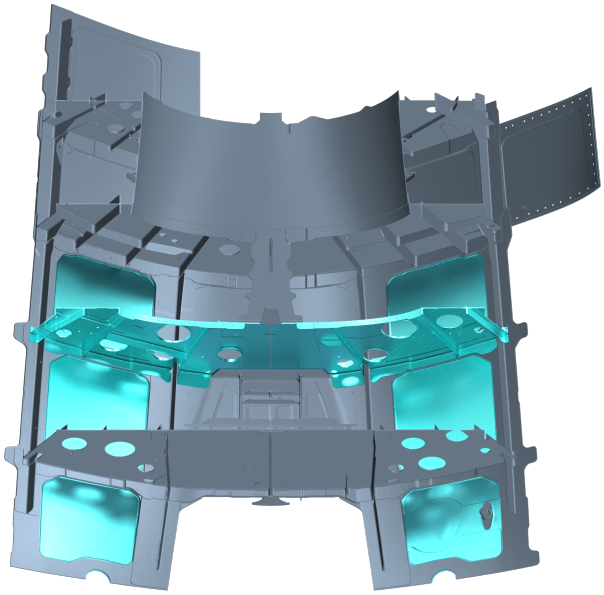

Figure 11: The parts monitored to help gauge convergence, presented in turquoise. The turquoise part stretching from left to right has a division in the middle and therefore consists of two parts.

The TCR between different parts was unknown in the solid model. Similarly the value of HTC was also unknown, although an approximation of it had been calculated to 8.34 W/m^2K in *section 3.2*. Based on this, combinations of TCR and HTC values were investigated and compared with experimental data for the validation of the model. The TCR was also compared to the results of a previous study performed at SAAB AB, [22]. The investigated HTC values were chosen based on the calculated value and then increased and decreased slightly in order to find the values that coincided best with the experimental data. The values of TCR were chosen in a similar way but the starting value was based on [30]. The investigated HTC and TCR values can be seen in (35) and (36) respectively.

$$HTC : \{6.34,\ \ 7.34,\ \ 8.34,\ \ 9.34,\ \ 10.34\} \tag{35}$$

$$TCR : \{1 \cdot 10^{-5},\ \ 1 \cdot 10^{-4},\ \ 5 \cdot 10^{-4},\ \ 1 \cdot 10^{-3},\ \ 5 \cdot 10^{-3},\ \ 1 \cdot 10^{-2}\} \tag{36}$$

3.2.4.1 Radiation

Since radiation was neglected in the solid simulations, it was of interest to investigate the effect of radiation and thereby the introduced error caused by this simplification. The simulation with settings of HTC and TCR that produced results closest to the experimental data was edited to include radiation. The *Surface to surface radiation* model in STAR-CCM+ was used which allows for radiation both between external surfaces of the model and with the environment.

An environmental BC was applied instead of the convective BC used in the validation simulations. The radiation to the surrounding environment was specified using only the room temperature. The convergence criteria used in the validation simulations were also applied for the radiation simulation.

The *Surface to surface radiation* model aggregates the surfaces of boundary elements into larger patches which are then treated as single radiating units when calculating the radiation [31]. No radiation occurs between the elements within a patch and a common view factor, which calculates the fraction of the diffuse radiated light from the patch that reaches another surface [31], is calculated. The patch to face proportion was set to 10 % which corresponds to one face being 10 % of a patch. Increasing the patch to face proportion increases the accuracy of the radiation calculations but also the computational cost [32].

The solid simulations did not require a lot of computational time, this in combination with the fact that only one radiation simulation was needed for this thesis was the reason for running the radiation simulation with a patch to face proportion of 100 %. Two tests were however performed with a patch to face proportion of 5 and 10 % in order to assess the error this would have introduced. The values at the 20 measured points showed that all points differed with less than 0.1 % for patch to face proportions of both 5 and 10 % compared to a proportion of 100 %. This meant that these lower proportions did not introduce any significant errors into the results. The computational cost was reduced with approximately 80 % for the simulations with a patch to face proportion of both 5 % and 10 % compared to the simulation with 100 %.

3.2.4.2 Transient Simulations

The transient simulations were performed by using the simulation with settings of HTC and TCR that produced the results closest to the experimental data as a base, radiation was not included. The time specification was then set to transient and a time step of 0.1 s was used. The BCs were calculated by taking the two measured temperatures at diagonal corners of the resistor and using them twice to represent the four corner temperatures that were used to calculate the BC according to *section 3.1.1*. Since the temperature at the resistor varied with time, a fourth degree polynomial was fitted to the experimental values to approximate the temperature change of the BC. This function was then used as a BC in the transient simulations. A transient simulation was also performed using a lower TCR, $1 \cdot 10^{-4}$ m^2K/W.

3.3 Fluid Simulations

A mesh analysis was performed on a representative model of a full size aircraft, *section 3.3.1*, further called the global model. The results were used as BC in a smaller domain covering the area of interest, the area where the jettisoned air was present. The smaller domain is further called the local model. The inlet and outlet positions were specified by SAAB AB and could not be changed. Since the aircraft extended further than the inlet and outlet of the local model a study of the domain size, adjusting the sides and top of the domain, was performed to make sure that the top and side boundaries of the domain disturbed the fluid flow as little as possible, *section 3.3.2*. It was also investigated whether an extrusion of the outlet contributed to more accurate results and if different BCs on the sides, top and bottom of the domain impacted the accuracy.

Common CFD parameters were investigated to see if the simulation cost could be reduced. The investigated parameters were the increase in y^+ when using All y^+ wall treatment, *section 3.3.3*, as well as the CFL number, where transient simulations were performed,

section 3.3.4. The turbulence model RKE Two-layer was also used in simulations in order to compare it towards the SST $k-\omega$ model.

3.3.1 Global Model Mesh Analysis

The mesh analysis was performed with the setup according to Table 8 where second order schemes were used. The aircraft surface had no-slip wall BC and inlet BCs were set at the engine exhaust and for the jettisoned air where temperature and mass flow were specified for both cases. Free stream BCs were used at all remaining boundaries of the domain where the Mach number was specified to 0.6, the normalized far field temperature to -3.346, the angle of attack to 4 degrees and the gauge pressure relative to the ambient pressure to 0 Pa. A triangular surface mesh was first created which was used as a basis for the volume mesh. In the fluid domain a trimmed mesh was used due to its ability to produce high quality-grids [33] for a low computational cost. The y^+ value was generally below two, while a small percentage was found both below and above two. The model was first run with a y^+ value that was generally below 1 but due to imperfections in the given aircraft structure caused by an earlier wrapping, the solution was not able to converge. This was the same reason for smaller areas of the domain having $y^+ > 2$ as well. A $y^+ < 2$ is however within the STAR-CCM+ recommended range [34], as well as within the viscous sub-layer, when using the *All y^+ wall treatment*. To reach the low y^+ a total of 30 prism layers were used creating a total thickness of 0.0153 m with a stretch rate of 1.2. The element size was refined in critical flow areas. These areas were at the engine exhaust, trailing edge (TE) of the wings, canards and stabilizer, as well as at the area consisting of jettisoned air. The largest refinement was done where hot air was jettisoned since that was the area of interest in this thesis. The other areas were refined to properly resolve the wakes behind the wings, the stabilizer and the jet engine exhaust so that they would not significantly affect the flow in the area of interest.

Table 8: Settings used in STAR-CCM+ when performing the mesh analysis.

Setting Category	**Chosen Settings**
Time	Steady
Viscous regime	Turbulent, RANS
Reynolds-Averaged Turbulence	$k-\omega$ Turbulence, SST $k-\omega$, All y^+ Treatment, Wall Distance
Space	Three Dimensional
Energy	Coupled Energy
Flow	Coupled Flow, Gas
Fluid	Air
Equation of State	Ideal Gas Law
Optional	Gravity, Solution Interpolation

Seven monitors were used to investigate convergence and mesh independence, four were placed at the jettisoned air region and three at the engine exhaust. Velocities and temperatures were obtained in all measure points. Lift- and drag coefficients were also monitored over the entire aircraft to see if the flow was globally stable. Faulty cells in the domain would cause unphysically high and low temperatures in the domain, the maximum and minimum temperatures were therefore monitored and used to remove the invalid cells, 14 cells were removed. To make sure that all simulations had converged, a standard deviation of 0.01 degrees for the temperature and 0.01 m/s for the velocity over 10 samples were

needed to be fulfilled by the four monitors at the jettisoned air. Three different meshes were run which had a cell count and base sizes according to Table 9. The refinement at the engine exhaust was made using three cylinders of different sizes to get a smooth transition in elements and the overall refinement was done using a percentage of factor 2, 4, 8 and 16 of the base size, Table 10.

Table 9: The cell count and base size for each mesh used in the mesh analysis, where the cell count increase is compared to the preceding mesh.

Mesh	**Cell Count**	**Cell Count Increase**	**Base Size [mm]**
Mesh 1	67 733 335		100
Mesh 2	98 386 981	45 %	60
Mesh 3	143 690 559	46 %	45

Table 10: The element size used in the refinement areas presented as a percentage of the base size.

Jettisoned air refinement [%]	**Smallest engine exhaust and canard refinement** [%]	**TE and engine exhaust refinement** [%]	**Largest cylinder at engine exhaust refinement** [%]
6.25	12.5	25	50

The normalized temperatures and velocities obtained at each monitor for each mesh can be seen in Table 11. The maximum and average percentual change for each mesh is presented as well. The monitors with index 1-4 were positioned at the jettisoned air, Figure 12, and 5-7 behind the engine. The results showed that the absolute change between the meshes were similar for all monitors even though the velocities and temperatures were higher at the engine exhaust than at the jettisoned air. The results also showed that the maximum difference in percentage between Mesh 2 and 3 was below 5 % for the temperature and below 9 % for the velocity, while the average was below 2 and 4 % respectively. The reason for the larger difference in the velocity between the two meshes was that monitor 3 and 4 were placed at the transition area between the fast free-stream flow and the slower jettisoned flow, see Figure 13 where the flow increases in direction of blue to red. This meant that refinement in the mesh gave large differences in the measured velocity. Based on that the impact of temperature was more important in the aim of the thesis, the slightly higher difference in velocity was deemed acceptable and Mesh 2 was assumed to be sufficiently accurate for further simulations. Due to the increase in computational cost with larger grids, no larger meshes were investigated.

It was also investigated whether a smaller refinement box could be used at the jettisoned air in order to decrease the number of elements. The results however showed oscillatory behavior at the velocities and no further investigation was conducted.

Table 11: Normalized temperatures and velocities measured at seven monitor points when performing the mesh analysis. It also shows the maximum and average percentage in change for an increased mesh refinement. The change was shown to decrease with an increase in elements and the velocity was shown to be more sensitive to a change of the discretization than the temperature.

Mesh	T_1	T_2	T_3	T_4	T_5	T_6	T_7	**Max** [%]	**Avg.** [%]
Mesh 1	20.32	20.36	11.97	5.41	68.54	67.45	59.91	27.26	5.05
Mesh 2	20.31	20.35	11.27	6.89	68.04	67.61	60.68	4.68	1.45
Mesh 3	20.31	20.35	11.61	6.75	67.85	67.53	57.84		
Mesh	v_1	v_2	v_3	v_4	v_5	v_6	v_7	**Max** [%]	**Avg.** [%]
Mesh 1	4.19	1.17	2.59	9.52	104.65	106.06	105.39	92.50	17.19
Mesh 2	4.39	2.26	2.94	8.70	105.30	105.86	105.65	8.48	3.16
Mesh 3	4.39	2.45	3.17	8.77	105.59	106.00	100.90		

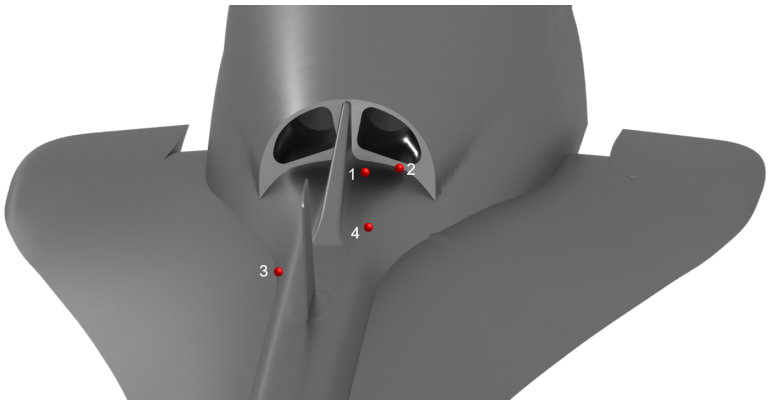

Figure 12: The monitor points' positions at the jettisoned air, numbered 1-4.

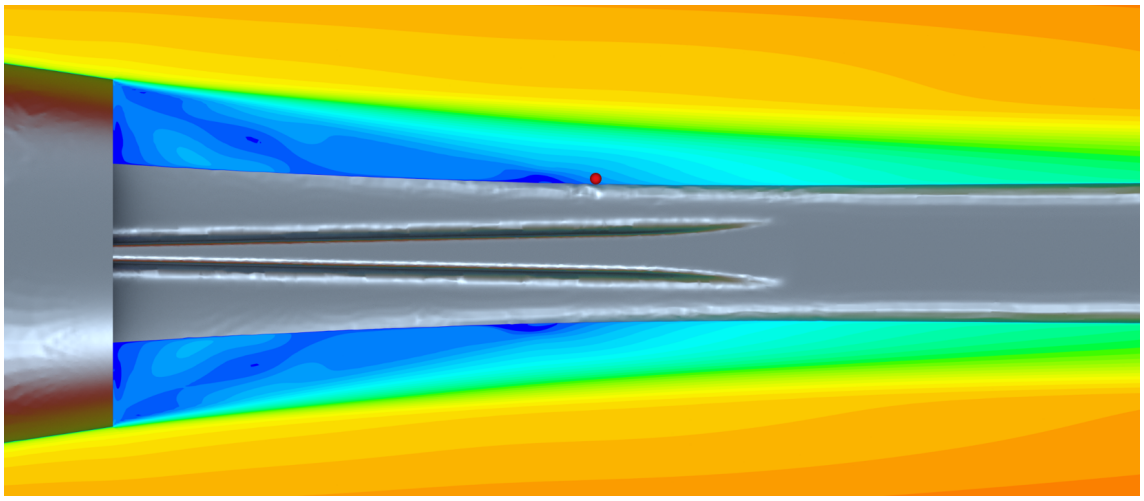

Figure 13: A top view of the position of monitor 3, red point, which is at the transition area of two velocities of different magnitudes.

3.3.2 Local Domain Size

The local domain was tilted 4 degrees to align it with the flow direction as found in the global model, where an angle of attack of 4 degrees was used, Figure 14. The aircraft geometry was kept in the same position as in the global model, meaning that only the external domain was positioned with a new angle. The inlet, outlet and bottom of the local domain were specified by SAAB AB and no change in their position was possible. Instead the positions of the sides and the top were investigated to see the impact on the flow behaviour. The placements of the boundaries are shown in Figure 15. An investigation into the size of the domain, where the width and height was changed, was therefore performed, *section 3.3.2.1*. From the investigations it was apparent that the outlet was positioned in a wake. To enable the turbulence and fluid flow to stabilize before arriving to the outlet, the outlet surface was extruded to see if it could result in more accurate flow behaviour. It was also investigated whether slip walls or free stream BC on the sides, top and bottom of the domain contributed to more accurate results, *section 3.3.2.2*.

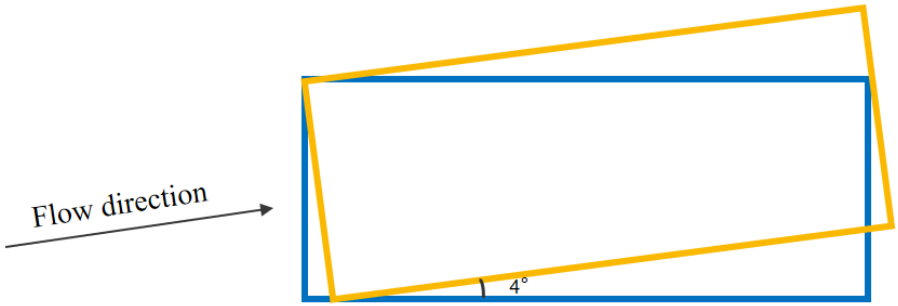

Figure 14: The local domain that was tilted and used in simulations, orange box.

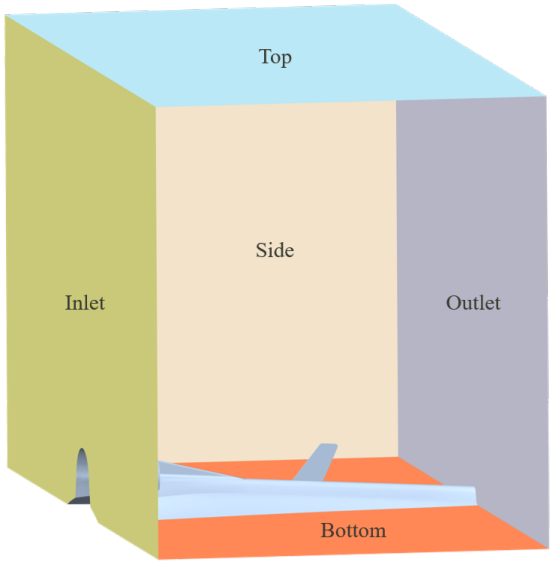

Figure 15: The fluid domain and its specified boundaries.

3.3.2.1 Width and Height

Three geometries were investigated where the smallest box, Box 1, had its sides and top approximately 2 m from the aircraft surface. After that the edges were extruded with 1.5 m for each increase in box size, Box 2 and Box 3. The three sizes investigated can be seen in Figure 16 where the mesh captured by each box is seen as well. The mesh chosen in the mesh analysis for the global model was used without any alterations. The setup used was the same as in the mesh analysis for the global model, Table 8. The inlet had BC from the global model where temperature, velocity, turbulent kinetic energy (TKE) and specific dissipation rate (SDR) were defined. The outlet was set to an outlet pressure BC with 0 Pa in gauge pressure relative to the ambient pressure and TKE and SDR specified from the global model as well. The sides, top and bottom were set to slip walls.

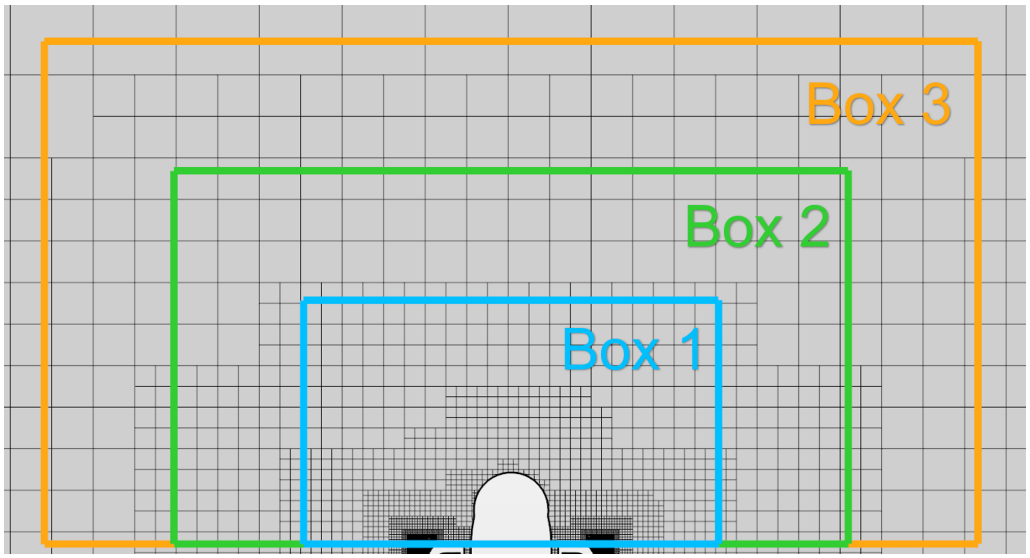

Figure 16: The three box sizes investigated and the mesh each box captured, seen from the front of the aircraft.

To investigate the impact of the box size, the velocity magnitude, temperature and TKE were measured along two lines called y and z-line, Figure 17. The line probes had 800 evenly distributed points that were evaluated at the closest node. All values were compared to the global model, Figure 18 where the normalized values are presented in relation to the normalized position at each line. At the y-line the largest deviations occurred, where Box 1 results in the largest in comparison to the global model while Box 2 and 3 fit well together but not always with the global model. On the z-line all results follow the same trend and mostly fit well together, though the largest deviations could be seen for Box 1 there as well. The results also showed that the boxes underpredicted both the velocity and TKE while the the temperature was overpredicted in comparison to the global model. Based on the results, the size of Box 2 was used in further simulations since no larger improvement was found for a larger box.

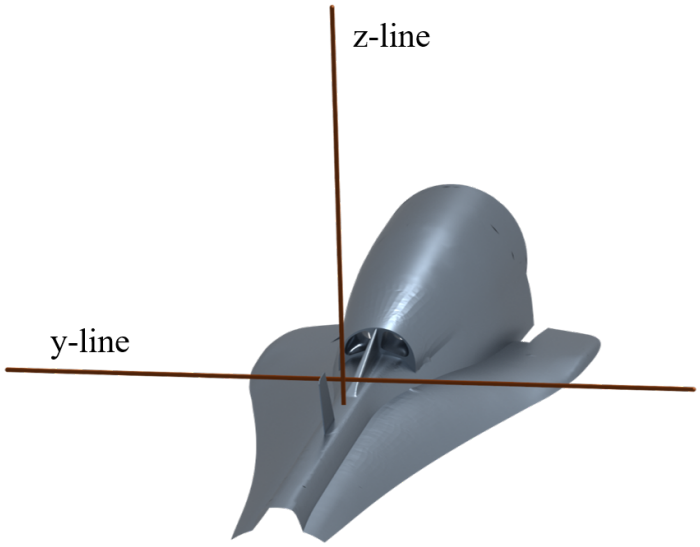

Figure 17: The y and z-lines positions in relation to the aircraft surface.

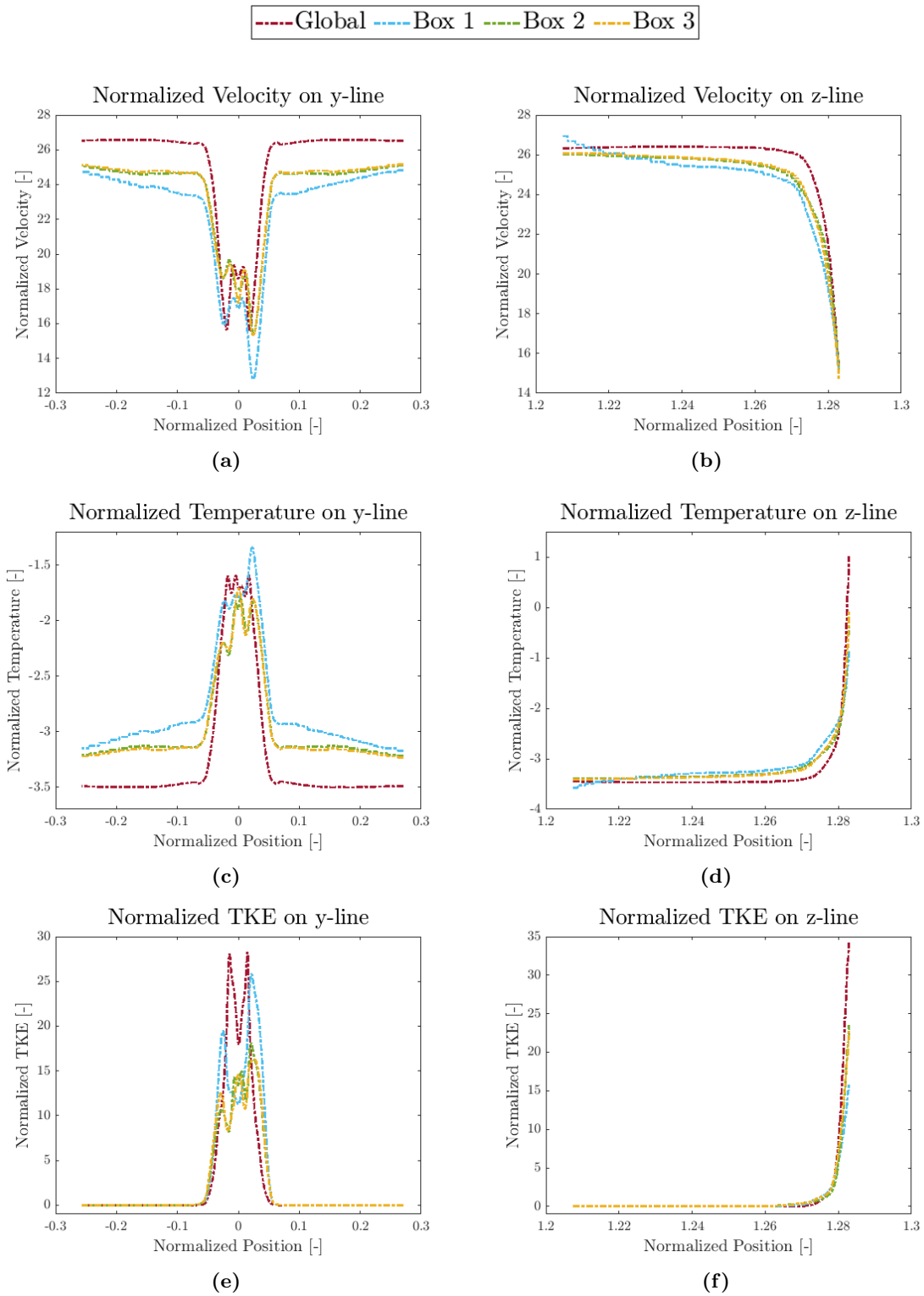

Figure 18: Normalized velocity magnitude, temperature and TKE along two lines, y and z line, where three different box sizes, Box 1, Box 2 and Box 3, were all compared towards the global model. Few differences were shown between Box 2 and 3 while Box 1 had the largest deviations compared to the global model.

3.3.2.2 Domain Length and Boundary Conditions

When investigating the fluid flow behaviour it was apparent that the outlet of the domain was placed in the middle of the wake, meaning that the flow did not have the possibility to fully develop and could have been disturbed by the BC set at the outlet. To enable the flow to develop the outlet surface was extruded 6 m, keeping the geometry and angle of the outlet surface through the whole extrusion, Figure 19 where the original model is shown in (a) and the extruded model in (b). It was important to be aware that since the domain earlier had been tilted 4 degrees while the geometry followed the original coordinate system, it resulted in a slant of 4 degrees in the geometry at the transition to the extruded volume. Two different setups of the extruded model were simulated, one with the same settings as in the local and one where the sides, top and bottom, that were earlier slip walls, had free stream as BC. The Mach number and temperature used in the far field of the global model were used in the extruded model. Similarly, the SDR and TKE that was interpolated at the outlet in the local domain was used on the outlet of the extruded domain as well. It was also investigated whether a pressure outlet BC could be used on all the sides where the TKE and SDR were interpolated from the global model, but because of early divergence in the solution for both steady and transient simulations no further investigations were performed.

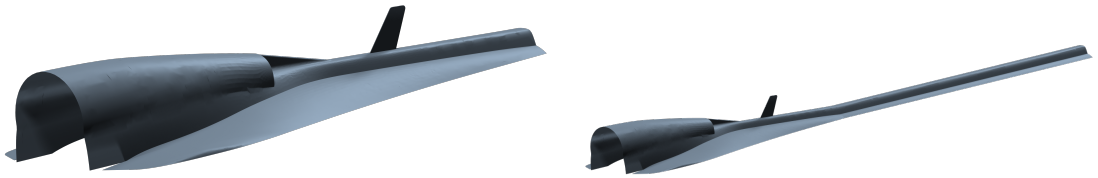

(a) Non extruded model. **(b)** Extruded model.

Figure 19: The original size of the local model as well as the extruded version.

Five line probes with 2000 evenly distributed measure points, Figure 20, were used to measure the velocity, temperature and TKE for the extruded models as well as the non-extruded model in order to see which resulted in most similar behaviour to the global model. The results for all three parameters showed that the largest deviations were at line 2 and 3 and smallest between the models at line 1, Figure 21, 22 and 23 where the lines are positioned in the same order and direction as in Figure 20. The local model and the extruded model that had slip wall BCs fit each other well, however they deviated more from the global model than the extruded model with free stream BCs did.

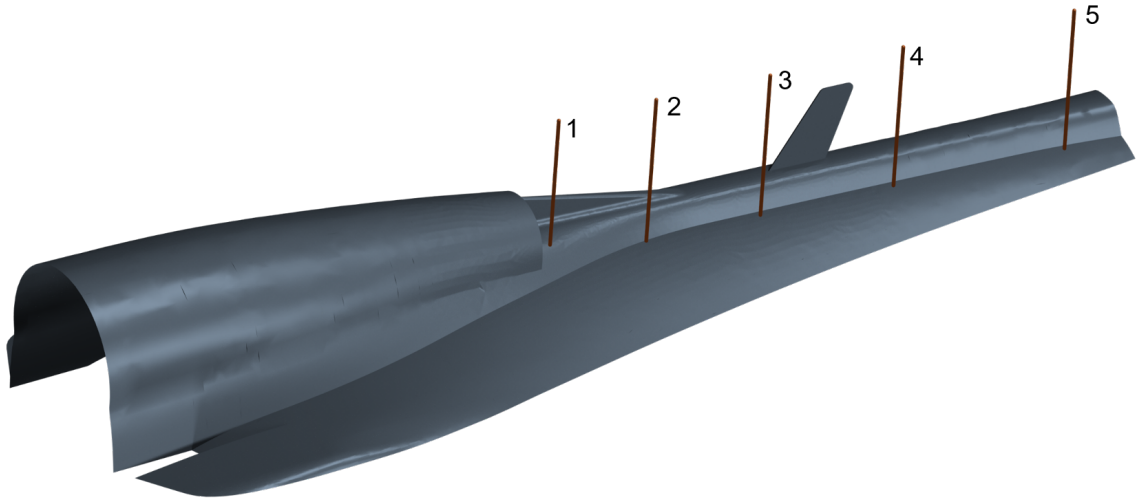

Figure 20: The line probes' positions in relation to the aircraft surface.

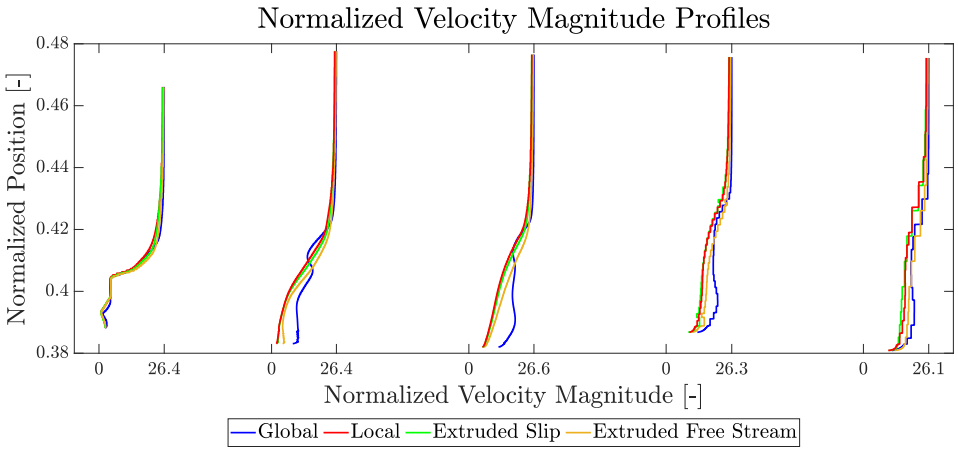

Figure 21: Normalized velocity magnitude profiles at five line probes along the domain. The local and the extruded model with slip wall BC showed a close fit while the extruded model with free stream BC often showed the closest fit to the global model.

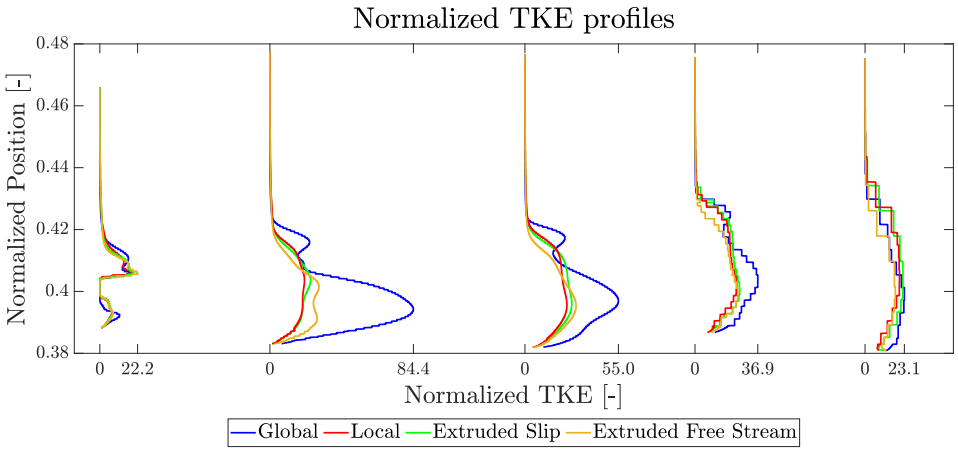

Figure 22: Normalized temperature profiles at five line probes along the domain. The local and the extruded model with slip wall BC showed a close fit while the extruded model with free stream BC often showed the closest fit to the global model.

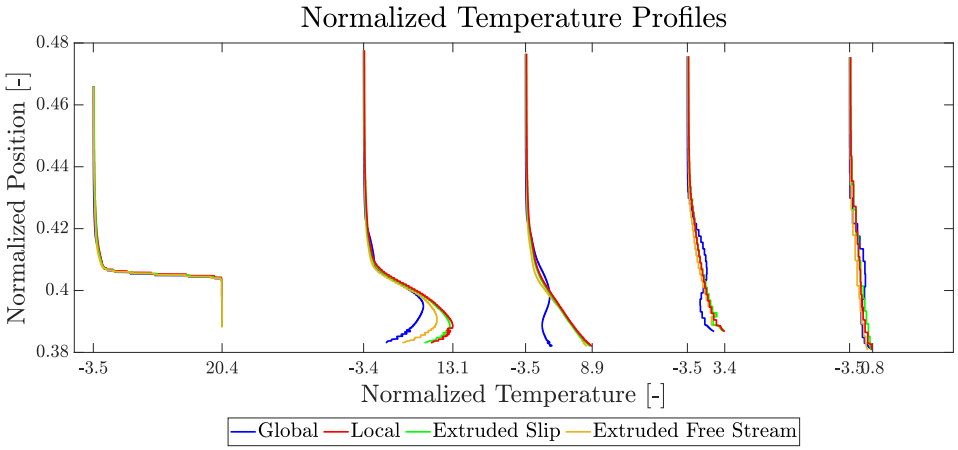

Figure 23: Normalized TKE profiles at five line probes along the domain. The local and the extruded model with slip wall BC showed a close fit while the extruded model with free stream BC often showed the closest fit to the global model.

It was also of interest to investigate how the BCs work by looking into the normalized velocity magnitude at a plane placed with a distance from the aircraft surface, Figure 24 where the inlet of the domain is to the left of the velocity planes in (a) and (b). The position of the plane was chosen to decrease the impact of the fluid flow about the aircraft as much as possible. The results showed that when slip walls were used, the bottom part of the plane had a very low velocity magnitude which was shown to be the effect of the propagation of the decelerated flow at the aircraft surface. The free stream BC instead controls the velocity at the bottom of the plane since that was where the BCs were applied and the velocity magnitude was therefore higher.

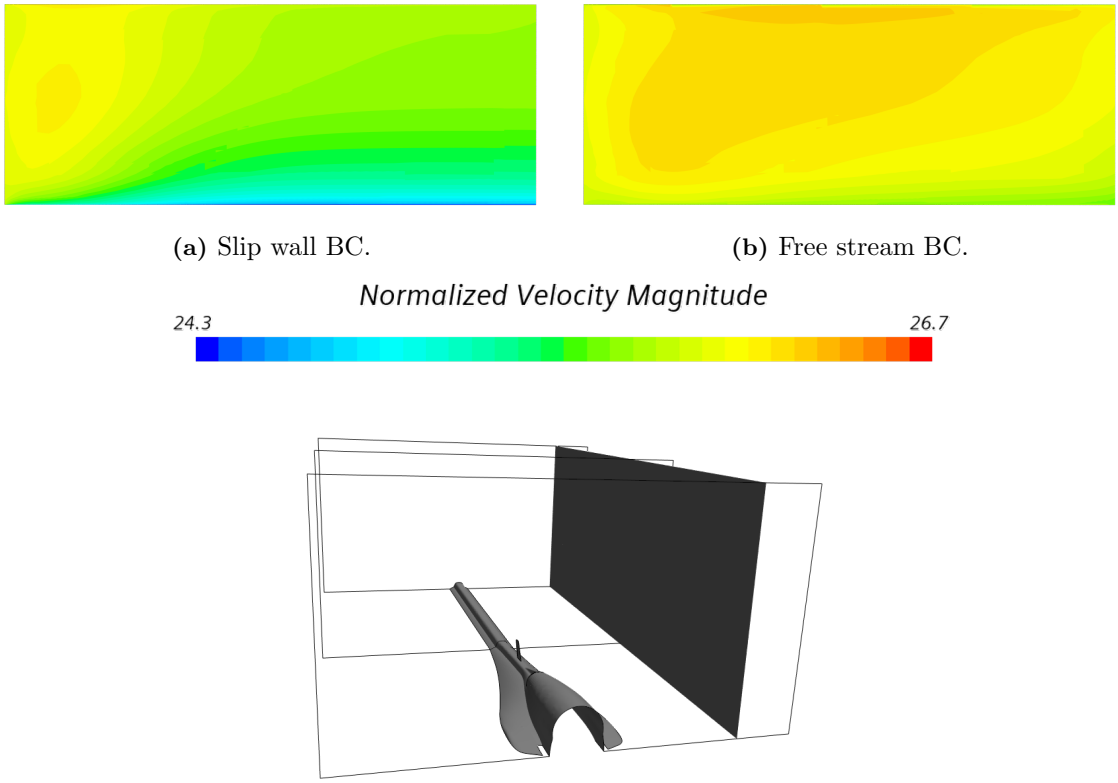

(a) Slip wall BC.

(b) Free stream BC.

(c) Placement of the normalized velocity magnitude plane, black plane to the right of the aircraft geometry, showed in (a) and (b).

Figure 24: The normalized velocity magnitude for slip wall and free stream BC at the sides, top and bottom of the fluid domain, (a) and (b), at the plane in (c). The overall velocity magnitude was larger when using free stream BC.

The *Specified* y^+ *HTC* at 8 monitor points was also measured for the different models, Figure 25. The *Specified* y^+ *HTC* was used because of the possibility to choose at which y^+ value the HTC should be calculated. In comparison, the *Local HTC* that uses the near wall cell in calculations can result in high HTC values in regions with no-slip walls [35]. The *Local HTC* was also not used because the first cell height could differ close to the geometry due to the earlier wrapping. Therefore, the *Specified* y^+ *HTC* was used and calculated at $y^+ = 100$ based on general recommendations [35]. In Table 12 the normalized *Specified* y^+ *HTC* values are presented at monitor 1-8 and their percentual change to the global model is also shown. It was apparent that the monitor points closest to the inlet, point 1-2 and 5-6, for the Local and Extruded model with slip walls resulted in smaller deviations while the monitors further downstream resulted in deviations around 10-20 %. For the Extruded model with free stream BCs, the points that were in the direction of the jettisoned air, monitor 1 to 4, showed small deviations in comparison to the global model while monitor 5 to 8 showed larger deviations. These monitor points were placed further from the jettisoned air and closer to the boundary where the free stream conditions were applied.

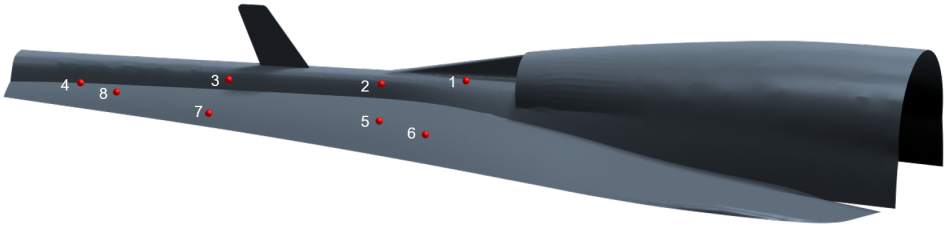

Figure 25: The monitor points used to measure the *Specified y^+ HTC*.

Table 12: HTC at eight monitor points and the change in percentage for each model to the same points measured in the global model. The deviations to the global model were larger in the points further from the jettisoned air.

Domain	**1**	[%]	**2**	[%]	**3**	[%]	**4**	[%]
Global	43.25		15.49		30.12		31.95	
Local	32.89	23.96	16.11	4.02	36.81	22.25	35.17	10.09
Extrude Slip Walls	35.49	17.95	17.00	9.77	37.13	23.31	37.43	17.14
Extrude Free Stream	42.80	1.04	16.96	9.54	32.32	7.34	30.46	4.65
Domain	**5**	[%]	**6**	[%]	**7**	[%]	**8**	[%]
Global	40.18		39.73		40.92		34.52	
Local	40.45	0.69	40.99	3.17	37.43	8.51	38.91	12.72
Extrude Slip Walls	40.59	1.03	41.18	3.67	37.83	7.51	38.61	11.85
Extrude Free Stream	27.49	31.57	31.17	21.55	27.93	31.72	29.28	15.18

The extruded model with slip walls as BC was selected to be used in further simulations for multiple reasons. As described earlier the outlet of the local domain was placed too close to the wake and an extrusion was a reasonable geometric operation to perform. When investigating the *Specified y^+ HTC* together with the results in Figure 21-23, it was apparent that the free stream BC resulted in a flow behaviour similar to the global model at the jettisoned air stream while having large deviations closer to the free stream. The overall flow behaviour when using slip walls as BCs was therefore assumed more representative for this specific domain.

3.3.3 y^+ Investigation

With higher y^+ values, fewer prism layers could be used which would reduce the computational cost. It was therefore of interest to investigate the impact of the y^+ value when using the STAR-CCM+ specific wall treatment, *All y^+ wall treatment*, when the y^+ value was either mostly below two or in the buffer or log-law layer. The investigation was performed on the local model. The y^+ range was modified by changing the number of prism layers and their stretch rate in Mesh 2, which was used as the baseline mesh of the investigation. The setups used are presented in Table 13, where the number of prism layers used were greater than the minimum of general recommendations [36].

Table 13: The number of prism layers and their total thickness, as well as the stretching rate, used in the y^+ investigation.

First cell height position	Number of prism layers	Stretching rate	Total thickness [mm]
Viscous	30	1.2	0.0153
Buffer	22	1.1	0.0154
Log-Law	17	1.1	0.0154

The *All* y^+ *wall treatment* changes between the *Low* and *High* y^+ *wall treatments* depending on the local y^+ value. The wall treatment uses a function, that is dependent on the Reynolds number based on the wall distance, that blends the turbulent quantities. The *Low* y^+ and *High* y^+, are used to model different parts of the boundary layer. The *Low* y^+ *wall treatment* requires $y^+ < 1$, but a higher y^+ is acceptable as long as the first cell node is placed within the viscous sub-layer [34]. The *High* y^+ *wall treatment* models the solution in the BL and it can be used when the mesh has a $y^+ > 30$. The *All* y^+ *wall treatment* is also said to be capable of producing reasonable results for a y^+ value in the buffer layer, it is however not recommended since a higher accuracy can be obtained if y^+ is within any of the other two regions. Using the *All* y^+ *wall treatment* resolves the BL where $y^+ < 1$ since no wall laws are used, while wall functions are implemented in to the modelling where $y^+ > 1$.

3.3.4 Transient Simulations

Transient simulations were performed to investigate the impact of the CFL number. At first, little turbulence was identified from the simulations because of the low angle of attack in combination with the low mass flow jettisoned, which was coherent with earlier experience at SAAB AB. To capture a larger rate of the turbulence and obtain a more qualitative comparison, the mass flow was increased with 66 % which meant that the jettisoned air had a higher velocity than the free stream. Even with the increased mass flow, and in turn velocity, the overall y^+ value was below two and therefore no alterations to the mesh were done.

The same solver setup as used in the steady simulations, Table 8, was used but the time setting was changed to *Implicit Unsteady*. The CFL numbers 1, 10, 20, 50 and 100 were investigated and in all cases 10 inner iterations were run. The CFL number was conservatively calculated using the maximum velocity in the entire domain and the smallest element found in the mesh outside of the prism layers. All simulations were run from the same initialisation for 20 flow through's, where data was sampled during the last 10.

The turbulence model RKE Two-layer was also used in simulations to compare it towards SST $k-\omega$. It was run with a CFL of 1 and 10 to see if any difference in impact of CFL was found for the RKE Two-layer model compared to the SST $k-\omega$ model.

4 Results

The results from the experimental tests and solid simulations are presented in *section 4.1* while the results from the investigations performed on the fluid simulation model is presented in *section 4.2*.

4.1 Solid Results

4.1.1 Stationary results

Combinations of HTC and TCR were varied and compared to experimental data to find the most correct values. The results were compared by taking the absolute values of the maximum, minimum and average percentual temperature difference compared to the experimental data for the 20 measured points, Figure 26 (a), (b) and (c). The lowest average difference was found for TCR $= 5 \cdot 10^{-4}$ m^2K/W and HTC $= 8.34$ W/m^2K and was 6.6 %, Figure 26 (c). It can also be seen that most of the lowest average differences occurred for TCR values between $1 \cdot 10^{-4}$ and $1 \cdot 10^{-3}$ m^2K/W. A similar trend could be seen for the minimum difference, Figure 26 (b), where most of the lowest differences were seen in this region. It was clear that an increase of TCR above $1 \cdot 10^{-3}$ m^2K/W significantly increased the difference to experimental data both for the maximum difference and the average difference.

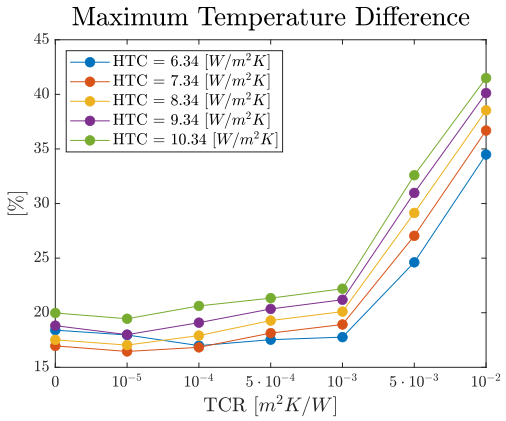

(a) Maximum absolute temperature difference.

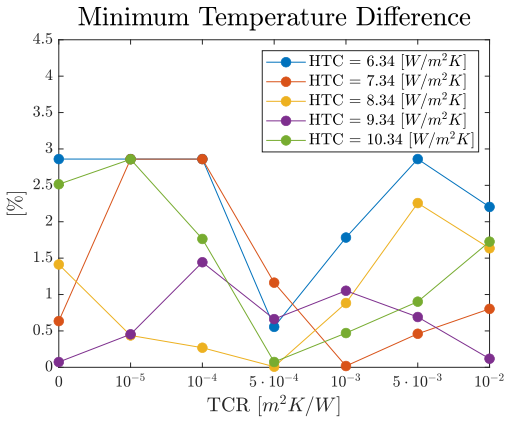

(b) Minimum absolute temperature difference.

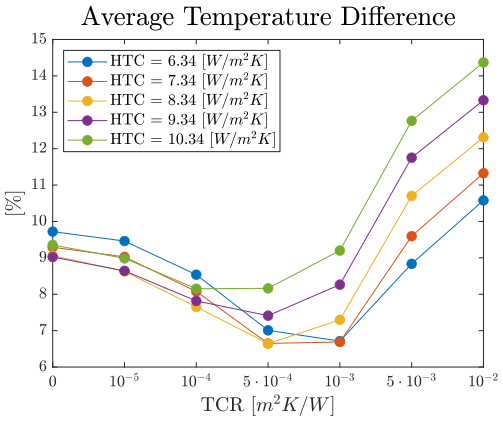

(c) Average absolute temperature difference.

Figure 26: The absolute minimum, (a), maximum, (b), and average, (c), temperature differences compared to experimental data of the 20 measured points for different values of HTC and TCR. The lowest differences can be seen for HTC values between 7.34 and 8.34 and TCR values between $1 \cdot 10^{-4}$ and $1 \cdot 10^{-3}$. Note that the figures have different y-axes.

The value of TCR was also compared to values from a previous study of TCR at SAAB AB [22]. It is worth noting that a climate chamber was used in the mentioned study where most of the tests had a surrounding temperature of 10 $°C$. The study had investigated TCR values for aluminium with and without a primer heated to 20 and 80 $°C$. In comparison, the experimental test piece in this thesis consisted of mostly aluminium parts with a primer applied to them. The chosen TCR value agreed better with the TCR value of aluminium with a primer, than without [22]. It also agreed better for the aluminium heated to 20 $°C$ than the aluminium that was heated to 80 $°C$. The study also investigated aluminium with and without a primer heated to 35 $°C$ when the ambient air was heated or cooled to certain temperatures. The best agreement between the results in this thesis and all the results in the study was seen for one of these tests where the ambient temperature was set to 20 $°C$. Generally, the value of TCR in this thesis differed significantly to those in the study, with differences ranging from 50-90 %.

The difference between a case with and without radiation was also investigated. The results showed that including radiation in the simulations on average gave a 4.6 % decrease in temperature for the measured points, with two points reaching a maximum difference of 9-10 %. It also gave an increased computational time of 40 % for each iteration and 370 % for the total CPU and physical time.

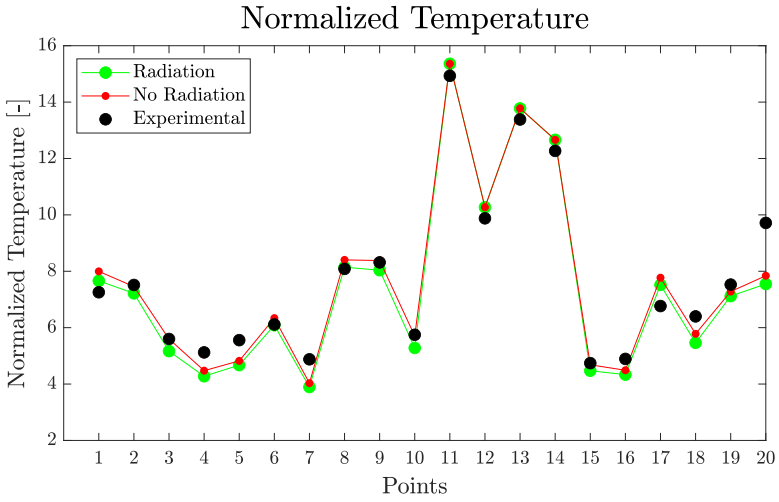

Figure 27: Normalized temperature for simulations with and without radiation as well as experimental data presented for each measuring point. The simulations with and without radiation fit each other well and the resulting average change was at 4.6 %.

4.1.2 Transient results

The simulated and experimental results for TCR $5 \cdot 10^{-4}$ m^2K/W at point 8, 14, 17 and 20 are shown in Figure 28 while the remaining points are presented in *Appendix B*. It was clear for point 17 that the simulated temperature increased faster than the experimental, Figure 28. All points showed a similar trend while also underpredicting the temperature compared to the experimental data as seen in for example point 20. This leads to the simulated values being relatively close to the experimental at the time steps in the beginning but larger deviations are seen closer to the end of the simulation. All points except 12, 14 and 17 showed this underprediction, point 12 was placed directly below the resistor. Point 14 was placed so far from the resistor that its temperature was mostly unchanged throughout the experiment and simulation. Point 7 and 20, which were placed on the same thin skin plate but with different distances to the resistor, showed similar behaviour for a TCR value of $5 \cdot 10^{-4}$ m^2K/W.

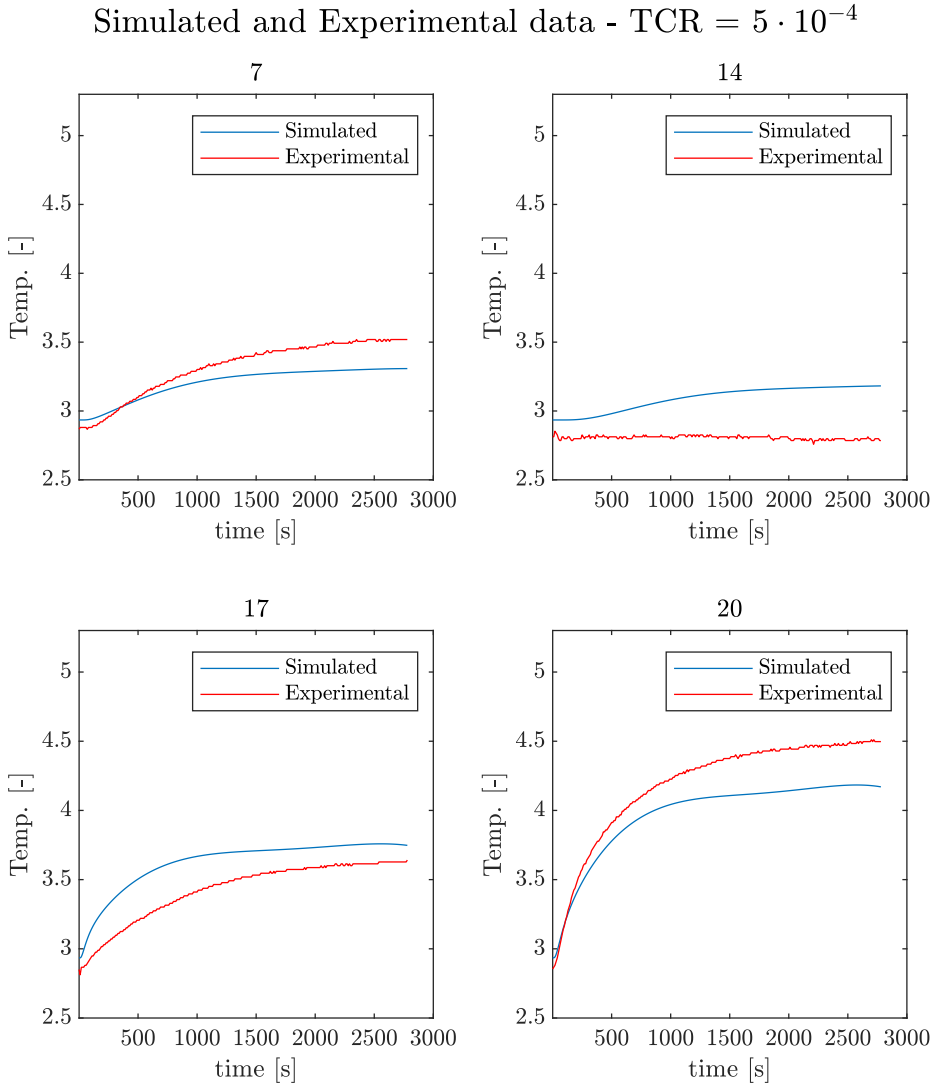

Figure 28: Normalized simulated and experimental temperatures in points 7, 14, 17 and 20 for a TCR value of $5 \cdot 10^{-4}$ m^2K/W. Most of the points showed similar results as for point 20. Generally, the simulated data underpredicted the temperatures compared to the experimental data.

Since the transient simulation with a TCR of $5 \cdot 10^{-4}$ m^2K/W underpredicted the temperature in most points, a transient simulation with a TCR value of $1 \cdot 10^{-4}$ m^2K/W was also performed. The results for all points for this simulation can be found in *Appendix B*. They showed an increase in the predicted temperature which in turn increased the coincidence with experimental data for most measuring points, similarly to point 20 in Figure 29.

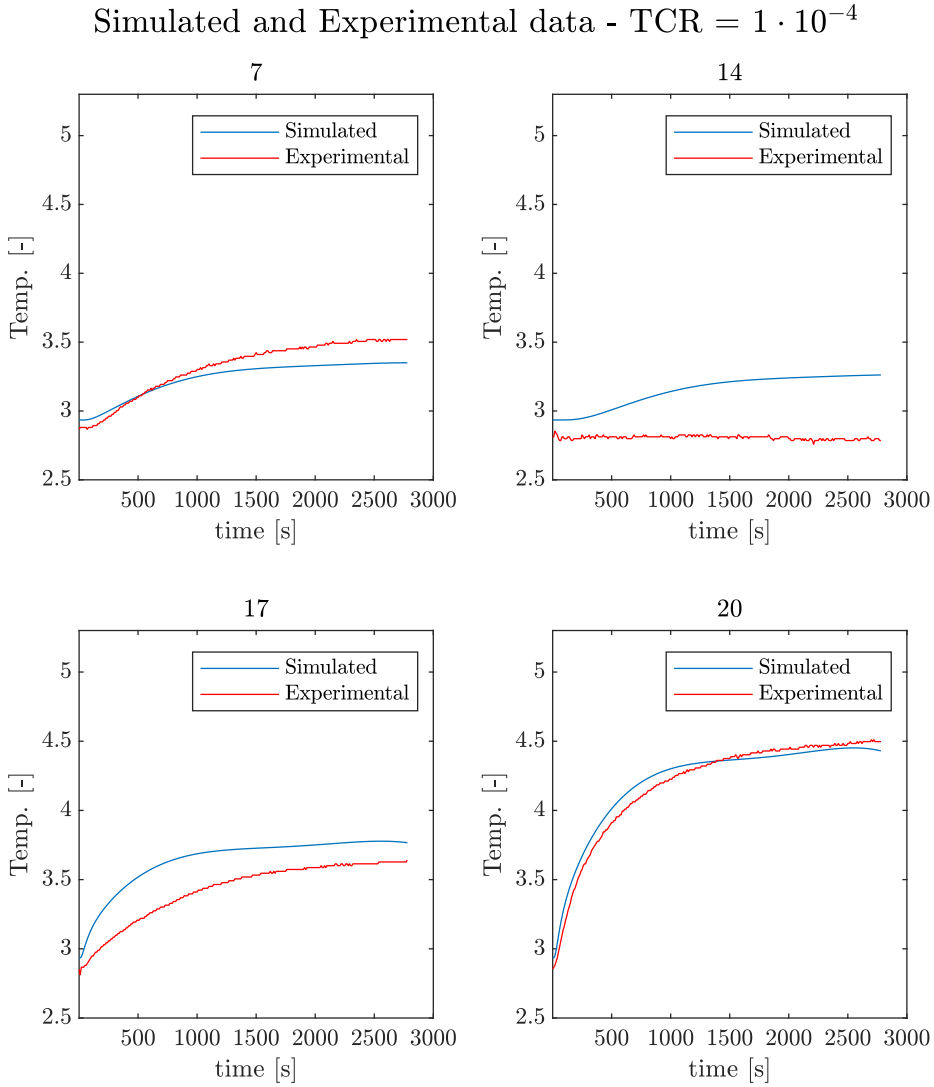

Figure 29: Normalized simulated and experimental temperatures in points 7, 14, 17 and 20 for a TCR value of $1 \cdot 10^{-4}$ m^2K/W. The simulated data generally show better coherence with experimental data compared to the previous transient simulation.

The average and maximum differences of the last 20 seconds for all points between the experimental and simulated data are also presented, Table 14. It can be seen that the average differences are lower for all transient simulations compared to the stationary, *section 4.1.1.* It is also clear that a TCR of $1 \cdot 10^{-4}$ m^2K/W showed the best coherence with the experimental results in the transient simulations. It was also seen that the maximum difference in the transient simulations occurred for point 14 which was mostly unaffected by the applied heat. If point 14 was excluded, the maximum difference for both TCR values were approximately 7 %.

Table 14: The absolute average and maximum percentual difference between simulated and experimental data taken from the 20 measured points for the transient simulations with different TCR values. The average was smallest for a TCR at $1 \cdot 10^{-4}$ while the maximum was smallest for a TCR at $5 \cdot 10^{-4}$.

TCR	$1 \cdot 10^{-4}$ [%]	$5 \cdot 10^{-4}$ [%]
Average	3.4	4.6
Maximum	16.6	13.8

4.2 Fluid Results

4.2.1 y^+ Investigation

To compare the three different setups the normalized temperatures and velocities were obtained in the same measuring points as in the mesh analysis, Table 15. It is also presented in which sub-layer of the BL the first cell was located. The results show similar behavior as in the mesh analysis, the sensitivity to change was larger for the monitors at the jettisoned air than at the engine exhaust. However, no other clear pattern could be identified.

Table 15: Normalized temperatures and velocities measured at seven monitors when performing the y^+ investigation. Minimal differences were shown.

Mesh	**Layer**	T_1	T_2	T_3	T_4	T_5	T_6	T_7
71 M	Log-Law	20.31	20.34	11.40	6.95	68.04	67.59	60.11
81 M	Buffer	20.31	20.34	11.20	6.73	68.04	67.61	60.13
98 M	Viscous	20.31	20.35	11.27	6.89	68.04	67.61	60.68
Mesh	**Layer**	v_1	v_2	v_3	v_4	v_5	v_6	v_7
71 M	Log-Law	4.52	2.77	2.90	8.52	105.33	105.88	104.74
81 M	Buffer	4.53	3.01	2.66	8.64	105.30	105.86	104.76
98 M	Viscous	4.39	2.26	2.94	8.70	105.30	105.86	105.65

Since no clear behaviour could be found the normalized temperature and velocity were also investigated within the BL and over the wing. It was done by using line probes with evenly distributed measuring points. The line probe within the BL was in the surface normal direction and the line probe over one of the wings was oriented in the direction of the flow, due to the curvature of the wing the measuring points had varying distances to the wing surface. The results showed deviations within the BL for the temperatures and velocities where the first cell centre was in the viscous sub-layer, in comparison when positioned in the buffer and log-law sub-layer, Figure 30 (a) and 31 (a). The normalized values over the wing display the same behaviour independent of y^+ range, Figure 30 (b) and 31 (b). It was shown that the temperature decreases with a decreased y^+ and the velocity increases with a decrease in y^+. The differences are however small and all curves follow the same trend.

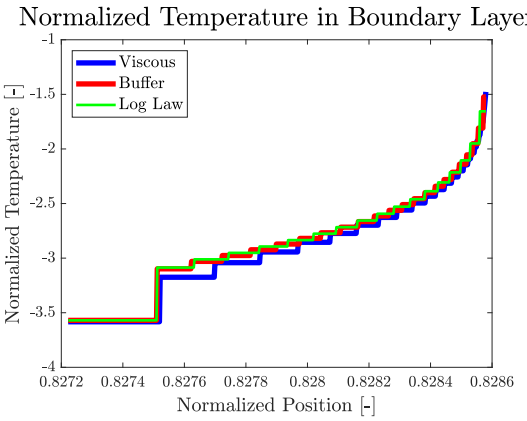

(a) Normalized temperature within the BL.

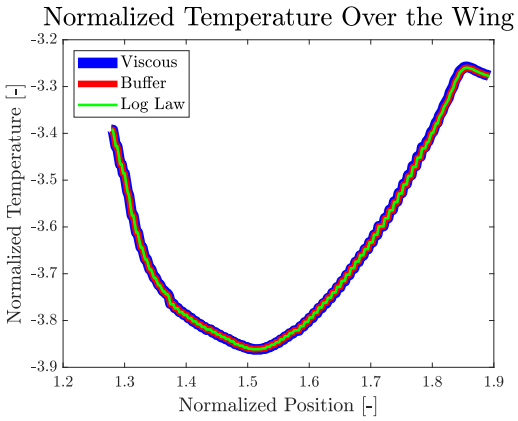

(b) Normalized temperature over the wing.

Figure 30: Normalized temperature within the boundary layer and over the wing when investigating the impact of y^+. The temperature in the viscous sub-layer in (a) deviates to the buffer and log-law sub-layer, which fit well together. No major differences can be seen in (b). A lower value in the x-axis in (a) corresponds to an increased distance from the aircraft surface.

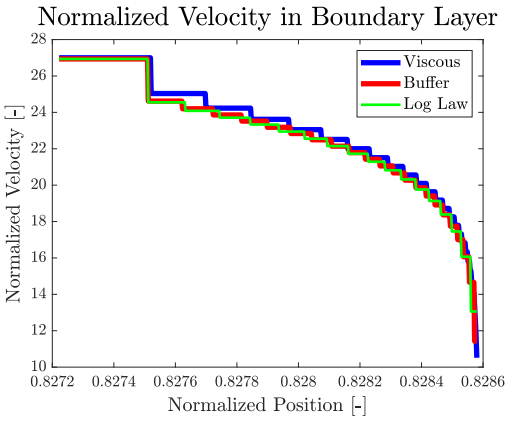

(a) Normalized velocity within the BL.

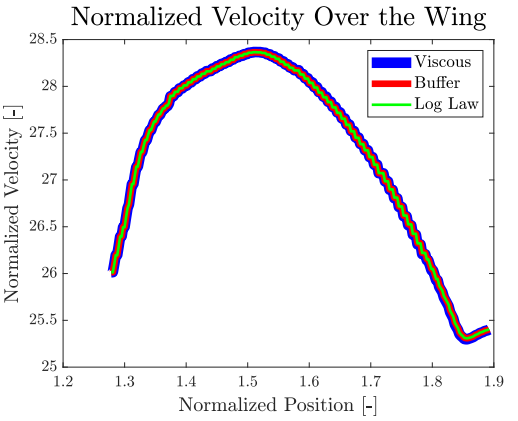

(b) Normalized velocity over the wing.

Figure 31: Normalized velocity within the boundary layer and over the wing when investigating the impact of y^+. The velocity in the viscous sub-layer deviates to the buffer and log-law sub-layer, which fit well together. No major differences can be seen in (b). A lower value in the x-axis in (a) corresponds to an increased distance from the aircraft surface.

4.2.2 Numerical Technique

To investigate the difference between RANS and URANS for the considered domain the *Specified* y^+ *HTC*, velocity and temperature for the time averaged URANS values were compared towards RANS values. The results showed that RANS, overall, predicted lower values than URANS for the *Specified* y^+ *HTC* and velocity, while predicting higher temperature as well as showing larger dissipation closer to the outlet, Figure 32-34 where the view is from above the aircraft.

The maximum, minimum and average *Specified* y^+ *HTC*, velocity and temperature differences at the monitor points used, Figure 12 and 25, were obtained to quantify the

differences between the numerical techniques. The *Specified* y^+ *HTC* resulted in largest differences, Table 16. The resulting differences were an apparent result of the monitor points 5-8, which were placed further from the jettisoned air, being greatly affected by chosen numerical technique with differences between 13-24 %. Generally, smaller differences were found for the temperature, Table 16, which was coherent with the results being found in *section 3.3.1*, where the temperatures were less impacted by mesh differences than the velocity.

Table 16: Percentual differences between URANS and RANS. The differences were largest for the *Specified* y^+ *HTC* and generally smallest for the temperature.

	Maximum [%]	**Minimum** [%]	**Average** [%]
Specified y^+ HTC	23.25	1.96	11.96
Velocity	9.09	1.27	5.13
Temperature	12.26	0.63	4.17

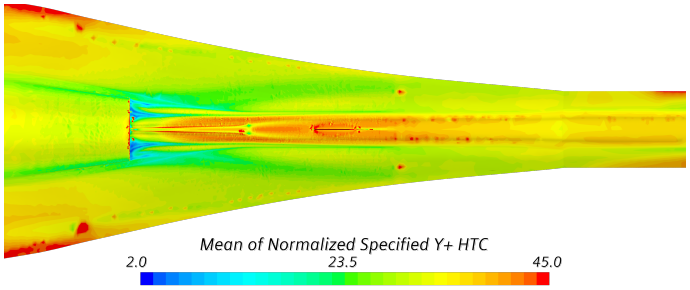

(a) URANS.

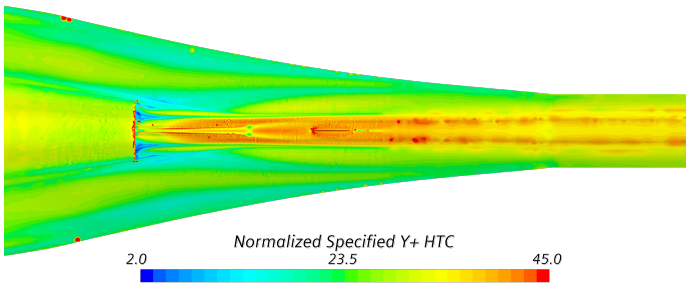

(b) RANS.

Figure 32: Time averaged normalized *Specified* y^+ *HTC* obtained from a URANS simulation and normalized *Specified* y^+ *HTC* obtained from a RANS simulation, Figure (a) and (b) respectively. Overall, the RANS simulation underpredicted compared to URANS.

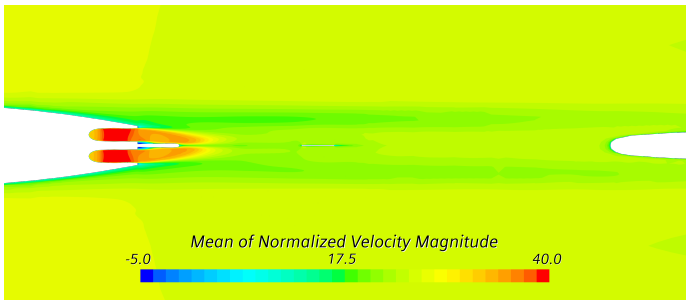

(a) URANS.

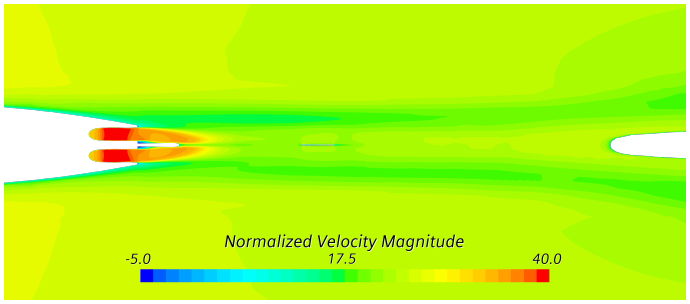

(b) RANS.

Figure 33: Time averaged normalized velocity obtained from a URANS simulation and normalized velocity obtained from a RANS simulation, Figure (a) and (b) respectively. Overall, the RANS simulation underpredicted compared to URANS.

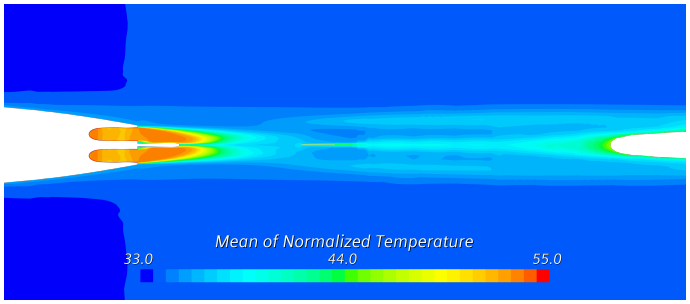

(a) URANS.

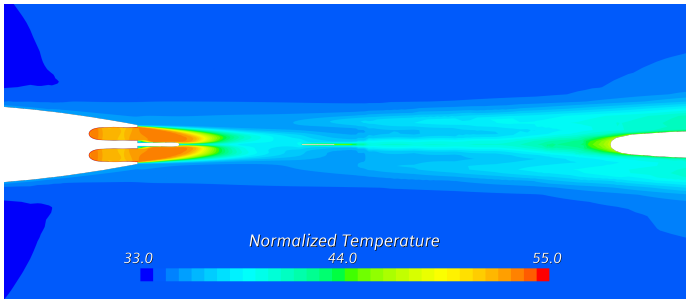

(b) RANS.

Figure 34: Time averaged normalized temperature obtained from a URANS simulation and normalized temperature obtained from a RANS simulation, Figure (a) and (b) respectively. Overall, the RANS simulation overpredicted compared to URANS.

4.2.3 CFL Investigation

To investigate the CFL number's impact on the accuracy the time averaged normalized pressure, temperature and velocity were measured at the monitor points at the jettisoned air that were used in earlier investigations, Figure 12. The normalized *Specified* y^+ *HTC* was obtained at the 8 monitor points used when investigating BC for the local domain, Figure 25. The CFL numbers 1, 10, 20, 50 and 100 were used in the simulations. In Figure 35-38 the normalized *Specified* y^+ *HTC*, pressure, temperature and velocity are presented at each point for all CFL numbers investigated. Overall, CFL 1 and 10 fit well together while the deviations increased with an increase in CFL. It was also shown that a larger CFL tends to underpredict the maximum values while overpredicting the minimum values in comparison to CFL 1.

The results showed that the CFL number had its largest impact on the *Specified* y^+ *HTC* values at the jettisoned air while at the monitors further from it, little differences were shown, Figure 35. It was also shown that CFL 1 and 10 often showed a good fit, except for at point 4. Minimal differences were shown between CFL 50 and 100, which were the CFL values that showed the largest deviations to CFL 1.

The largest deviations in pressure between the different CFL numbers were found at point 1 and 3, where monitor 1 was closest to the outlet of the jettisoned air and monitor 3 was positioned further downstream, Figure 36. The time averaged normalized temperature showed almost no deviations, Figure 37. The largest differences were found at point 4. The time averaged normalized velocity also showed small differences but larger deviations were found at point 1 and 3, Figure 38.

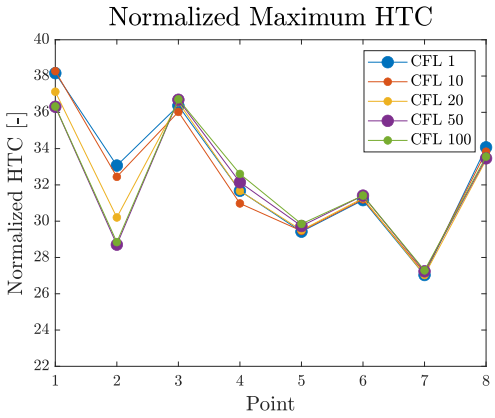

(a) Normalized maximum *Specified* y^+ *HTC*.

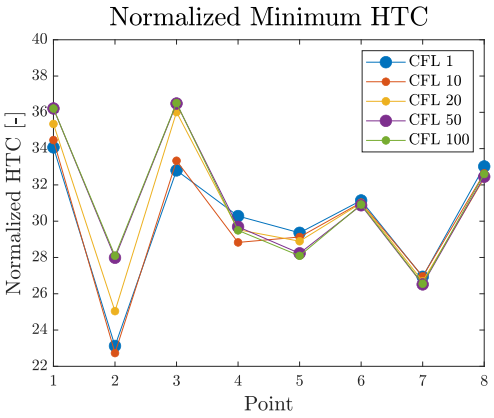

(b) Normalized minimum *Specified* y^+ *HTC*.

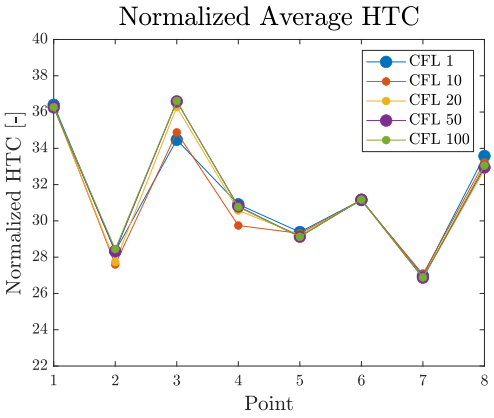

(c) Normalized mean *Specified* y^+ *HTC*.

Figure 35: Time averaged normalized maximum, minimum and average *Specified* y^+ *HTC* over 10 flow throughs. CFL 10 showed good coherence with CFL 1 while the larger CFL numbers often deviated.

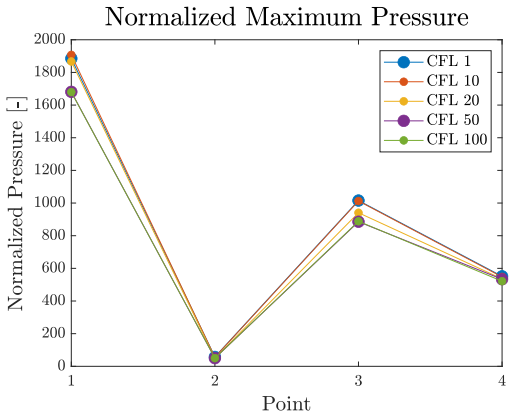

(a) Normalized maximum pressure.

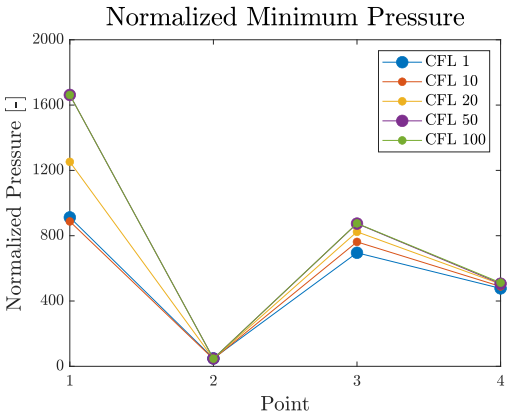

(b) Normalized minimum pressure.

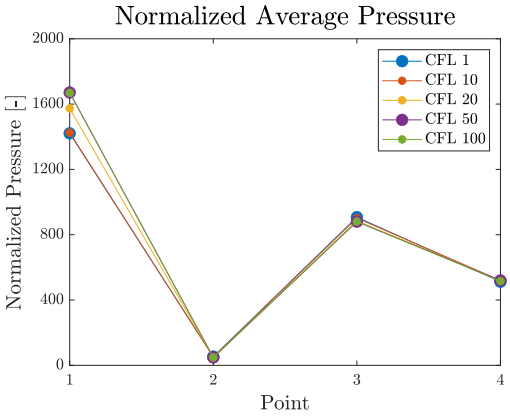

(c) Normalized mean pressure.

Figure 36: Time averaged normalized maximum, minimum and mean pressure over 10 flow throughs. CFL 10 showed good coherence with CFL 1 while the larger CFL numbers often deviated.

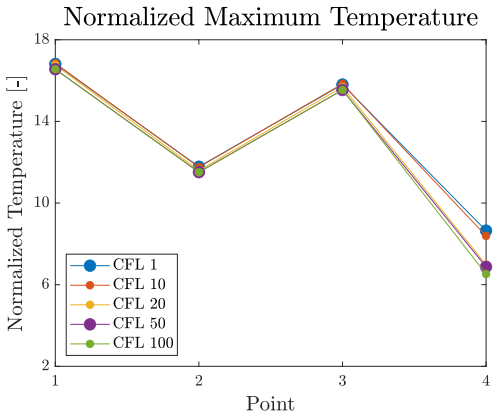

(a) Normalized maximum temperature.

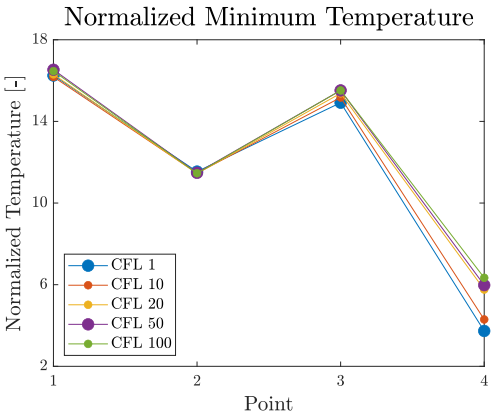

(b) Normalized minimum temperature.

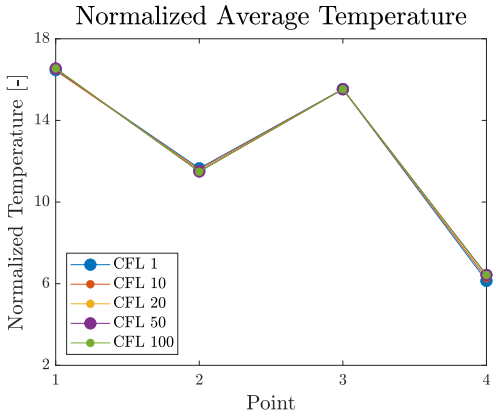

(c) Normalized mean temperature.

Figure 37: Time averaged normalized maximum, minimum and mean temperature over 10 flow throughs. CFL 10 showed good coherence with CFL 1 while the larger CFL numbers often deviated.

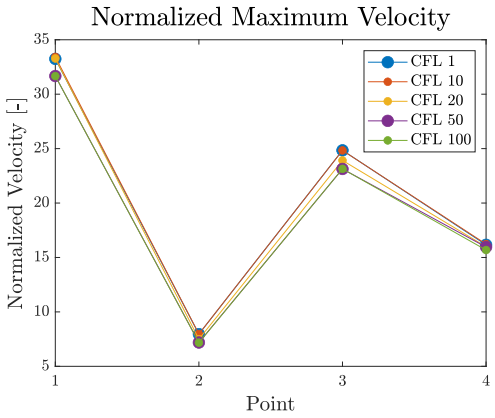

(a) Normalized maximum velocity.

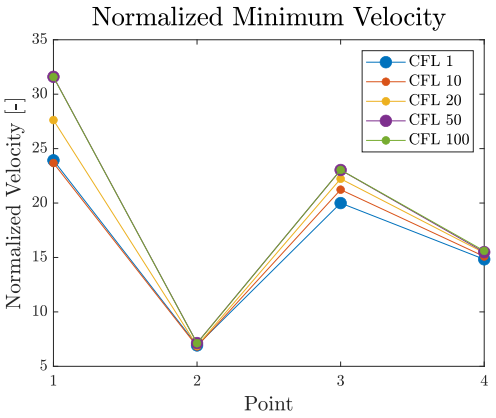

(b) Normalized minimum velocity.

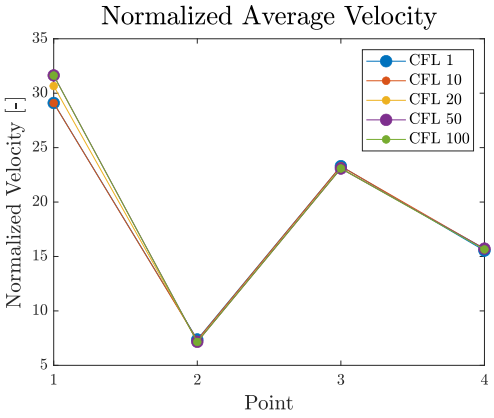

(c) Normalized mean velocity.

Figure 38: Time averaged normalized maximum, minimum and mean velocity over 10 flow throughs. CFL 10 showed good coherence with CFL 1 while the larger CFL numbers often deviated.

Investigating the time averaged *Specified* y^+ *HTC*, velocity and temperature qualitatively in a plane showed almost no visible differences between the CFL numbers, Figure 32a, 33a and 34a which shows the qualitative results for CFL 1 only. This corresponded well to the similarities found in Figure 35-38. However, the instantaneous values showed large differences between the smaller and larger CFL numbers. The results showed that the turbulence was captured to a much larger extent for CFL 1 than for CFL 100, Figure 39 where the normalized instantaneous temperature for each CFL number at the same plane is presented.

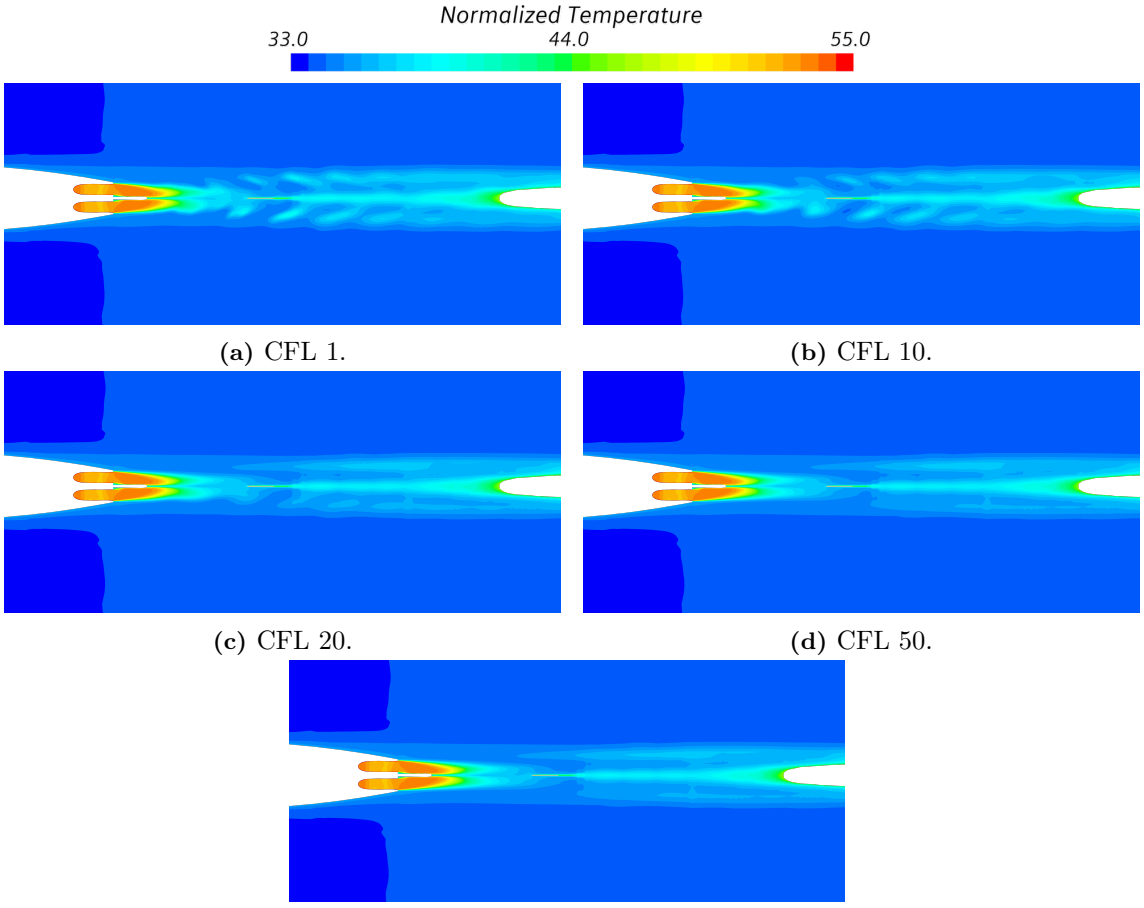

(a) CFL 1.

(b) CFL 10.

(c) CFL 20.

(d) CFL 50.

(e) CFL 100.

Figure 39: Instantaneous normalized temperature for CFL numbers of 1, 10, 20, 50 and 100. The captured turbulence can be seen to decrease with an increase in CFL.

Since little differences were shown in the graphs and larger differences were seen for the instantaneous values it was of interest to see at which magnitudes of the CFL number was present in the domain. In Figure 40 the Convective Courant Number in the area close to the area of interest is shown, note that different scales on the legends are present. The scalar visualizations in combination with Figure 39 showed that when a limited area had CFL numbers below 10, most of the flow was captured while the downstream flow was shown to be greatly affected when the CFL number was larger than 10 in the same area.

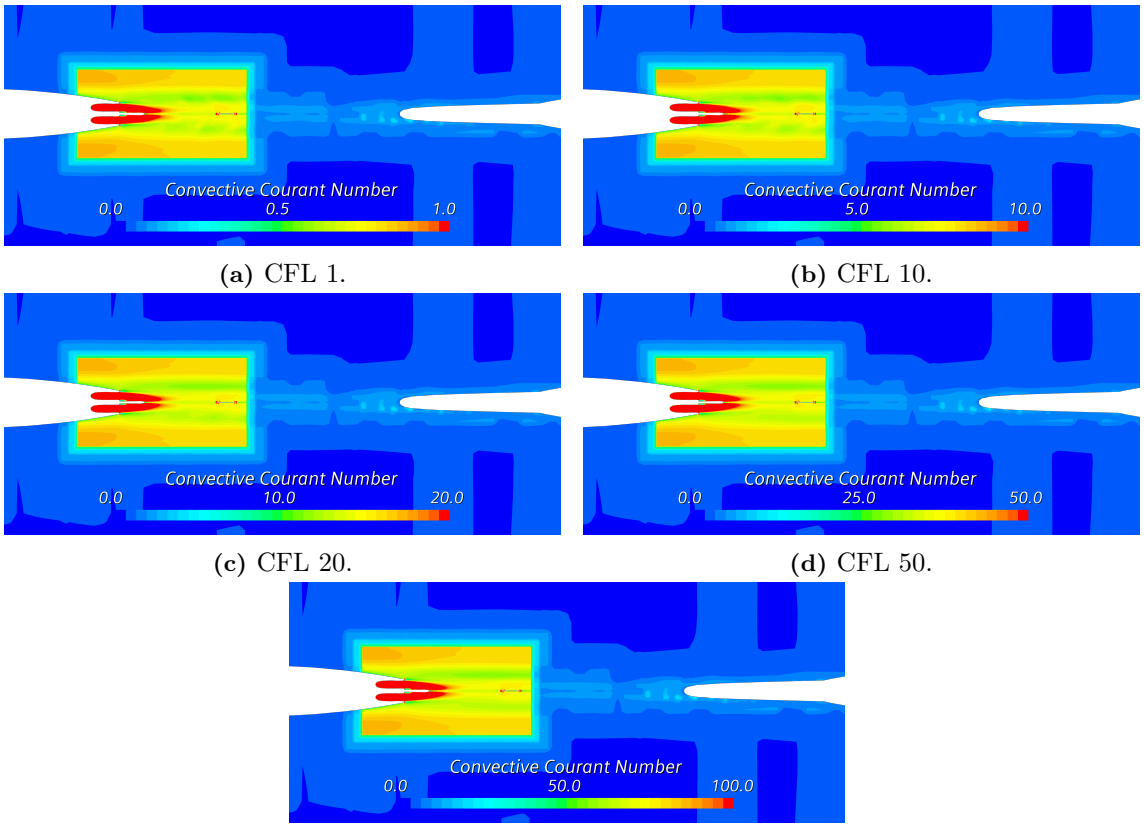

(a) CFL 1.

(b) CFL 10.

(c) CFL 20.

(d) CFL 50.

(e) CFL 100.

Figure 40: The Convective Courant Number in a part of the domain, note that the legends have different scales.

It was also investigated if the same results were found when performing transient simulations with the use of RKE Two-layer as chosen turbulence model, where a CFL of 1 and 10 was used. The results for the RKE Two-layer CFL investigation were in principal the same as for the SST $k-\omega$, little or no deviation was found between CFL 1 and 10 independent of variable at the monitor points. During the simulations it was also shown that all turbulence was damped by the RKE Two-layer model while periodic oscillations were found when using the SST $k-\omega$ model.

4.2.4 Turbulence Models

The turbulence models SST $k-\omega$ and RKE Two-layer were run with a CFL of 1 and compared towards each other. The results showed that the SST $k-\omega$ overall gave higher values, Figure 41 where the normalized mean *Specified* y^+ *HTC*, pressure, temperature and velocity are shown at the same monitor points as used in *section 4.2.3*. Similar behaviour was found in Figure 42-44, however for the temperature the RKE Two-layer resulted in higher values. It was also shown that the RKE Two-layer model resulted in more dissipative behaviour.

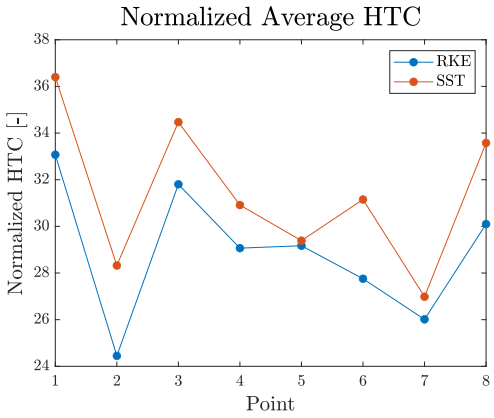

(a) Normalized mean Specified y^+ HTC.

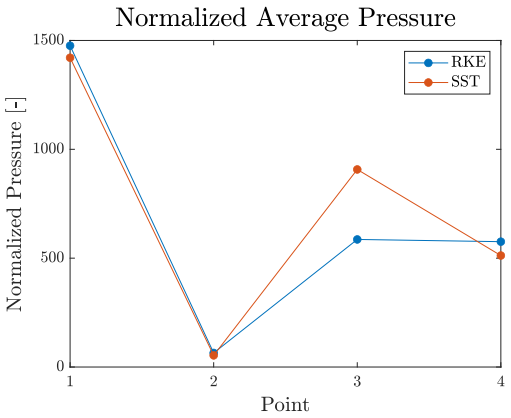

(b) Normalized mean pressure.

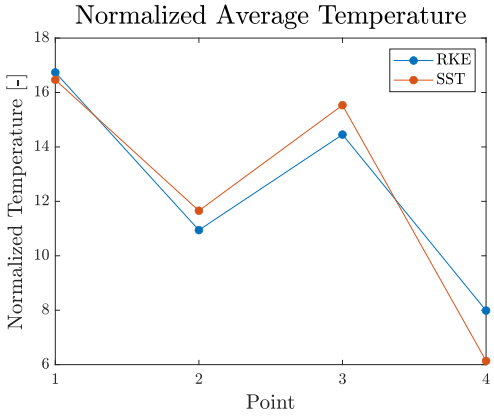

(c) Normalized mean temperature.

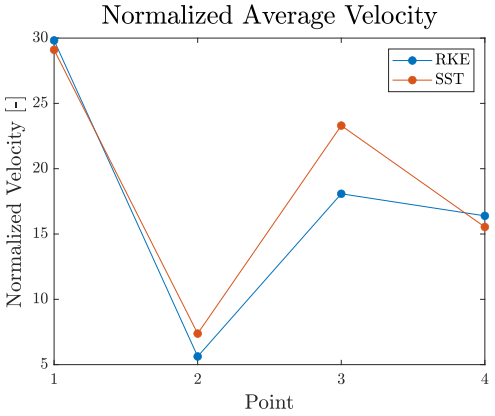

(d) Normalized mean velocity.

Figure 41: Time averaged normalized mean Specified y^+ HTC, pressure, temperature and velocity for SST $k-\omega$ and RKE Two-layer. The RKE Two-layer underpredicted the *Specified* y^+ *HTC* compared to the SST $k-\omega$ while for the other variables, no clear pattern was shown.

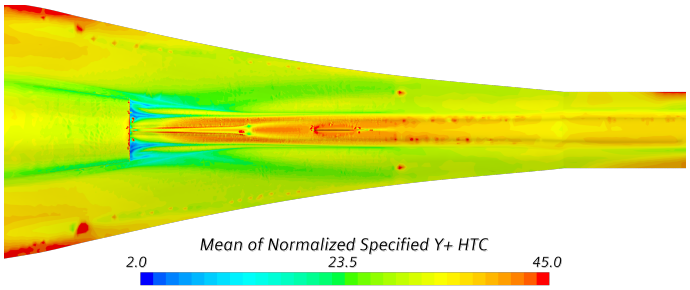

(a) SST $k - \omega$.

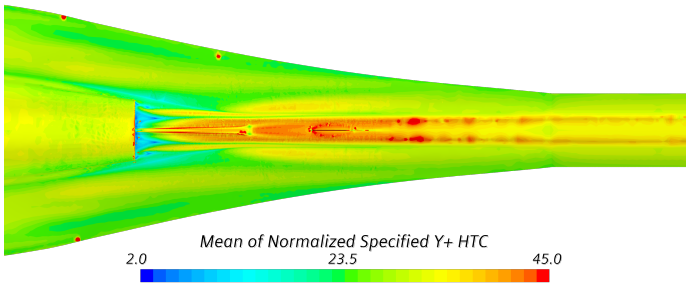

(b) RKE Two-layer.

Figure 42: Time averaged normalized *Specified* y^+ *HTC* obtained from transient simulations for SST $k - \omega$ and RKE Two-layer, Figure (a) and (b) respectively. Overall, the RKE Two-layer underpredicted compared to the SST $k - \omega$.

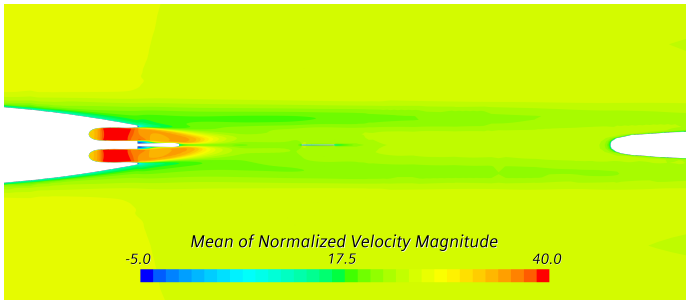

(a) SST $k - \omega$.

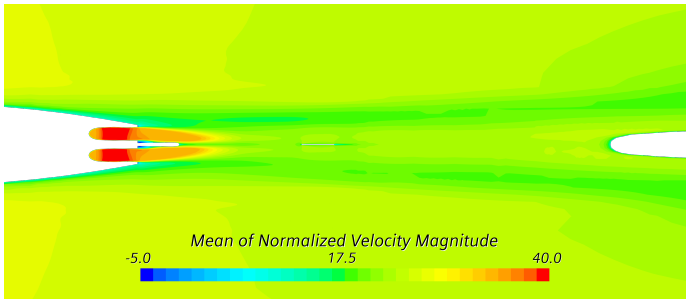

(b) RKE Two-layer.

Figure 43: Time averaged normalized velocity magnitude obtained from transient simulations for SST $k - \omega$ and RKE Two-layer, Figure (a) and (b) respectively. Overall, the RKE Two-layer underpredicted compared to the SST $k - \omega$. The RKE Two-layer also showed a more dissipative behaviour.

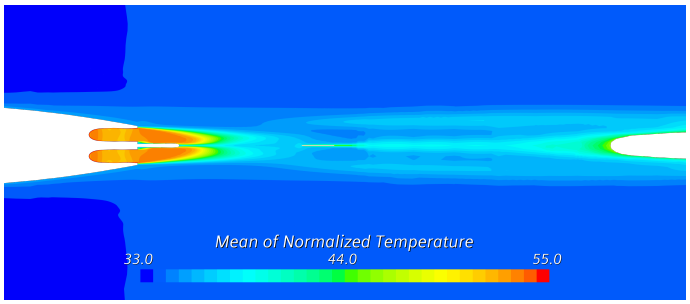

(a) SST $k-\omega$.

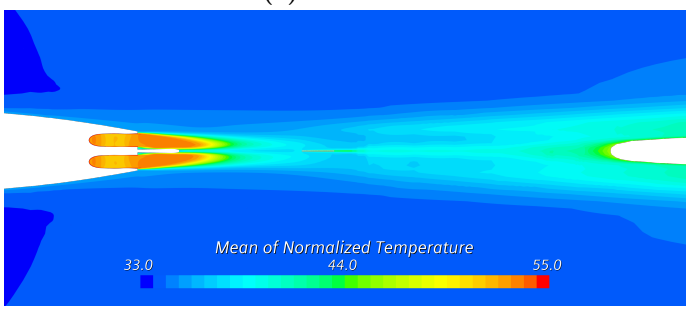

(b) RKE Two-layer.

Figure 44: Time averaged normalized temperature obtained from transient simulations for SST $k-\omega$ and RKE Two-layer, Figure (a) and (b) respectively. Overall, the RKE Two-layer overpredicted compared to the SST $k-\omega$. The RKE Two-layer also showed a more dissipative behaviour.

5 Discussion

In this section the discussion regarding the method used in this thesis as well as the results obtained for the solid and fluid parts are presented, *section 5.1* and *5.2*.

5.1 Experiments and Solid Model

5.1.1 Verification

The mesh analysis for the solid model was performed using constant temperatures in two parts of the geometry as the heat adding BC. This was not the case for the validation experiments nor was it representative for how heat is applied on the structure of a fighter aircraft during flight. Despite this, the heat flux that needed to be captured was representative of the later simulations. The heated parts were placed close to the skin of the aircraft, Figure 7, which meant that it was close to where the BC:s later were applied. The two selected parts spanned over a greater surface than the BC:s used in the validation study, this meant that temperature gradients would be present in more parts of the structure. Based on this, a greater region of the mesh was evaluated in terms of how well a certain mesh resolution could capture the larger gradients, which was an advantage.

The results of the mesh analysis showed that there were no large temperature differences between the different mesh resolutions. This is reasonable since the only mode of heat transfer simulated within the mesh was conduction, which is a linear phenomenon [37] and the mesh resolution will therefore not have a great effect on the results. Similarly, the number of thin layers in the thin structures did not affect the results significantly as long as at least two layers in the thickness direction were present. As seen from the normalized temperatures in the skin, Figure 9 (b), the mesh without thin layers deviated more from the other meshes in areas where the mesh size was coarser. In areas with finer mesh resolution however, it coincided well with the other meshes. The reason for this was that the small elements in the finer regions resulted in more than one element being present in the thickness direction of the structure. However, these elements would not have nodes aligned with the thickness direction, as the thin layers did. This indicates that it was not necessary to use thin layers, which would be aligned with the thickness direction of the structure, to capture the heat distribution as long as more than one element was present across a structure. The reason for this might be that information is lost when using the finite volume method since only one cell is available to calculate and store information about the entire temperature difference through a thin structure. In contrast, better results might have been achieved in that case if the finite element method had been used since a polynomial can then represent the temperature difference across the cell [38].

Since the problematic elements in the mesh were not discovered until the validation simulations, they were present during the mesh analysis. They were however not discovered since the residuals and all monitored temperatures became stable during the simulations and no unwanted behaviour was identified. Based on this, and that conduction is a linear phenomenon as previously mentioned, the results from the mesh analysis should still be valid. This is also backed by the good coherence between the simulated and experimental results.

5.1.2 Sources of Error - Experiments

Sources of error are present in all experiments and they contribute to the differences between the simulated and experimental data. There were inaccuracies in the temperature measurements by the thermocouples in the experimental setup, although the error was shown to be small since the thermocouples did not differ more than 0.2 $^{\circ}C$ degrees in room temperature. Another source of error was that since the environment for the test section could not be completely controlled, the temperatures oscillated slightly throughout the experiment. This meant that even though it was run until the temperatures had plateaued, their complete steadiness could not be ensured. This in combination with other sources of errors can be one explanation for the differences between the simulated and experimental results. In addition to this, the measurements of the corners of the resistors that were used for the BCs were taken using only one thermocouple. This meant that all those temperatures were measured at different points in time and might therefore introduce some uncertainties because of this oscillatory behaviour. This error should however be small since the average oscillations were found to be 3 %, *section 3.1.2.1.* The measuring hardware limited the number of thermocouples to 20 and it was therefore prioritised to have more measuring points distributed over the test section than to measure all corners at the exact same time.

5.1.3 Sources of Error - Simulations

One major difference between the simulated and experimental tests was that the BCs of the simulations could not be made to exactly replicate the heat from the resistors in the experiments. As a result of this it was apparent in the validated results that the temperatures measured on the bottom side of the thin plates, directly below the resistors, were slightly higher in the simulations than in the experiments. A reason for this was that the approximated temperature in the middle of the contact between the resistor and the skin plates was used for a large portion of the resistor's contact surface, as described in *section 3.1.1.* As a compensation the remaining part of the BC was most likely colder than in the experiments. The reason for this was that the coldest part of the contact surface, the corners, were used together with the temperature at the centre of the contact surface between the resistor and the skin plates. This gave four cold temperatures and one hot where an average was taken, this would lead to a colder temperature than in the experiments. Based on this, the entire BC should be relatively close to the experimental temperatures although it might not have the same distribution at all locations of the BC. It is therefore reasonable that the temperatures below the resistors were slightly overpredicted in the simulations since they were measured in the centre where the higher temperatures had been applied.

Due to the curvatures of the test section and that placements of resistors and thermocouples were measured by hand, the placements might have deviated between the simulated and experimental tests. However the measurements were performed as thoroughly as possible and the temperature gradients were not extreme which means that the effect on the results should not be too significant. Another difference between the simulated and experimental tests was that the geometries were not completely similar. Alterations were however made on the simulated geometry which ensured that the most significant differences were in regions far from the measured area. These types of errors were difficult to avoid since the physical test section was cut by hand.

The exact materials in the physical test section were not completely known in this thesis. Some parts in the given CAD geometry had materials assigned to them but not all. For some of the parts, an identical or almost identical part was placed somewhere else in the geometry and had an assigned material. In those cases, the material of that part was used and little or no error would be introduced. For the remaining parts, materials of parts with a similar function or size were chosen. Supervisors at SAAB AB assisted in this selection since they had previous knowledge of the parts and materials which would have reduced the introduced error. The test section consisted of the three main types of material titanium, steel and aluminium alloys which had thermal conductivities spanning from around 5-10 W/mK, 15-20 W/mK and 90-130 W/mK respectively, as mention in *section 3.2.1*. The difference in thermal conductivities were significant with especially the aluminium alloys having deviating values compared to steel and titanium. However, almost all materials in the model were some type of aluminium alloy, only a few parts were steel or titanium. Based on this, the error of wrong materials possibly being chosen for some parts should not have a too great impact on the results.

Since constant values for the thermal conductivities of the materials were used, any changes caused by temperature variations were neglected. This would however most likely not have affected the results too much since the test section was heated to a relatively low temperature. The effect would have increased with larger ranges of temperature in the domain and it would therefore be recommended to use polynomial values for the thermal conductivity for those types of simulations.

The contacts created in the solid simulation contributed to either small geometrical changes in the case of the contact interfaces, or a larger or smaller contact surface in the case of the mapped contact interfaces. The geometrical changes occur since a conformal mesh is created, this change should however have almost no effect on the results since only very small areas were affected. The larger or smaller contact surfaces occur since the elements in the mesh did not match the shape of the other contacting surface. It generally produced larger contact surfaces than what would be the case in the experimental test section. This should however not have a significant effect since the materials used are very conductive. This means that if heat is transferred to a larger surface on a cold part instead of being transferred to a smaller region and then conducted to the remaining regions, the difference in temperature distribution should not be very large.

All the investigated points were placed close to the heat source, the reasons for this was that a limited number of thermocouples could be measured simultaneously and that the temperature differences would be so small farther from the heat source that they would not yield relevant results.

5.1.4 Validation

Both the simplified calculations and the simulation test showed that the neglect of radiation did not affect the results substantially, which was also coherent with [25]. The calculations did however show that it contributed to 10 % of the total heat transfer but those calculations approximated the geometry as a thin plate which would reduce the conduction compared to the physical experiment. They also assumed a combined emissivity constant of 0.8 which would mean that both the surfaces of the test section and the surrounding white walls would have an emissivity constant of 0.89. This is a very high value

for the bright colours of the surfaces. The calculations were thereby conservative, which was also backed by the fact that the radiation simulations produced results that on average only differed 4.6 % compared to simulations without radiation. A part of this difference might be that the radiation simulation function *Surface to surface* radiation also contains simplifications but the major part is most likely contributed to the conservativeness of the simplified calculations. Based on the small decrease in accuracy and the large increase in computational cost, *section 4.1.1*, the assumption to neglect radiation is reasonable in these types of simulations.

As mentioned, the *Surface to surface* radiation contains simplifications, for example the setup used in this thesis uses wavelength-independent radiation properties [39]. Since it is a radiation model based on surfaces, the emitting, absorbing and scattering of the thermal radiation by the intermediate medium is not included in the calculations [39]. Despite the simplified formulation of radiation, an indication of how much radiation contributes to the total heat transfer can still be obtained. Since the difference between the temperature distribution with and without radiation was relatively small, the assumption to neglect radiation was most likely valid.

The simulation where radiation was included showed that the temperatures on average decreased with 4.6 % for the measured points. This is reasonable since all the points were measured in regions close to the resistors where high temperatures were present. Because of the high temperatures, more heat will be radiated away from the structure than into it which lowers the temperature.

The comparison between the TCR values obtained in this thesis and those in [22] showed significant differences. A possible explanation for the differences might be the errors presented in this report in combination with that only one stationary test was performed and used as validation. Another explanation for this might be the differences in geometry since the study used simplified thick square blocks while this thesis investigated a complex structural aircraft geometry. The geometry in this thesis might for example have small gaps or sealants between the different parts which would affect the TCR value. This might mean that the TCR value in this thesis could be more applicable for a real life aircraft case. The results in this thesis consistently predicted higher values of TCR than those in the mentioned study, which is reasonable if some of the differences were caused by interfering materials or gaps between the different parts.

The transient simulations provided an additional validation of the solid model and the values of TCR and HTC. Both transient simulations showed a good agreement with the experimental data which indicates that errors in the model were sufficiently small. Although a maximum temperature difference of 9 % was shown for TCR $= 5 \cdot 10^{-4}$ m^2K/W the remaining points all had differences around or below 5 %. One possible explanation for the better coincidence with experimental data for a TCR value of $1 \cdot 10^{-4}$ m^2K/W was that, as previously mentioned, the contact surfaces between different parts were often slightly larger than the actual contact area of the parts. This could have meant that the increased conduction due to the larger contact surfaces was cancelled out when a larger TCR value was used, such as $1 \cdot 10^{-4}$ m^2K/W.

An interesting result was that two points placed on the same part but with different distances to the resistor showed similar behaviour when comparing the simulated and experimental data, point 7 and 20. This indicated that material heat transfer data was

relatively correct, at least for the specified part. The reason for this was that if wrong material data had been used, the difference between simulated and experimental data would either increase or decrease with increasing distance from the resistor.

The stationary results showed that $5 \cdot 10^{-4}$ m^2K/W was closer to the experimental data than $1 \cdot 10^{-4}$ m^2K/W while the transient results showed the opposite. A possible explanation for this was that the temperature varied slightly throughout the stationary validation experiment since the ambient temperature could not be controlled. This meant that it was not possible to make sure that the temperatures throughout the test section were stagnated. In the transient simulations however, the BC was based on the temperature of the resistor throughout the entire experiment. This removes the dependency on stagnated temperatures and could be the reason for the smaller deviations from experimental values for the transient simulations compared to the stationary. This would indicate that the TCR should be chosen based on the transient simulations, which also gives a TCR closer to the results in [22].

5.2 Fluid Model

5.2.1 Verification

A greater refinement with the same amount of elements could have been found if a faster growth rate would have been used where the elements changed in size. Another way to construct the mesh was to base the refinement on the areas of interest and not on the base size. The non constant base size could then have been approximated to a larger extent and smaller elements could have been used in the area of interest. However, to keep a consequent increase in number of elements and a decrease in element size, it was in this thesis chosen to base the refinements on the base size. As found in the mesh analysis a mesh of 98 million elements was found accurate enough and a maximum deviation of 8.48 % was thereby accepted. The reason for the high change in percentage was the monitors' positions. A few of the monitors were positioned at the transition area between two velocities of different magnitudes where minimal mesh refinements could create large changes in the velocities. This could indicate that some of the largest mesh induced errors were captured. The high percentual change of the velocity between the meshes was deemed acceptable in order to reduce the computational cost since the differences in temperature, which was one of the main variables of interest, was sufficiently low.

As mentioned in the method, the y^+ value was kept above 1 in the mesh analysis because of the problematic areas of the given model caused by a previous wrapping. It resulted in that some parts of the geometry had dents in the surface of the aircraft where a smooth surface was expected. These parts were shown to create bad cells which resulted in unphysical flow behaviour. Reaching a converged solution with a $y^+ < 1$ would need a significant reduction in cell size and was therefore not investigated because of the limited time frame and the increased computational cost the simulation would result in. Since $y^+ < 2$ was close to general recommendations for CFD simulations [40], and within the recommendations of STAR-CCM+ [34], it was assumed accurate enough for this thesis since the the *All* y^+ *wall treatment* was used.

5.2.2 Local Domain Size

The investigation concerning the box size for the local domain could be approached in two different ways, as a validation or as a verification. In the method the results from the global model were presented as a form of validation while the choice to use Box 2 in further simulations was based on verification reasoning, *section 3.3.2.1.* The choice of using Box 2 in further simulations was decided independent of similarity to the global model. Reduced deviations to the global model might have been found if larger domains had been investigated as well but since no improvements were found for the largest box, no larger boxes were investigated. Based on general recommendations the chosen box size should be larger [41][42]. Box 2 was however assumed accurate enough for this thesis and the specific domain considered. It was also important to compare the results to the global model to ensure that the flow behaviour was somewhat similar. The reason for this was that the BC used at the inlet and outlet were taken from the global model, and a behaviour with larger deviations to the global model would introduce larger uncertainties. The results showed that the largest deviations were in the free stream area, Figure 18, which was reasonable because of the effect of the local domain and its boundary placements.

Neither of the boxes coincided well with the global model in the free stream but all boxes followed similar trends. The results showed expected behaviour for the smallest box, Box 1. It showed large deviations to the global model in the flow with some distance from the aircraft. This was expected since the sides and top of the domain were placed close to the surface and therefor enabling the fluid flow to be affected by the domain boundaries. It was unexpected that Box 2 and 3 showed little deviations from each other since both boxes had smaller distances to the boundaries than recommended. One reason for Box 3 to not have an increased accuracy could depend on the larger elements being introduced from the global mesh, which were placed at the domain boundaries, Figure 16. This meant that a smaller number of elements were introduced from Box 2 to 3 than between Box 1 and 2. In order to gain a more representative comparison, the size of the boxes could have been investigated in relation to the element sizes as well and not only by an increase in 1.5 m.

Even though the measurements for both Box 2 and 3 were too small in comparison to the general recommendations, improvements might not have been found in further investigations. That the difference between the boxes turns to zero indicated that it was not the side and top boundaries that affect the flow and accuracy, but the inlet, outlet and bottom boundaries that did.

Since the outlet was positioned in the wake of the fluid flow it was reasonable to perform a surface extrusion. Investigating the BC on the sides, top and bottom resulted in interesting findings. When using free stream BCs the fluid flow was shown to be greatly dependent on the parameters used as far field constants, which could be expected since the aircraft surface and the bottom side of the domain were connected. The free stream BC is also advised to not use where rotational flow is present [43], which in unsteady simulations could appear at the bottom for the used domain. The slip walls showed impact on the bottom side close to the boundaries which was an effect from the retarded flow about the aircraft propagated out along the walls. This indicated that the flow around the aircraft surface governed the remaining flow while a free stream BC instead had a larger impact on the flow at the aircraft surface.

That the solution quickly diverged when using the pressure outlet BC on the sides was shown to be the result of the interpolated data that had captured a more complex flow than the considered domain would model. The flow from the global model contained larger turbulent scales which created problematic behaviour and the BC's ability of handling the occurring backflow was affected [44]. At this point it could also be questioned why an outlet BC was not used at the outlet boundary instead of the pressure outlet since the outlet conditions of an outlet BC are determined of the flow upstream and not specified by the user. However, because of the outlet BC's inability to handle recirculation [45], it was early discarded because of the limited size of the local domain and the pressure outlet was therefore chosen to be used for the extruded domain as well.

The slant in the geometry that was a result from the geometric extrusion was expected to affect the flow. The impact was however hard to avoid since other alternatives of extending the domain would result in similar problems. For example if the geometry was extruded in its own direction while at the same time extending the tilted fluid domain, the slant would occur where the geometry would end and a no-slip wall would transition into a slip wall. It would also occur early in the extended model which meant that a larger effect on the flow upstream might have been present. The differences between the local and extruded models towards the global model decreased closer to the slant, Figure 21-23, if the angle change would have had a large effect, the lines closest to the slant would most likely have larger differences and not the other way around. Based on this, the impact of the slant did not result in any large inaccuracies upstream and no further investigations were therefore performed.

5.2.3 Parametric Investigations

Some deviations were expected when keeping the y^+ value within the buffer layer in the investigation of the All y^+ wall treatment since that is not a recommended practice. As the results showed however, no large differences were found dependent on the position of y^+. The reason for not getting any obvious deviations could be because of the smooth geometry of an aircraft where mostly small and expected separations occur due to the laminar and attached flow that are often desired in the aircraft industry in order to reduce the drag [46]. As mentioned in the results, small deviations for the model with y^+ within the viscous sub-layer were present, Figure 30 and 31. The deviation can partly be explained by the size difference in the element sizes within the boundary layer. The element height at the outer layer of the BL was at largest in the mesh where y^+ was within the viscous sub-layer, and smallest when y^+ was in the log-law sub-layer. The small difference between the temperature and velocity magnitude within the BL between the meshes could be because no wall functions were used when in the viscous sub-layer, while the simulated data for the buffer and log-law layer have been adapted through the same modelling techniques. Because of the small deviations found in the results, they indicate that industries similar to SAAB AB does not need to perform y^+ investigations when using All y^+ wall treatment.

In the CFL investigations it was expected that a simulation with a CFL of 100 would resolve less of the turbulence than CFL 1. In Figure 35-37 however, few deviations were found. It indicated that the impact of CFL was small. When instead investigating the instantaneous temperature at a plane it was obvious that the differences between the CFL numbers were large, Figure 39, which was a reasonable results because of the definition of the CFL number. The results showed that a larger CFL number underpredicted the maximum values while overpredicting the minimum values. This was coherent with the

results of the instantaneous plots which showed fewer turbulent structures being captured for the higher CFL numbers. The reason for this was that the increased time step results in that the fluctuations between the samples cannot be captured. This is a part of the error that is introduced when using larger CFL numbers.

The results indicated that a CFL number of 10 could be used in order to save to computational cost while not decreasing the accuracy to a large extent for this specific domain. Similar results were found in [12] where a CFL number of 20 resulted in similar accuracy as a CFL number of 1. It is however important to be aware of that different geometries and domains were used in this thesis and in [12] and no general conclusion could be drawn from the two results in combination. It could however be discussed whether the CFL number was too conservatively calculated in this thesis, as mentioned in *section 3.3.4*. The reason for this was that the CFL number was specified at the jettisoned air but due to the high velocities and small elements in that region, the remaining part of the domain had significantly lower CFL numbers. This meant that a large portion of the flow was modelled with a lower CFL number which would give a more accurately predicted flow. In conclusion however, the two results in combination, this thesis and [12], supports that the CFL number could be larger than unity for small and limited number of areas [20] without the risk of decreasing the accuracy, which was also shown in *section 4.2.3*.

5.2.4 Numerical Techniques and Turbulence Models

That the RANS results both underpredicted and overpredicted the variables in comparison to URANS dependent on location in the domain and flow case was similar to results found in [47] and [48]. The RANS simulations showed to overall predict lower velocities than URANS, which in turn resulted in a prediction of higher temperatures. This was reasonable since a decreased velocity will reduce the rate at which the hot air is transported away. It was seen that these lower velocities were caused by a deceleration of the flow over the sudden geometrical changes close to the inlet, the flat part of the aircraft skin, which then propagated through the entire domain. It was unclear whether the RANS or URANS simulations produced the results closest to a real flow case. It is clear that a lot of trade-offs are made when using RANS and it is therefore recommended for SAAB AB to run a LES simulation to quantify a more correct number of the errors introduced. An LES simulation, or a numerical technique with similar accuracy, is recommended because of its similarities to physical values [49] as well as being cheaper than doing physical experiments at these scales.

That the turbulence was damped when using RKE Two-layer could be explained by the turbulence model's limitation of an overpredicted eddy viscosity [14]. This because an increase in eddy viscosity dampens the turbulence. The near wall damping functions existing in the RKE model could also be responsible for the damped turbulence [50]. Similar results were found in [51] where the length of the wake was shorter for RKE than SST $k-\omega$ and the turbulence flattened out earlier. It was however hard to determine if the SST $k-\omega$ or the RKE Two-layer gave most accurate results because of the lack of validation material. The SST $k-\omega$ model is however known for its good applicability in flows where large adverse pressure gradients are present which is found in the aeronautical industry. It might therefore be assumed more accurate than the RKE Two-layer model. To reach a good comparison between the turbulence models it is recommended for SAAB AB to compare the two towards an LES simulation, or a numerical technique with similar accuracy, for the same reasons as previously mentioned as well as its independency of turbulence model.

It was found that the URANS simulations using the RKE Two-layer model showed no unsteady fluctuations. The reason for this was, as previously mentioned, that the model damped the turbulence and since the flow case used did not contain fluctuations of very high magnitude, the RKE Two-layer model was unable to capture it. Since fighter aircraft bodies are designed to avoid the creation of large separations or vortex sheddings, the RKE Two-layer model might in many cases be unsuitable for these types of flows because of its inability to capture the smaller fluctuations. However, a comparison with more accurate simulations or experimental data would be necessary in order to draw any certain conclusions.

6 Conclusion

Due to the small differences between a solid simulation with and without radiation in combination with the significant increase in computational time, it is reasonable to neglect radiation in these types of simulations. It was also seen that if radiation is included and the *Surface to surface radiation* is used, a low patch to face proportion of 5-10 % produce accurate results at a low cost. It was also seen that the optimal TCR value differed between the stationary and transient simulations, with an optimal value of $5 \cdot 10^{-4}$ m^2K/W for the stationary and $1 \cdot 10^{-4}$ m^2K/W for the transient. The average difference between experimental and simulated data for the stationary simulation with a TCR of $5 \cdot 10^{-4}$ m^2K/W and HTC of 8.34 W/m^2K showed an average difference of 6.6 % while the transient simulations on average differed 3.4 and 4.6 % for TCR $1 \cdot 10^{-4}$ and $5 \cdot 10^{-4}$ m^2K/W respectively. The HTC value was in both transient cases 8.34 W/m^2K. Based on the low differences between the simulated and experimental data, results from the solid model can be trusted to a large degree although errors always will be present.

The local domain considered in fluid flow simulations in this thesis had multiple types of errors introduced because of the domain size, which had the inlet and outlet boundary in connection to the aircraft surface. However, the results of investigations of the CFL number, turbulence model and numerical technique can still be relevant when compared to each other and since similar trends could be found in the literature. It was found and supported that a $CFL > 1$ could be used if present in small and limited number of areas. Since there was no obvious validation for the numerical techniques and turbulence models, it is recommended for SAAB AB to perform simulations of a more accurate numerical technique in order to quantify to what degree the errors introduced are when simulating with currently used methods. The results obtained when using the *All* y^+ *wall treatment* for different values of y^+ indicate that industries similar to SAAB AB does not need to perform y^+ investigations when using the function, since little or almost no differences were found between the different cases. Because of the errors and uncertainties introduced for the local domain, it is recommended to perform future investigations in a domain where the whole aircraft is taken into account.

7 Future Work

The solid simulation model resulted in close coherence with the experimental data and the TCR value of $1 \cdot 10^{-4}$ could therefore be used in future CHT simulation models. It could be of interest to investigate to what degree the globally used TCR value of $1 \cdot 10^{-4}$ fit to experimental data performed on a full size aircraft. The reason for this was that the TCR in an aircraft varies and only a small part of the aircraft was considered in this thesis.

Future investigations for the fluid simulation parameters should be performed where the full model of a fighter aircraft is considered. In order to quantify the errors introduced when performing RANS simulations a simulation with a heavier and more correct numerical technique should be performed, for example an LES simulation. Experimental tests could also be used, however, the cost of flight tests are large. In comparison, an LES simulation is most likely cheaper as well as faster and is therefore recommended. The same stands for when investigating the use of different turbulence models. It would be interesting to see if either of the turbulence models give more accurate predictions in different areas. Other turbulence models than SST $k - \omega$ and RKE Two-layer could also be of interest to investigate. Simulations should also be performed where the impact of the CFL number is investigated where support for $CFL > 1$ in limited areas can be found in this thesis as well as in [12], however, the cases differ in geometry and flow case which is important to be aware of.

References

[1] W. Harrison III, K. Binns, S. Anderson, and R. Morris, "High heat sink fuels for improved aircraft thermal management," *SAE Transactions*, pp. 709–718, 1993.

[2] K. Hanjalic, "Will rans survive les? a view of perspectives," 2005.

[3] A. B. Haines, "Know your flow - the key to better prediction and successful innovation," p. 1, 2012.

[4] J. P. Holman, *Heat Transfer*. McGraw-Hill, 2010.

[5] K. Storck, M. Karlsson, I. Andersson, J. Renner, and D. Loyd, *Formelsamling i termo- och fluiddynamik*. Tekniska högskolan vid Linköpings universitet, 2016.

[6] H. K. Versteeg and W. Malalasekera, *An introduction to computational fluid dynamics: the finite volume method, Chapter 3*. Pearson Educated Limited, 2007.

[7] A. F. Molland and S. R. Turnock, *Marine rudders and control surfaces: principles, data, design and applications*. Elsevier, 2011.

[8] J. D. Anderson Jr, *Fundamentals of aerodynamics*, 6th ed. Tata McGraw-Hill Education, 2017.

[9] S. D. I. Software., *Simcenter STAR-CCM+ Documentation, Fundamental Equations*, Siemens, 2020.

[10] H. K. Versteeg and W. Malalasekera, *An introduction to computational fluid dynamics: the finite volume method, Chapter 2*. Pearson Educated Limited, 2007.

[11] S. D. I. Software., *Simcenter STAR-CCM+ Documentation, RANS Turbulence Models*, Siemens, 2020.

[12] P. Ekman, "Important factors for accurate scale-resolving simulations of automotive aerodynamics," vol. 2068, pp. 19,23–24, 32, 61–62, 2020.

[13] L. Davidson, "Fluid mechanics, turbulent flow and turbulence modeling," 2015.

[14] T.-H. Shih, W. W. Liou, A. Shabbir, Z. Yang, and J. Zhu, "A new $k-\epsilon$ eddy viscosity model for high reynolds number turbulent flows," *Computers & fluids*, vol. 24, no. 3, pp. 227–238, 1995.

[15] S. D. I. Software., *Simcenter STAR-CCM+ Documentation, Deciding on $k-\varepsilon$ model*, Siemens, 2020.

[16] F. R. Menter, "Two-equation eddy-viscosity turbulence models for engineering applications," *AIAA journal*, vol. 32, no. 8, pp. 1598–1605, 1994.

[17] W. Chan, P. Jacobs, and D. Mee, "Suitability of the k–ω turbulence model for scramjet flowfield simulations," *International Journal for Numerical Methods in Fluids*, vol. 70, no. 4, pp. 493–514, 2012.

[18] S. D. I. Software., *Simcenter STAR-CCM+ Documentation, RANS Turbulence Models*, Siemens, 2020.

[19] G. Caminha, "The cfl condition and how to choose your timestep size," https://www.simscale.com/blog/2017/08/cfl-condition/#:~:text=The%20Courant%E2%80%93Friedrichs%E2%80%93Lewy%20or,that%20derives%20the%20CFL%20condition., 2019.

[20] Ansys-Inc., *Ansys Fluent User Guide, 13.2.4.1 Time Discretization*, Ansys, 1 2020.

[21] F. Balduzzi, A. Bianchini, G. Ferrara, and L. Ferrari, "Dimensionless numbers for the assessment of mesh and timestep requirements in cfd simulations of darrieus wind turbines," *Energy*, vol. 97, pp. 246–261, 2016.

[22] V. Andersson, "Thermal contact conductance in aircraft applications," 2018.

[23] T. Arts, J. Anthoine, H. L. Boerrigter, J.-M. Buchlin, M. Carbonaro, G. Degrez, R. Dénos, D. Fletcher, D. Olivari, M. L. Riethmuller, and R. A. Van den Braembussche, *Measurement Techniques in Fluid Dynamics: An Introduction.* Karman Institute for Fluid Dynamics von, 1994.

[24] R. Pincus and K. F. Evans, "Computational cost and accuracy in calculating three-dimensional radiative transfer: Results for new implementations of monte carlo and shdom," *Journal of the Atmospheric Sciences*, vol. 66, no. 10, pp. 3131–3146, 2009.

[25] B. R. Sehgal *et al.*, *Nuclear safety in light water reactors: severe accident phenomenology.* Academic Press, 2011.

[26] S. D. I. Software., *Simcenter STAR-CCM+ Documentation, Weak Contact Creator*, Siemens, 2020.

[27] ——, *Simcenter STAR-CCM+ Documentation, Contact Interface*, Siemens, 2020.

[28] ——, *Simcenter STAR-CCM+ Documentation, Mapped Contact Interface*, Siemens, 2020.

[29] ——, *Simcenter STAR-CCM+ Documentation, Weak Contacts*, Siemens, 2020.

[30] K. N. Babu, "Thermal contact resistance: experiments and simulation," Master's thesis, 2015.

[31] S. D. I. Software., *Simcenter STAR-CCM+ Documentation, S2S (Surface-to-Surface) Radiation*, Siemens, 2020.

[32] ——, *Simcenter STAR-CCM+ Documentation, Surface Radiation Exchange Reference*, Siemens, 2020.

[33] ——, *Simcenter STAR-CCM+ Documentation, Trimmed Mesh*, Siemens, 2020.

[34] ——, *Simcenter STAR-CCM+ Documentation, Setting Up Wall Treatment*, Siemens, 2020.

[35] T. Dekker and V. Krishnan, "Numerical investigations of brake cooling performance," Master's thesis, 2018.

[36] A. Kapoor, "A quick approach to boundary layer meshing - for beginners," 2016.

[37] A. Rivoldini, T. Van Hoolst, O. Verhoeven, A. Mocquet, and V. Dehant, "Geodesy constraints on the interior structure and composition of mars," *Icarus*, vol. 213, no. 2, pp. 451–472, 2011.

[38] M. Asadzadeh, *An Introduction to the Finite Element Method for Differential Equations*. John Wiley & Sons, 2020.

[39] S. D. I. Software., *Simcenter STAR-CCM+ Documentation, Surface Radiation Exchange Reference*, Siemens, 2020.

[40] M. K. F.R. Menter and R. Langtry, "Ten years of industrial experience with the sst turbulence model," *Turbulence, Heat and Mass Transfer*, vol. 4, 2003.

[41] S. Hardie, "Drag estimations on experimental aircraft using cfd," 2006.

[42] K. Lammers, "Aerodynamic cfd analysis on experimental airplane," 2015.

[43] S. D. I. Software., *Simcenter STAR-CCM+ Documentation, Free-Stream*, Siemens, 2020.

[44] ——, *Simcenter STAR-CCM+ Documentation, Pressure Outlet*, Siemens, 2020.

[45] ——, *Simcenter STAR-CCM+ Documentation, Outlet*, Siemens, 2020.

[46] R. Longobardi, "Fluid dynamic instabilities in complex flow systems," Ph.D. dissertation, Université Paul Sabatier-Toulouse III; Università degli studi (Salerne, Italie), 2019.

[47] Z. Yang, "Assessment of unsteady-rans approach against steady-rans approach for predicting twin impinging jets in a cross-flow," *Cogent Engineering*, vol. 1, no. 1, p. 936995, 2014.

[48] M. Carnevale, S. Salvadori, F. Martelli, and M. Manna, "A comparative study of rans, urans and nles approaches for flow prediction in pin fin array," in *10 th European Conference on Turbomachinery Fluid dynamics & Thermodynamics*. EUROPEAN TURBOMACHINERY SOCIETY, 2013.

[49] ——, "A comparative study of rans, urans and nles approaches for flow prediction in pin fin array," in *10 th European Conference on Turbomachinery Fluid dynamics & Thermodynamics*. EUROPEAN TURBOMACHINERY SOCIETY, 2013.

[50] S. Geller, K. Holeczek, A. Winkler, T. Tyczynski, T. Weber, M. Gude, and N. Modler, "Multiscale characterization and testing of function-integrative fiber-reinforced composites," in *Performance Testing of Textiles*. Elsevier, 2016, pp. 155–176.

[51] A. Rezaeiha, H. Montazeri, and B. Blocken, "On the accuracy of turbulence models for cfd simulations of vertical axis wind turbines," *Energy*, vol. 180, pp. 838–857, 2019.

Appendix

A Resistor RND Components

The product sheet for the resistors used as heating components in this thesis is presented below.

Wirewound Resistors in Aluminium Housing

RND components

Features

- Aluminium housing for direct heat sink attachment
- Excellent heat transfer and small dimensions
- Good electrical stability, reliability and mechanical rigidity
- Values from R10 to 27K
- RoHS compliant
- Custom terminations, mounting arrangements possible

General Series Characteristics

Characteristic	Condition	Compliance
Tolerance (Tighter tolerance available on request)	For values less than 1 Ω For values greater than 1 Ω	± 5% ± 0.25 to ± 5%
Temperature co-efficient (Lower TCR available on request)	For values less than 100 Ω For values greater than 100 Ω	60 ppm / °C 30 ppm / °C
Insulation resistance	Dry / Normal	10GΩ min
Change in resistance - short time overload - shelf life	 10x rated voltage for 5 sec After 3 years	 ± 0.5% < ± 1%
Incombustibility	16x rated wattage for 5 sec	No flame
Operating temperature	From - 25°C to 250 °C	

Global Part Number Information

Example: RND 15525 1K2 F

RND 15525	1K2	F
RND 15525 = 25 W RND 15550 = 50 W RND 155100 = 100 W RND 155200 = 200 W RND 155300 = 300 W	Resistance	Tolerance: F=1% J=5%

Electrical Specifications

Series	Power rating on standard heat sink @ 25 °C	Power rating with no heat sink @ 25°C	Resistance range	Limiting element voltage (DC / AC rms)	Dielectric strength (AC peak)	Weight approx. (g)	Standard heat sink	
							Area (cm²)	Thickness (mm)
RND 15525	25	12.5	R10 - 27K	550	2500	15	550	1
RND 15550	50	20	R10 - 10K	1250	2500	30	550	1
RND 155100	100	50	R10 - 10K	1900	5000	115	1000	3
RND 155200	200	50	R10 - 1K	1900	5000	475	3750	3
RND 155300	300	75	R10 - 1K	2500	5000	700	5800	3

Power Derating Curve

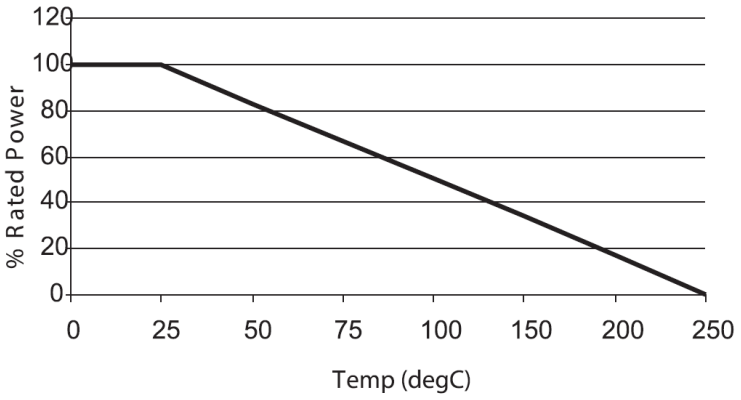

Wirewound Resistors in Aluminium Housing

RND components

Temperature Rise Chart

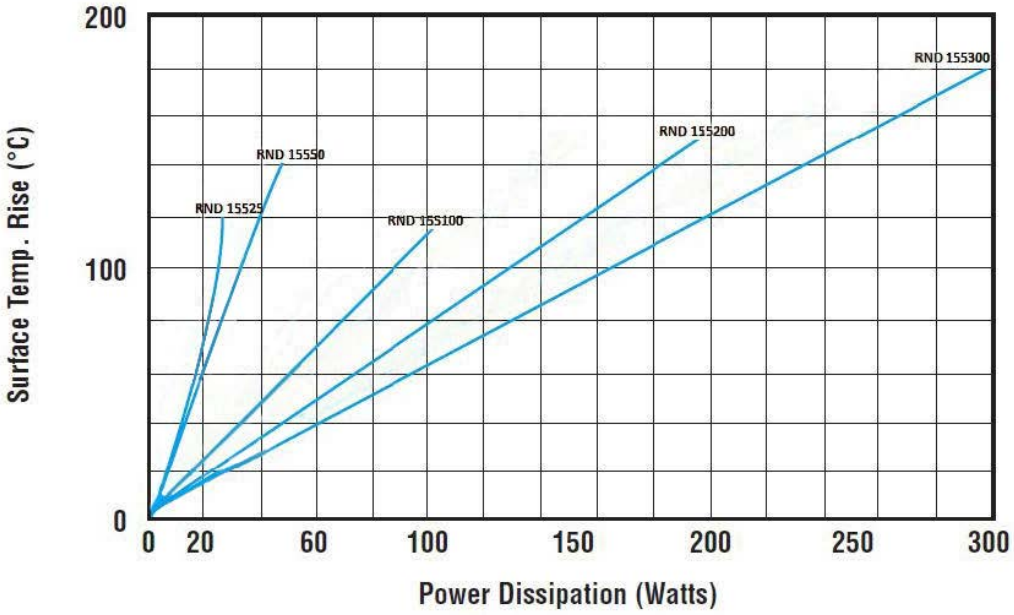

Mechanical Specifications

Series	L ± 0.5	A max.	H	PX ± 0.3	PX1	PY ± 0.3	M ± 0.5	B max.	C max.	D
RND 15525	27.3	51.8	28	18.3	-	19.8	3.2	7.5	15	3
RND 15550	50.1	72.5	30	39.7	-	21.4	3.2	8.5	17	3
RND 155100	65.4	87.5	48	35	-	37.0	4.4	12	26	4
RND 155200	89	143	73	35	-	57.2	5.1	20.5	45	5.5
RND 155300	127	180	73	52	-	59.0	6.6	20.5	45	5.5

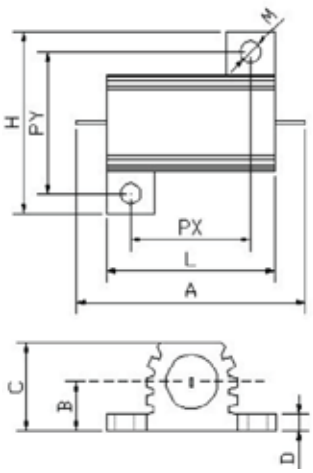

RND 15525
RND 15550

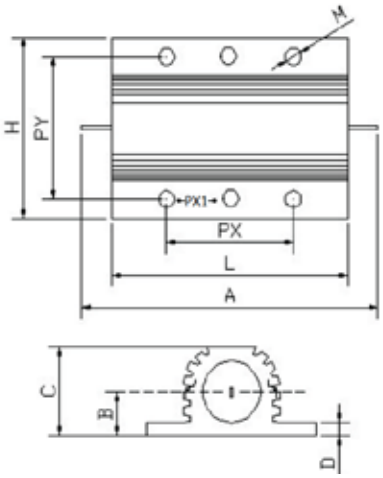

RND 155100

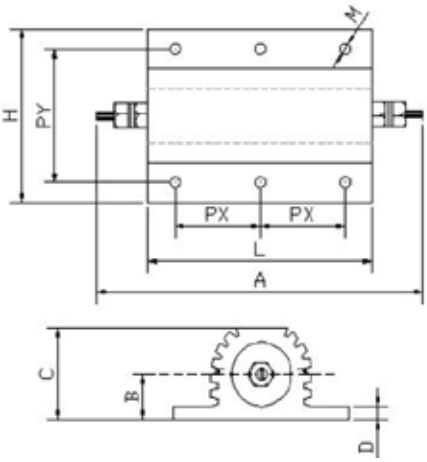

RND 155200
RND 155300

B Solid Transient Simulation Results

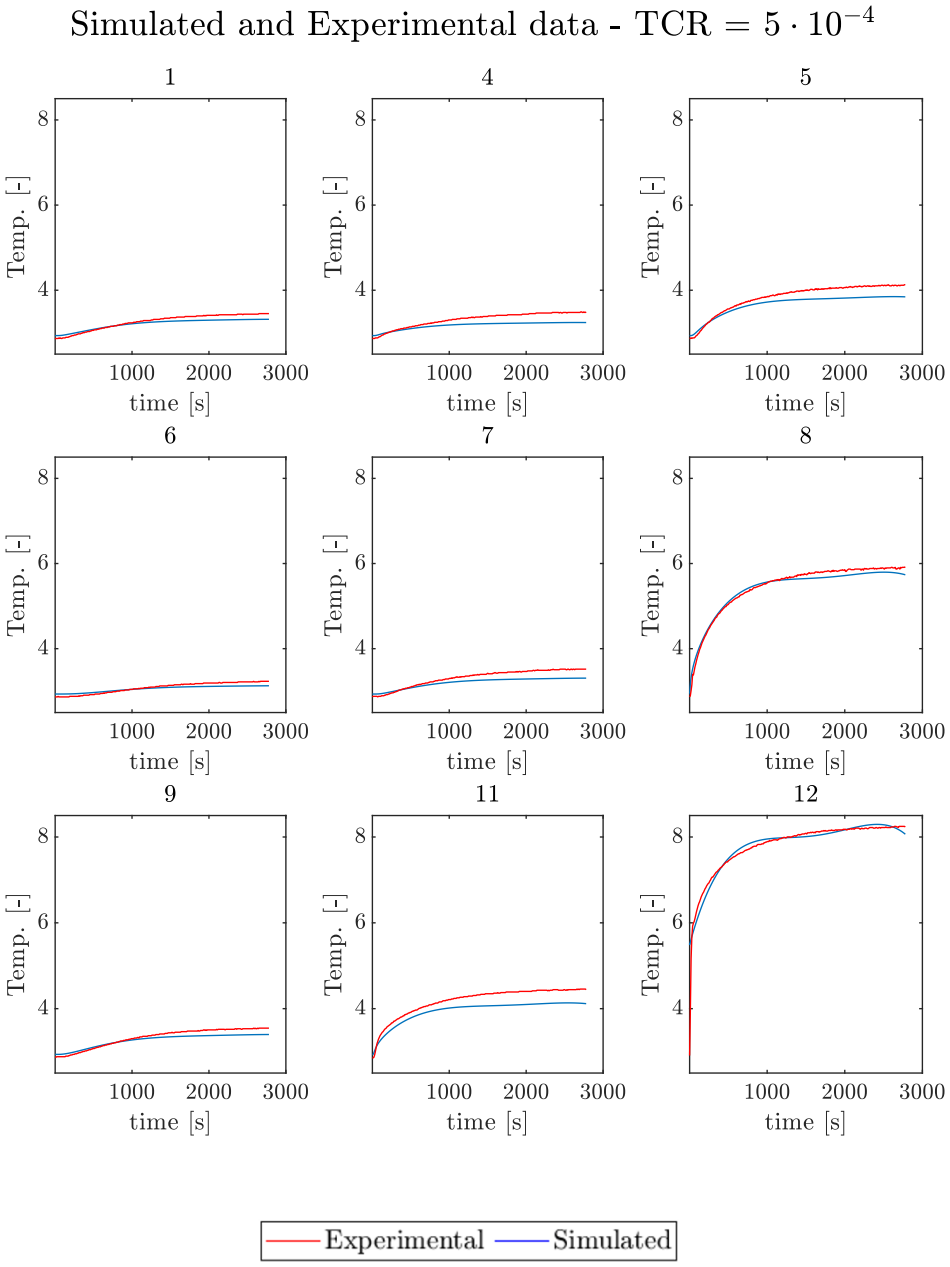

Figure 45: Normalized transient simulated and experimental temperatures for a TCR value of $5 \cdot 10^{-4}$ m^2K/W, points 1-12. Points 2-3 and 10 are excluded since they were used to measure BC temperatures and therefore irrelevant to measure in the simulations.

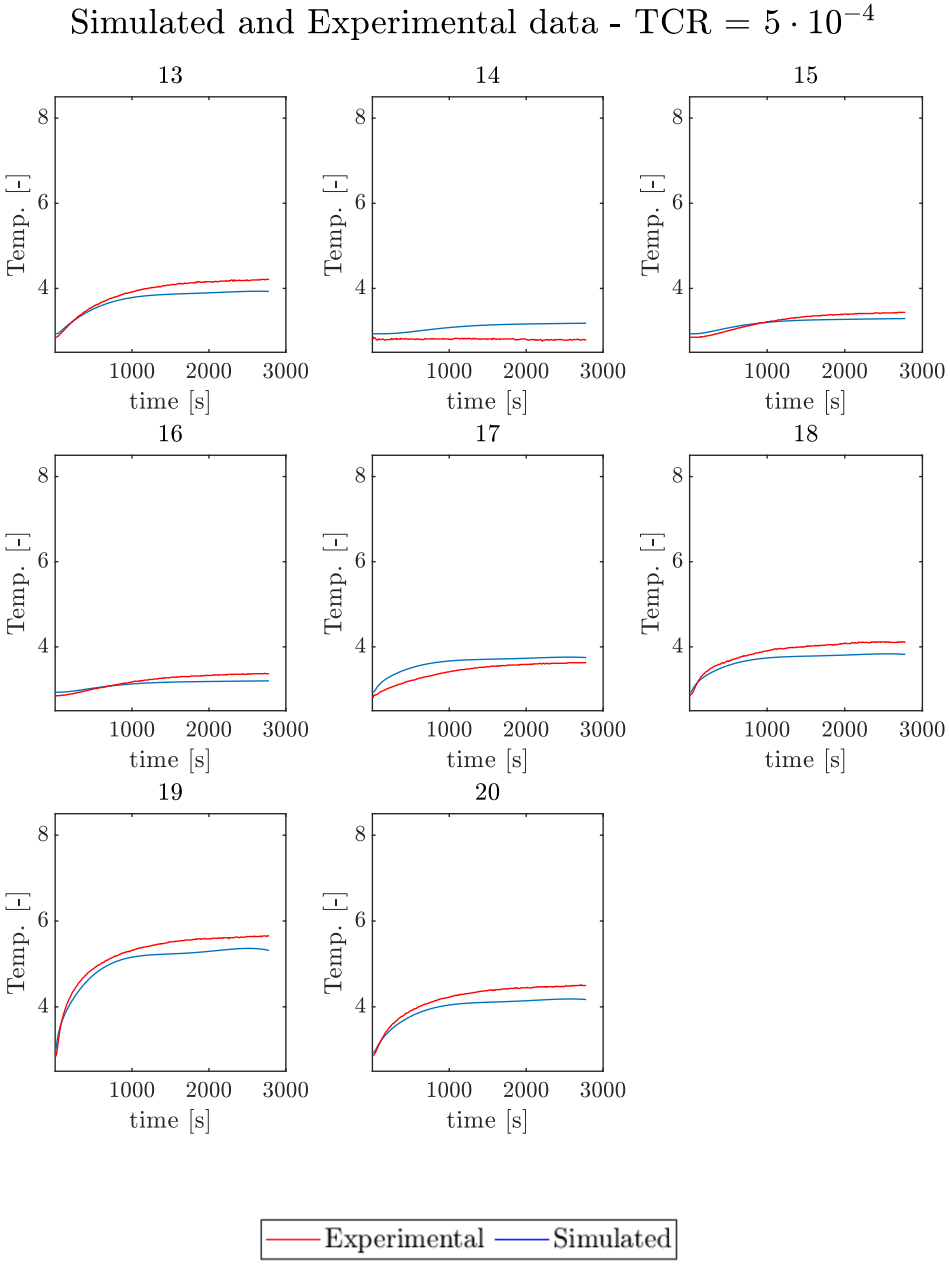

Figure 46: Normalized transient simulated and experimental temperatures for a TCR value of $5 \cdot 10^{-4}$ m^2K/W, points 13-20.

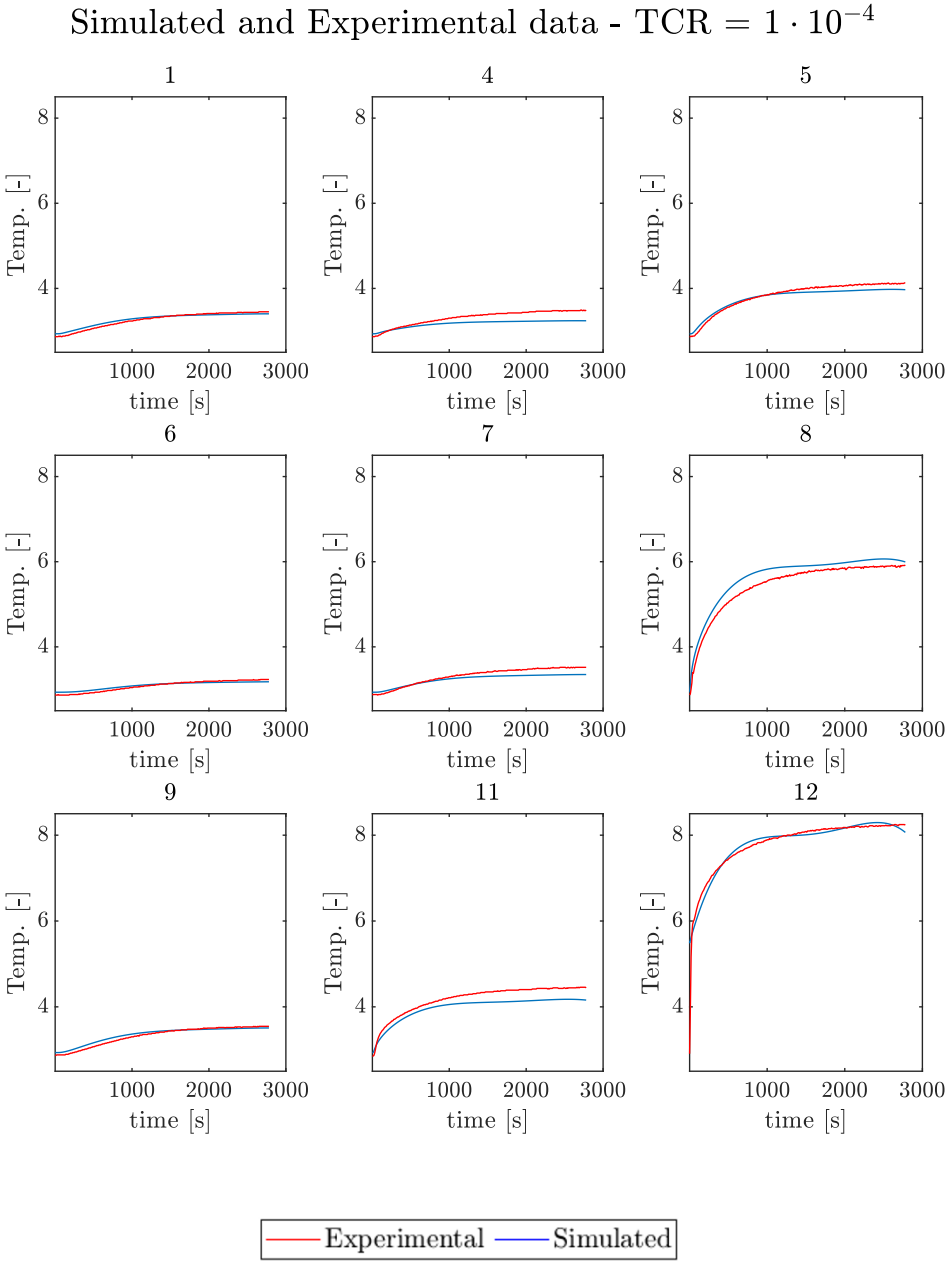

Figure 47: Normalized transient simulated and experimental temperatures for a TCR value of $1 \cdot 10^{-4}$ m^2K/W, points 1-12. Points 2-3 and 10 are excluded since they were used to measure BC temperatures and therefore irrelevant to measure in the simulations.

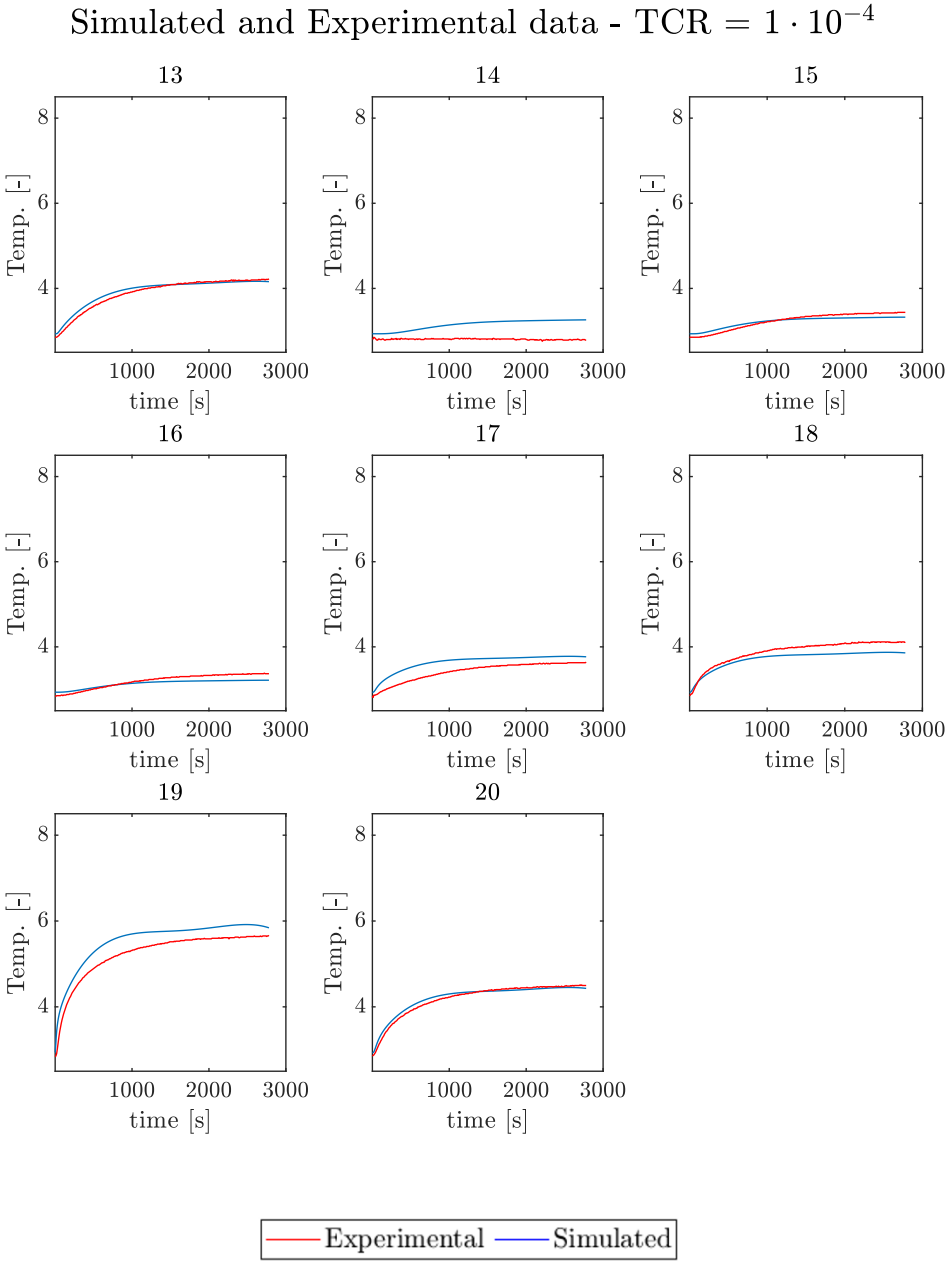

Figure 48: Normalized transient simulated and experimental temperatures for a TCR value of $1 \cdot 10^{-4}$ m^2K/W, points 12-20.